Model development based on discrete particle simulations of partially- and fully-saturated granular media

by

Qiong Zhang

Submitted to the Department of Mechanical Engineering
in partial fulfillment of the requirements for the degree of

Doctor of Philosophy in Mechanical Engineering and Computation

at the

MASSACHUSETTS INSTITUTE OF TECHNOLOGY

February 2023

Author .....
Department of Mechanical Engineering
November 29, 2022

Certified by .....
Ken Kamrin
Professor of Mechanical Engineering
Thesis Supervisor

Accepted by .....
Nicolas G. Hadjiconstantinou
Professor of Mechanical Engineering
Chairman Department Committee on Graduate Theses

Model development based on discrete particle simulations of partially- and fully-saturated granular media

by

Qiong Zhang

Submitted to the Department of Mechanical Engineering
on November 29, 2022, in partial fulfillment of the
requirements for the degree of
Doctor of Philosophy in Mechanical Engineering and Computation

Abstract

Granular materials are ubiquitous in industrial and geophysical scenarios. At a high computational expense, the discrete element method (DEM) simulates granular materials with a high accuracy by tracking individual particles. At the other extreme, empirical formulas based on dimensional analysis and continuum models are convenient to be applied to large scale problems, but calibrations may be needed. In this thesis, DEM simulations are carried out as virtual experiments to study the particle-scale physics and then guide the formulation of empirical relations or continuum models for two applications.

Dynamic similarity, commonly applied in fluid systems, has recently been extended to locomotion problems in granular media. Our previous research was limited to locomotors in cohesionless, flat beds of grains under the assumption of a simple frictional fluid rheology. However, many natural circumstances involve beds that are sloped or composed of cohesive grains. Expanded scaling relations are derived and DEM simulations are performed as validation, with inclined beds and cohesive grains using rotating "wheels" of various shape families, varying size and loading conditions. The data show a good agreement between scaled tests, suggesting the usage of these scalings as a potential design tool for off-road vehicles and extra-planetary rovers, and as an analysis tool for bio-locomotion in soils.

In the bedload sediment transport process, the variability in the relation between sediment flux and driving factors is not well understood. At a given Shields number, the observed dimensionless transport rate can vary over a wide range in controlled systems. A two-way coupled fluid-grain numerical scheme has been validated against physical experiments of spherical sediment particles. It is used to explore the parameter space controlling sediment transport in simple systems. Examination of fluid-grain interactions shows fluid torque is non-negligible near the threshold. And the simulations guide the formulation of continuum models for the bedload transport and the creep flow. Furthermore, a numerical scheme has been developed to simulate the transport of natural shaped sediment particles. Conglomerated spheres, approximating the real shapes from CT scanning, are constructed in DEM and coupled with the

fluid solver. Agreement with the corresponding flume experiments is observed.

Thesis Supervisor: Ken Kamrin
Title: Professor of Mechanical Engineering

Acknowledgments

First and foremost, I owe thanks to my advisor Ken Kamrin. Ken is always willing to discuss detailed problems and his physical intuition helped a lot in this simulation based work. After finishing the master's degree with Ken, my research direction drastically changed from non-local effects of granular materials into sediment transport modeling which I had been longing for before I came to MIT. I am sincerely grateful for Ken's patience and help during this long process in the new field. In the years working with Ken, my curiosity are strongly influenced by his enthusiasm, and my presentation skill also improved a lot.

I would love to express my gratitude to my thesis committee member and collaborator, geologist, Prof. J. Taylor Perron. Without much background in geophysics, I got into this field with the help from Taylor's classes, group meetings and field trips. The encouraging conversations and the insightful comments from Taylor have been very helpful.

I would like to thank my committee member: Prof. Wim van Rees, for the valuable feedback and advises along the way.

Thanks to Prof. Dick Yue who started the wonderful journey by introduced me to Ken in a restroom break. This is one of the most MIT things I have experienced.

I would also love to thank my collaborators: Eric Deal, Santiago J. Benavides, Matthew Rushlow and Prof. Jeremy G. Venditti. Their carefully designed experiments have made excellent benchmark cases and their insights in the research area inspired me a lot. I am especially grateful to Eric for the patience and help, from whom I obtained enormous details about the experiments and the field. I am also thankful to the other group members in Taylor's group: Rose Palermo, Marjorie Cantine, Una Schneck and Morgan Schmidt for introducing the knowledge of geology, especially Maya Stokes and Sam Goldberg for organizing the filed trips and helping with the courses as TA's, .

I am thankful to the past and present members in the Kamrin group: Sachith Dunatunga, Tyler Olsen, James Slonaker, Aaron Baumgarten, Stephen Townsend,

Maytee Chantharayukhonthorn, Shashank Agarwal, Saviz Mowlavi, Seongmin Kim, William Zunker, David L. Henann, Hesam Askari, Ramin Ghelichi, Chen-Hung Wu, Xiaolin Wang and Eduardo Rojas. They have been great colleagues to works with. I am especially grateful to Patrick Mutabaruka for walking me through the titanic DEM-LBM code on top of which I made modifications for the simulations in this work, and for teaching me “c’est la vie" when numerical issues came out.

I am grateful for the assistance from administrative staff in MechE, especially Leslie Regan, Christina Spinelli, Ray Hardin, Saana McDaniel and Una Sheehan. I am also thankful to the campus stuff at the Covid testing stations in the pandemic.

I appreciate my friends in MIT and in the dragon boating community, who made my stay in Boston full of pleasure. I owe thanks to Guowei Zhang who accompanied me as a roommate for 6 years and have provided many advises on improving the data structure as well as parallelization of the DEM-LBM code.

Last but not least, I would like to thank my parents and my wife Xinyue Ma, especially for the support, accompany and encouragements during the pandemic. “The greatest thing you’ll ever learn, is just to love and be loved in return".

Contents

List of Figures

List of Tables

Chapter 1

General introduction

1.1 Background

Granular materials are ubiquitous in daily lief and industrial processes, such as the transport and storage of food grains and pharmaceutical capsules/tablets. In geophysics, the aeolian transport of sand and the sediment transport of gravels on river beds shape the natural landscapes. Extraplanetary scenarios are also seen, for example the Mars rover Spirit has been stuck in sand since 2009. Mathematical description of the behaviour of granular matters are challenging since they can behave like solid, fluid and gas, and they can transit from one phase to another in certain conditions. Sometime multiple phases of the three can co-exist.

A lot of experimental and numerical efforts have been made for better understanding of the granular materials. The discrete element method (DEM) [1] simulates granular materials with a high accuracy by tracking individual particles and going through the pair-wise interactions with a contact law. DEM simulations can provide detailed dynamic variables which are not easy to access in physical experiments. As a consequence, a large number of research have been conducted using DEM (see the review paper [2] for more details) and it has also been couple with computational fluid dynamics (CFD) to study multi-phase granular flows (see these two reviews [3, 4]). One of the problems is that in many applications, the length scale we are interested in in are much larger than the particle size. The DEM approach may be

computationally too expensive or even impossible.

At the other extreme of computational cost, continuum models [5, 6, 7] in which the particle-wise variables are homogenized into continuous fields to be solved, as well as empirical relations [8, 9], are convenient to be applied to large scale problems, but calibrations may be needed. In this thesis, DEM based simulations are carried out as virtual experiments to study the particle-scale physics and then guide the formulation of empirical dimensionless relations or continuum models for two applications: (1) locomotion problems in granular media, and (2) the bedload sediment transport process, leading to 3 parts in this thesis.

In the first part of this thesis, DEM simulations of different shaped wheels on granular beds with modified inter-particle contact laws are used to study dynamic similarities of the locomotion problems in granular media, guided by dimensional analysis. Scaling relations for driving performance, namely the power and traveling velocity, are proposed and validated for wheeled locomotion inclined and cohesive granular beds.

In the second part of the thesis, DEM is coupled with LBM to simulate the bedload sediment transport process of round particles with a sub-particle resolution, for a better understanding of the variability in the relation between sediment flux and driving factors. After being validated against the corresponding flume tests, the DEM-LBM simulations are used to explore the parameter space controlling sediment transport in simple systems. Examination of the accessible variables that are not easy to be measured in experiments are carried out to guide the formulation of continuum models for the sediment transport as well as the creep flow beneath the sediment bed surface.

In the last part of the thesis, based on the shape approximation of natural gravels using clusters of superimposed spheres, a novel DEM-LBM scheme is developed to simulate the transport of natural shaped sediment particles. The results are compared with the corresponding sediment transport of natural gravels.

1.2 Contributions

The dimensional analysis and the wheel simulations (presented in Chapter 2) were developed in collaboration between myself, my advisor Ken Kamrin and Stephen Townsend. The Navier slip boundary condition, the DEM-LBM simulations and the continuum modeling (presented in Chapter 3) are developed jointly between myself and Ken Kamrin. The CT scanning, multi-sphere approximation of the natural gravels and the flume experiments were carried out by Eric Deal, Santiago J. Benavides, Matthew Rushlow, my thesis committee member J. Taylor Perron and Jeremy G. Venditti. With the reconstructed multi-sphere particles, the benchmarks of the particle properties and DEM-LBM simulations (presented in Chapter 4) were finished jointly by me and Ken Kamrin. The DEM-LBM code was adapted from Patrick Mutabaruka's PhD work with major modifications including the implementation of Navier slip boundary condition (Chapter 3) and multi-sphere technique (Chapter 4) as well parallelization and calibration by me.

1.3 Publications

This thesis contains material that was published in the following articles:

1. Qiong Zhang, Stephen Townsend and Ken Kamrin (2020). Expanded scaling relations for locomotion in sloped or cohesive granular beds. *Physical Review Fluids*, 5(11): 114301.

2. Qiong Zhang, Eric Deal, J. Taylor Perron, Jeremy G. Venditti, Santiago J. Benavides, Matthew Rushlow and Ken Kamrin (2022). Fluid-driven transport of round sediment particles: From discrete simulations to continuum modeling. *Journal of Geophysical Research: Earth Surface*, 127(7): e2021JF006504.

Chapter 2

Scaling relations for locomotion in inclined non-cohesive and horizontal cohesive granular media

This chapter includes results previously published by this author in Zhang et al., 2020 [10].

2.1 Background

Scaling relations for locomotion in flat beds of dry granular material have recently been proposed by considering dynamic similarity in a presumed continuum representation [11]. Despite the complexity of granular rheology, including history-dependent effects [12, 13, 14], anisotropy [15], hysteresis [16], rate-dependent effects [17, 18], non-local effects [6, 19] and relaxation [20], the proposed scaling relation in [11] is based on the assumption of a simple rate-independent frictional-plastic rheology. Even though a simple constitutive model is assumed, the obtained scalings are shown to describe the features of locomotion in flat, non-cohesive, dry granular beds in a number of experiments and discrete element method (DEM) simulations. However, terrains in nature are frequently sloped (e.g. hills, piles, dunes) and the grains may be cohesive, typically due to moisture or powder-like attraction, giving rise to novel locomotive

dynamics [21, 22]. How or if scaling relations extend under these circumstances has remained unclear. Furthermore, since the previous scaling law was shown to be effective under variations of gravity, if an extended scaling relation could be found, it could lead to novel protocols for modeling extraplanetary rovers by way of experiments performed on earth that properly scale the gravity and essential frictional/cohesive soil character of the target environment.

In this chapter, extended scaling relations for basic locomotive observables, such as power expenditure of the locomotor and its traveling velocity, are proposed for use in inclined and/or cohesive granular beds. For verification, DEM simulations are performed using locomotors of various sizes and three different locomotor shapes (triangle, rectangle and hexagonal) along with a variety of mass loadings, rotation speeds, and gravities. We show the proposed scalings are satisfied in separate studies of sloped beds and cohesive grains.

2.2 Dimensional analysis

Our scaling analysis begins by supposing a simple continuum model for the granular media and analyzing its dimensional consequences. First, the media satisfies momentum balance

$$\rho \dot{\boldsymbol{v}} = \nabla \cdot \boldsymbol{\sigma} + \rho \boldsymbol{b}$$

where $\boldsymbol{v}$ is the velocity of a material point, $\boldsymbol{\sigma}$ the Cauchy stress tensor, ρ the density of the material, and $\boldsymbol{b}$ the specific body force. We consider a constitutive relation that assumes wherever the density is below a critical value, ρ_0, the material is disconnected and thus stress-free (i.e. $\boldsymbol{\sigma} = \mathbf{0}$ when $\rho < \rho_0$). Alternatively, in the dense state, which is described as when $\rho = \rho_0$, we presume a frictional and cohesive rheology, which

can be concisely summarized with the system of constraints below:

$$\dot{\rho}(C_2 + p) = 0 \quad \text{and } C_2 + p \geq 0 \text{ and } \dot{\rho} \leq 0,$$
$$f_y \cdot \dot{\gamma} = 0 \quad \text{and } f_y = \tau - \mu_s p - C_1 \leq 0 \text{ and } \dot{\gamma} \geq 0,$$

where p is the pressure, $\dot{\gamma}$ the shear rate, τ the shear stress, and μ_s the material critical friction coefficient [1]. C_1 is the cohesive shear stress that must be overcome in order to plastically shear the material at zero pressure [23, 24, 25, 26], and $-C_2$ is the hydrostatic stress necessary to detach the material in uniform expansion. In words, the first equation above states that material exiting the dense state ($\dot{\rho} < 0$) does so when its pressure becomes critical ($p = -C_2$), otherwise material that is below the expansion criterion ($p > -C_2$) can only flow incompressibly ($\dot{\rho} = 0$). The second equation above states that material is either shearing and the stress satisfies $f_y = 0$, or the material is not shearing and the stress is sub-yield, $f_y < 0$. For non-cohesive grains, C_1, C_2 are zero. For cohesive grains, C_1 and C_2 both manifest from the same microscale source, cohesive bonds at the grain contacts, so we assume both C_1 and C_2 are expressible in terms of a common characteristic cohesion stress, which we denote heretofore as σ_c.

Note that the constitutive equations above are rate independent. The dependence of shear stress on rate is typically low for granular intrusion problems, even rapid ones, because high pressure develops against the intruding surface, which counters the large shear rate in the inertial number definition [17]. For example, when intruders are shot into granular beds [27], the effect of rate is shown to be rather small ($< 10\%$) in terms of traveling depth and time. The constitutive model is also free of particle size effects, which is justifiable as long the length-scale of the locomotor is much larger than the grain scale [6, 28] including possible grain-size-based cohesion length-scales.

With the constitutive model just described, we next infer scaling relations for

[1] In 3D there are several choices one could make for the directionality (such as codirectionality v.s. double-shearing) and the definition of τ (such as Tresca's equivalent stress v.s. equivalent shear stress) and p (such as the normal stress on the flow plane v.s. the hydrostatic stress). But for any choice of the definitions, the same scaling laws come out as long as the model remains isotropic.

locomotion and check how well they hold against a number of DEM simulations. In so doing, this study is also a de-facto check on the validity of using the above basic continuum assumptions for these problems. We perform a dimensional analysis similar to that by Slonaker er al. [11]. For a wheel having large out-of-plane thickness D_W and characteristic in-plane length L, one can non-dimensionalize the driving inputs and constitutive parameters to express the velocity V of the wheel and power P expended by the wheel as follows:

$$\left[\frac{P}{Mg\sqrt{Lg}}, \frac{V}{\sqrt{Lg}}\right] = \Psi\left(\sqrt{\frac{g}{L}}t, f, \frac{g}{L\omega^2}, \frac{\rho_0 D_W L^2}{M}, \mu_s, \mu_w, \frac{\rho_0 g L}{\sigma_c}, \theta\right) \tag{2.1}$$

for some two-output scaling function Ψ. Here, t is time, the gravitational acceleration is g, the inclination of the bed relative to the direction of gravity is θ, the mass of the wheel is M, the rotational speed is ω, the shape of the wheel is represented by a set f, and μ_w is the friction coefficient of the wheel-bed interface. Each set of scaling tests below utilizes a fixed granular material and fixed wheel roughness so μ_s and μ_w can be absorbed into the undetermined Ψ function.

We study the validity of the above relation by splitting it into two sets of cases, which we shall analyze separately. We consider wheels traveling on inclined beds of non-cohesive particles, where the dimensionless number $\frac{\rho_0 g L}{\sigma_c}$ is not involved. Thus the relation becomes

$$\left[\frac{P}{Mg\sqrt{Lg}}, \frac{V}{\sqrt{Lg}}\right] = \tilde{\Psi}_1\left(\sqrt{\frac{g}{L}}t, f, \frac{g}{L\omega^2}, \frac{\rho_0 D_W L^2}{M}, \theta\right). \tag{2.2}$$

We also consider the case of wheels traveling on horizontal beds of cohesive granular media. Here, we can take away θ and the relation becomes

$$\left[\frac{P}{Mg\sqrt{Lg}}, \frac{V}{\sqrt{Lg}}\right] = \tilde{\Psi}_2\left(\sqrt{\frac{g}{L}}t, f, \frac{g}{L\omega^2}, \frac{\rho_0 D_W L^2}{M}, \frac{\rho_0 g L}{\sigma_c}\right). \tag{2.3}$$

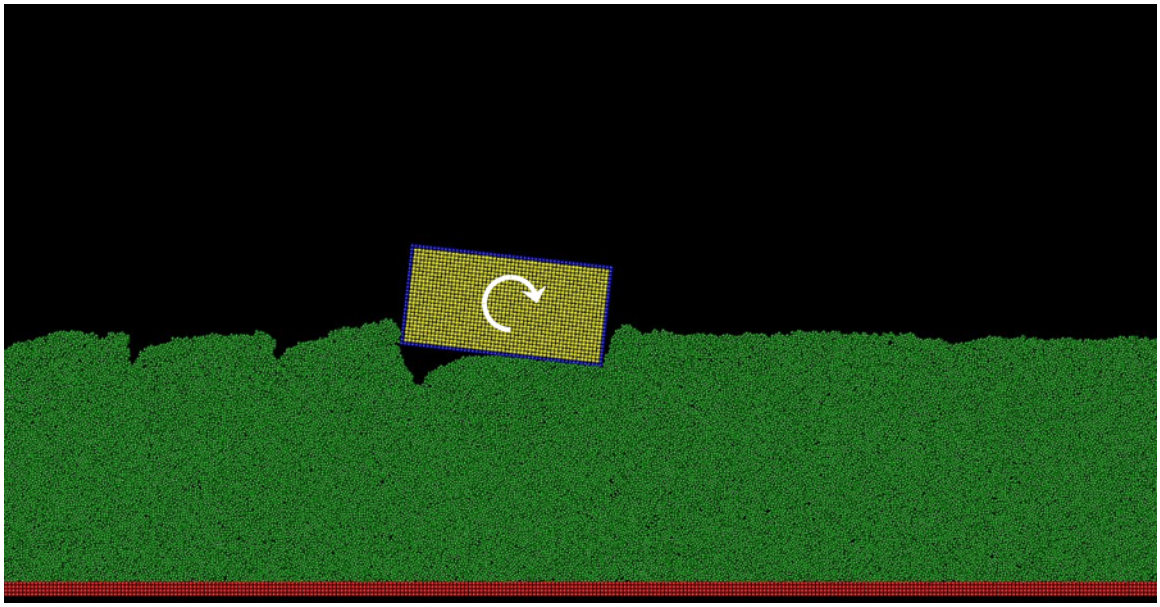

Figure 2-1: Example simulation system — case of a rectangular wheel in cohesive grains pictured. A wheel comprised of rigidly connected yellow inner particles and blue particles on the edge, is given a fixed rotation speed, which causes it to travel to the right. The particles in the bed are shown in green while the red particles at the bottom are fixed. The pictured domain width is about half of that of the whole simulated domain.

2.3 Numerical experiments

In order to test the proposed scaling relations, traveling wheels of different sizes and different shapes in different operating conditions are numerically simulated on horizontal granular beds of cohesive particles as well as inclined granular beds of non-cohesive particles using the open source software LAMMPS [29]. In all our numerical experiments, the granular beds are made of particles with a mean diameter of $\bar{d}$ =0.635 mm and the polydispersity is 20%. The solid density of grains is 2500 kg/m^3, close to the density of quartz. For non-cohesive granular beds, the contact model is Hooke's law in both normal and tangential directions, with damping in the normal direction and a frictional sliding coefficient of 0.4 [30, 31]. The stiffness k is set large enough that the hard particle limit is satisfied anywhere in the bed — that is, $p_b\bar{d}/k < 10^{-4}$, where p_b is the pressure in the bed due to the weight and motion of the material — and the damping corresponds to a restitution coefficient $e = 0.1$. The same values of the particle parameters have been used in previous studies [32, 11].

The cohesive particles also have an extra Lennard-Jones Potential to enable medium range attraction, as used in other researchers' work on cohesive particles [33, 34]. The radius at which distance the potential is minimum is set to be $\bar{d}$ and the potential is calculated within a cutoff of $2.5\bar{d}$. The depth of the potential well is 2×10^{-9}J. Our choice to use a fixed granular material for all scaled locomotion tests is for practical purposes, as it would be difficult in reality to have to "manufacture new sand" in order to utilize a scaling relation.

Because the scaling purports to apply to arbitrary wheel shapes, we consider three different shapes in this study: equilateral triangular wheels, rectangular wheels, and regular hexagonal wheels. All wheels are composed of particles having a uniform diameter $d_0 = 0.8\,\text{mm}$ rigidly connected to each other. The characteristic in-plane size L of the triangular and hexagonal wheels are represented by the side lengths, while for the rectangular wheels (aspect ratio 2:1) L is represented by the long side length. The mechanical properties of the outer layers (single or double layers) of the wheel particles are set to be the same as the particles in the granular bed to maintain a common wheel-grain and grain-grain contact interaction, while the density of the inner layers of the wheel particles can be tuned accordingly to scale the mass of the wheel in the study. The rotational velocity of the wheel is prescribed about the wheel's geometric center and the particles constituting the wheel move as a rigid body. When studying locomotion in a cohesive granular bed, the outer particles of the wheel also interact with the bed particles via the Lennard-Jones Potential described above.

The numerical experiments are quasi-3D (see FIG. 2-1) in the sense that the simulated domain has a depth of d_0 into the page (y direction) and periodic boundary conditions are applied in the y direction, allowing particles to move out-of-plane. Hence, the simulation represents a 'thick' wheel driving on a granular bed. Periodic boundary conditions are also applied in the x direction (wheel traveling direction). The bottom of the bed is made of fixed particles, representing a no-slip boundary condition. In the simulations with horizontal beds, the gravity points vertically downward. Tilted beds are treated by tilting the gravity vector.

2.4 Scaling law for wheels on inclined beds of non-cohesive grains

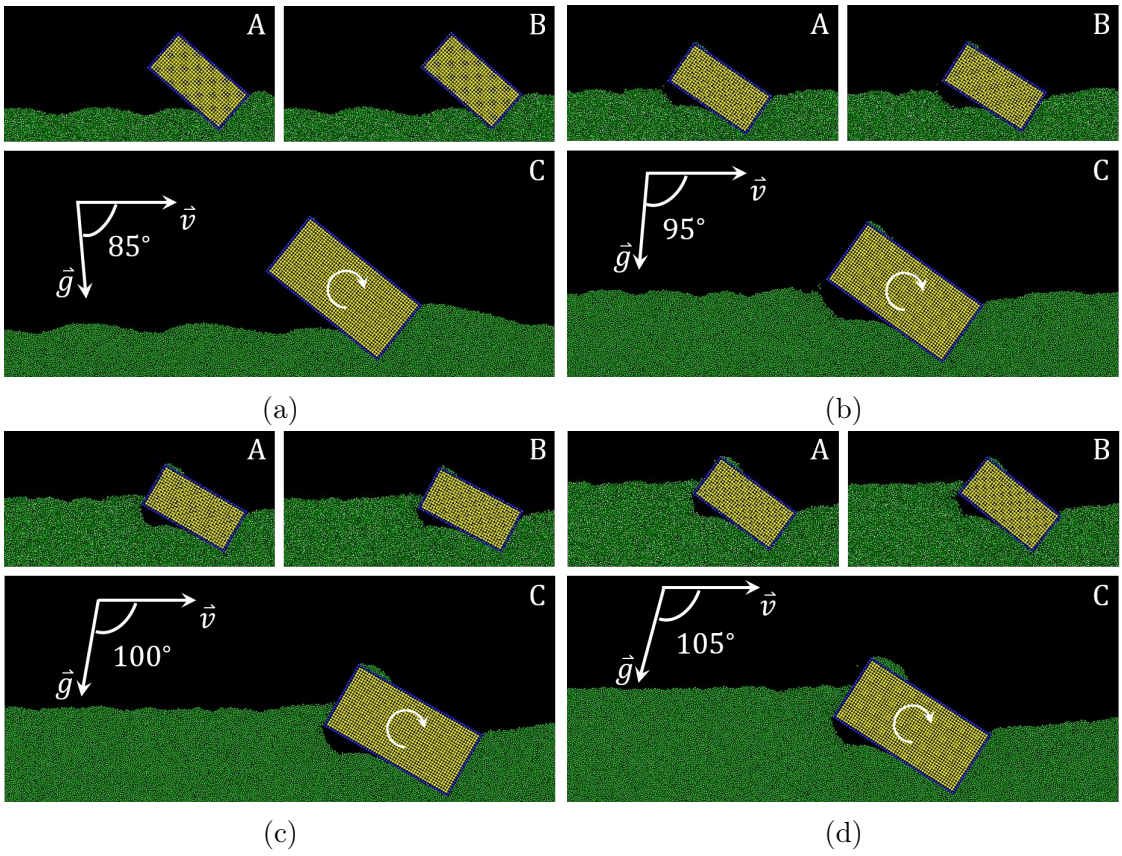

Figure 2-2: For each of (a)-(d), snapshots are shown of rectangular wheels at the same dimensionless time driving in non-cohesive particle beds at a particular tilt angle θ. The subfigures correspond to the supposed scale-equivalent test cases A, B, and C. The value of θ is (a) 85°, (b) 95°, (c) 100° and (d) 105°. The wheels spin clock-wise and travel to the right.

The numerical simulations of wheels traveling on inclined beds of non-cohesive particles consist of three groups corresponding to three different shapes: triangle, rectangle (aspect ratio 2:1), and hexagon. Each group adopts a set of three wheels of identical shape but different sizes or operating parameters: we denote them A, B and C, as shown in Table 2.1, where the value of the parameters are shown in Table 2.2 with the wheel particle size $d_0 = 0.8\,\mathrm{mm}$. The parameters of the wheels are designed according to Eq.(2.2) such that $g/L\omega^2$ and $\rho_0 D_W L^2/M$ are fixed across all wheels

sharing a common shape.

Table 2.1: Parameters of the wheels, in each group of the same shape, tested on inclined beds of non-cohesive particles at various angles.

Wheel	Size	M/D_W	ω	g
A	L_1	M_1	ω_1	g_1
B	L_1	M_1	$2 \cdot \omega_1$	$4g_1$
C	$k_1 \cdot L_1$	$k_1^2 \cdot M_1$	$\omega_1/\sqrt{k_1}$	g_1

Table 2.2: Value of the parameters for different wheel shapes, tested on inclined beds of non-cohesive particles at varying angles.

Shape	L_1/d_0	k_1	$M_1(\mathrm{kg\,m^{-1}})$	$\omega_1(\mathrm{rps})$	$g_1(\mathrm{m/s^2})$
Triangle	36	3/2	0.56	1	9.8
Rectangle	36 (length)	3/2	1.09	1	9.8
Hexagonal	18	4/3	0.77	1	9.8

Each set of three wheels are tested with four different angles between the traveling direction and the gravity: $\theta = 85°$ (downhill), $95°$ (uphill when $\theta > 90°$), $100°$ and $105°$. Due to the periodic boundary conditions in the traveling direction and the finite depth of the granular bed, the angles are constrained to a range that permits the bed to be static in the absence of a wheel, and to ensure that any flows set off due to impact by the moving wheel do not cause grains to pass through the periodic boundary and hit the front of the wheel, nor produce divots that expose or come close to the bottom wall of the bed.

First we present detailed results of the rectangular wheel simulations. Snapshots of those simulations at a fixed value of $\tilde{t}$ are compared in FIG. 2-2. It can be seen that for each tilt angle θ, the footprint and impression patterns of the three wheel cases (A,B, and C) are geometrically similar, which is a first indication that the scaling relations proposed are indeed scaling the relevant physics. More quantitatively, the dimensionless power $\tilde{P} = \frac{P}{Mg\sqrt{Lg}}$ and traveling velocity $\tilde{V} = \frac{V}{\sqrt{Lg}}$, as a function of dimensionless time $\tilde{t} = t\sqrt{g/L}$ comparisons of the set of three rectangle wheels on beds of non-cohesive particles, with different angles θ, are shown in FIG. 2-3. The dimensionless power and traveling velocity of the three wheels show strong agreement, supporting the proposed scaling relation for driving up (or down) inclined

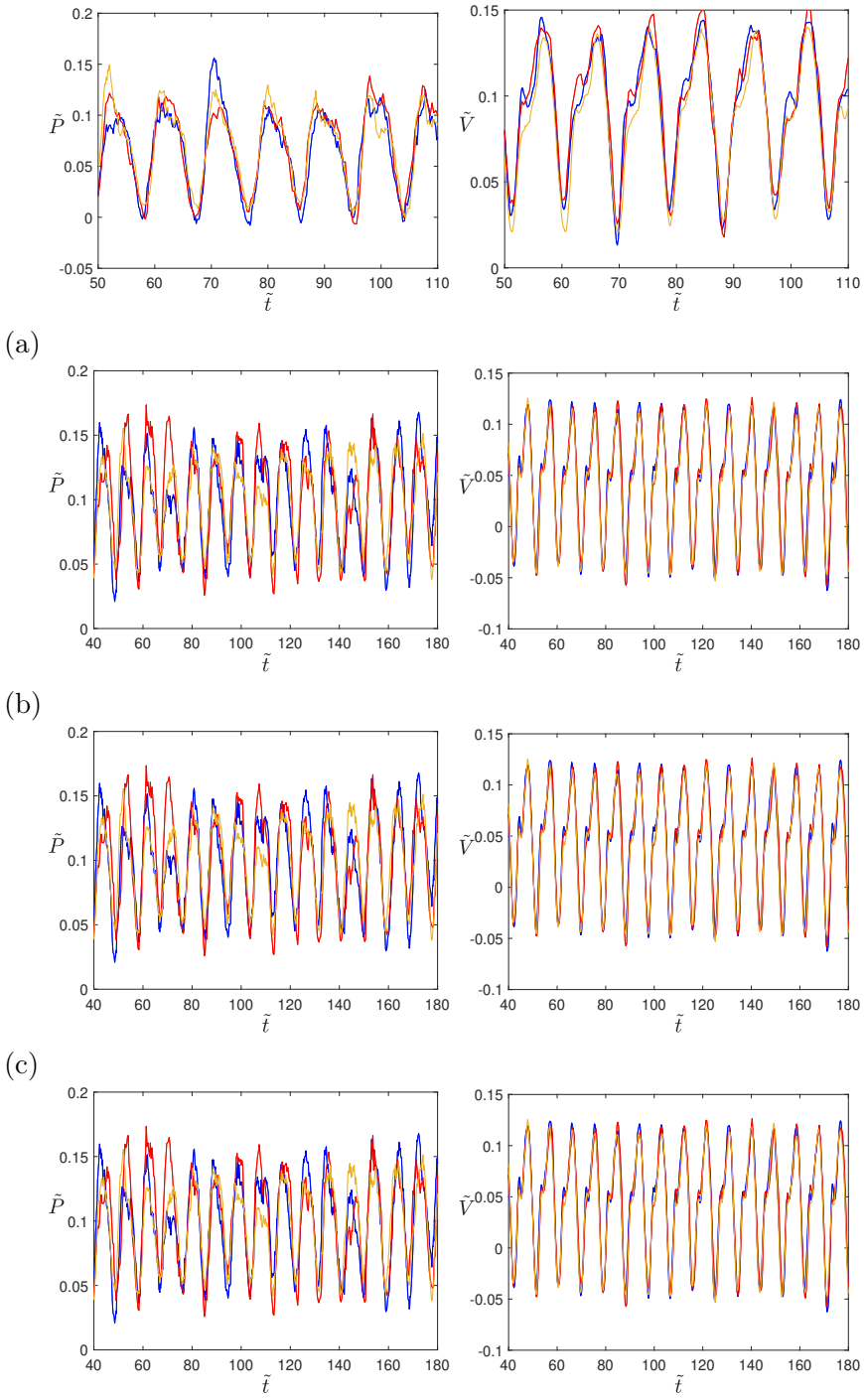

Figure 2-3: Dimensionless power and traveling velocity comparisons of a set of three rectangle wheels in beds of non-cohesive particles, with the angle θ between the traveling direction and the gravity (a) $\theta = 85°$, (b) $\theta = 95°$, (c) $\theta = 100°$, (d) $\theta = 105°$. Blue curves stand for case A, red for case B and yellow for case C.

terrains. More specifically, within the set of the three wheels, wheels A and C are under the same magnitude of gravity whereas wheel B is under a different gravity magnitude. This suggests the potential of the scaling law to be applied to locomotion in extraplanetary terrains.

The dimensionless power and traveling velocity of the rectangular wheels can be further averaged in each case and then plotted as a function of inclined angle as shown in FIG. 2-4, in comparison with the counterparts of different shapes. The data is averaged over a distance of at least five wheel “diameters" (maximum length across the wheel) on virgin bed surface in steady state. The scaling relation works well through different shapes, covering a range of inclination angles from uphill locomotion to downhill.

We also notice that the smaller triangle wheels (A and B) consume less power than the prediction ($\sim$ 10% less). This effect may be a result of size effects in granular flow rheology since the corners of the triangular wheels are sharp, causing penetration widths that compete with the grain size. The granular bed performs stronger when the interaction occurs at limited contacts and in thin layers, which makes the smaller triangular wheels prone to sink slightly less, so that driving over the surface requires less power. Similar size effects are also observed when we tried “bar wheels" (elongated rectangles with an aspect ratio of 9:1 with the short edges no longer than $6d_0$). As the size of the wheel becomes much larger than the grain size (low aspect ratio rectangles shown here) and corners less sharp (hexagons), the size effect diminishes and the scaling law works well. The notion that grain-size effects make ‘smaller act stronger’ in granular media is confirmed by experiments [35, 16, 36] and has been explained with nonlocal (grain-size-dependent) rheologies [6, 28, 37, 38, 39, 40].

2.5 Scaling laws for cohesive grains

To study the scaling relation on beds of cohesive particles, we have tested a set of three triangular wheels, three rectangular wheels, as well as three hexagonal wheels for generality. Dimensionless groups $g/L\omega^2$, $\rho_0 D_W L^2/M$ and $\rho_0 gL/\sigma_c$ are controlled

and the design of the wheels can be found in Table 2.3, where the parameters that are picked (see Table 2.4) produce reasonable wheel sinkages in the simulated domain.

Table 2.3: Parameters of the wheels, in each group of the same shape, tested on horizontal beds of cohesive particles.

Wheel	Size	M/D_W	ω	g
Small	$k_2 \cdot L_2$	$k_3^2 \cdot M_2$	ω_2/k_2	g_2/k_2
Medium	L_2	M_2	ω_2	g_2
Large	$k_3 \cdot L_2$	$k_3^2 \cdot M_2$	ω_2/k_3	g_2/k_3

Table 2.4: Value of the parameters for different wheel shapes on beds of cohesive particles.

Shape	L_2/d_0	k_2	k_3	$M_2(\mathrm{kg\,m^{-1}})$	$\omega_2(\mathrm{rps})$	$g_2(\mathrm{m/s^2})$
Triangle	36	2/3	3/2	0.57	1	9.8
Rectangle	36 (length)	2/3	3/2	0.54	1	9.8
Hexagonal	18	2/3	4/3	0.77	1	9.8

Figure 2-6 shows snapshots of the simulations at the same dimensionless time. The 'footprint' patterns left by wheels of the same shape but differing size show geometric similarity, a signature of the underlying scaling. Indeed, when the dimensionless wheel shapes are fixed (same f) and dimensionless groups $g/L\omega^2, \rho_0 D_W L^2/M, \rho_0 g L/\sigma_c$ are controlled to be the same, the power P and traveling velocity V appear to scale as in Eq.(2.3), as evidenced in FIG. 2-5. Both the triangular and rectangular wheels dimensionless power and velocity as functions of dimensionless time match well, respectively. The hexagonal wheels have noisier time-dependent profiles, however the time averaged values match best among all the tested shapes: $\tilde{P}$ within a difference of 1.0% and $\tilde{V}$ within a difference of 6.0% relative error with respect to the mean values of the time averaged power and velocity, whereas the relative error of power and velocity are within 2.9% and 8.4% for rectangle wheels, 7.5% and 7.7% for triangle wheels. The scaling relation seems to be more robust to sharp corners; it appears the triangular wheels scale better in cohesive versus non-cohesive particles.

Due to the cohesive nature of the particles, the gravity g and the characteristic length L produce the dimensionless group $\rho_0 g L/\sigma_c$. Observe that when the granular material and gravity are fixed, this group can only stay fixed if L is unchanged.

Conversely, a test in one gravity to predict behavior in another comes with a specific size-scaling rule. For example, to test a Mars rover on Earth in a soil matching the behavior of Martian soil, the dimensionless group $\rho_0 g L/\sigma_c$ dictates that the size of the wheel to be tested on the Earth should be scaled to $(g_{\text{earth}}/g_{\text{mars}})^{-1} = 0.38$ times the size of the one intended for Mars. Other testing parameters can be decided by matching the dimensionless numbers in Eq.(2.3). Besides investigations involving variations in gravity, the scaling of wheel size in cohesive grains is also possible if one is able to directly control and vary the granular cohesion stress, σ_c, which would presumably require control over the physical mechanism causing particle attraction.

Lastly, we point out that there are many types of cohesive granular interaction models (such as capillary models [41, 42], van der Waals interactions [33], the powder chemistry model [43], the liquid bridging model [44], DLVO theory [45]) and we are using just one of them: a van der Waals type medium range interaction to account for the cohesive forces. Though the interactions and flow behaviours of cohesive granular materials are more complicated than non-cohesive, the chapter presented here suggests that a simple scaling law exists to predict the driving performance of wheels on cohesive granular beds, as long as the cohesive length scale is small enough that a characteristic cohesion strength σ_c is the only relevant variable.

2.6 Concluding remarks

In this chapter, scaling relations for driving performance, namely the power and traveling velocity, have been proposed for wheeled locomotion on inclined and cohesive granular beds. For verification, DEM simulations of different shaped wheels have been performed and the results have confirmed the proposed scaling relations. These scaling relations shed light on how to design experiments in laboratory scales and/or in a different gravitational environment by following the dimensionless groups. For example, consider two driving experiments in the same (non-cohesive) grains having common wheel shape f, where one system has inputs $(g, L, M, D_W, \omega, \theta)$ and the other has $(g', L', M', D'_W, \omega', \theta') \equiv (qg, rL, sM, sr^{-2}D_W, q^{1/2}r^{-1/2}\omega, \theta)$, where q, r, s

are arbitrary scalars that can be selected by the user. Then, by Eq 2.1, these two tests have matching dimensionless inputs and ought to obey similitude. If the grains used in the pair of tests are also cohesive, Eq 2.1 would now require $r = 1/q$ in order to secure dynamic similarity, thereby removing one free parameter from the design space for the scaled test. However, if σ_c can be tuned in the locomotion experiments, then three free parameters reemerge in the cohesive case. Because the scalings were obtained assuming a local granular rheology, they are more accurate when the grain size is indeed negligible compared with wheel length-scales, since small-body intrusion effects may bring out rheologically nonlocal contributions in the granular media. For example, wheels with very narrow features or wheels that do not protrude into the bed deeply enough compared to the grain size may not satisfy the scalings as well.

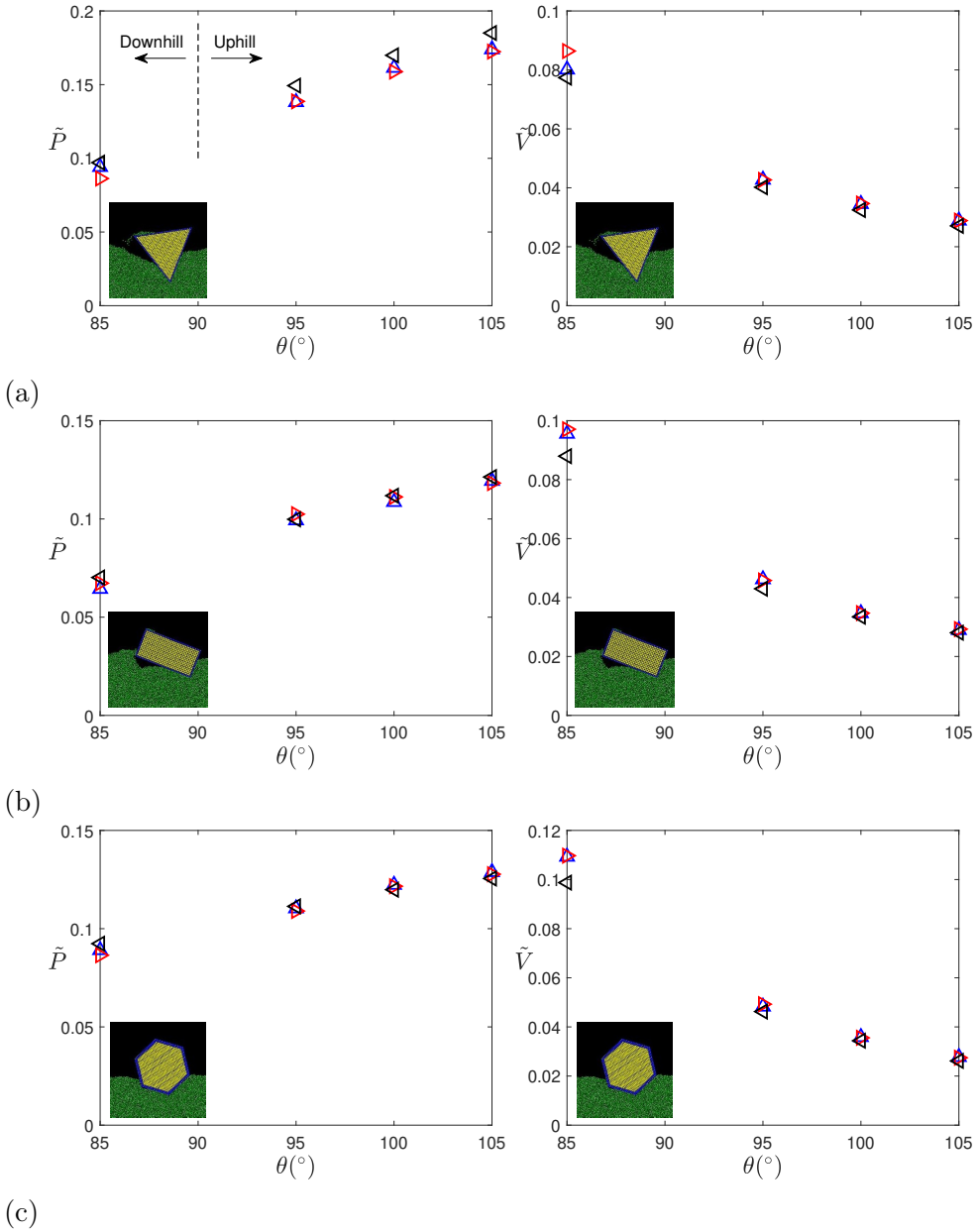

Figure 2-4: Averaged dimensionless power and traveling velocity comparisons of (a) triangular wheels, (b) rectangular wheels and (c) hexagonal wheels, at different inclined angles. Case A represented by blue markers, case B red, and case C black.

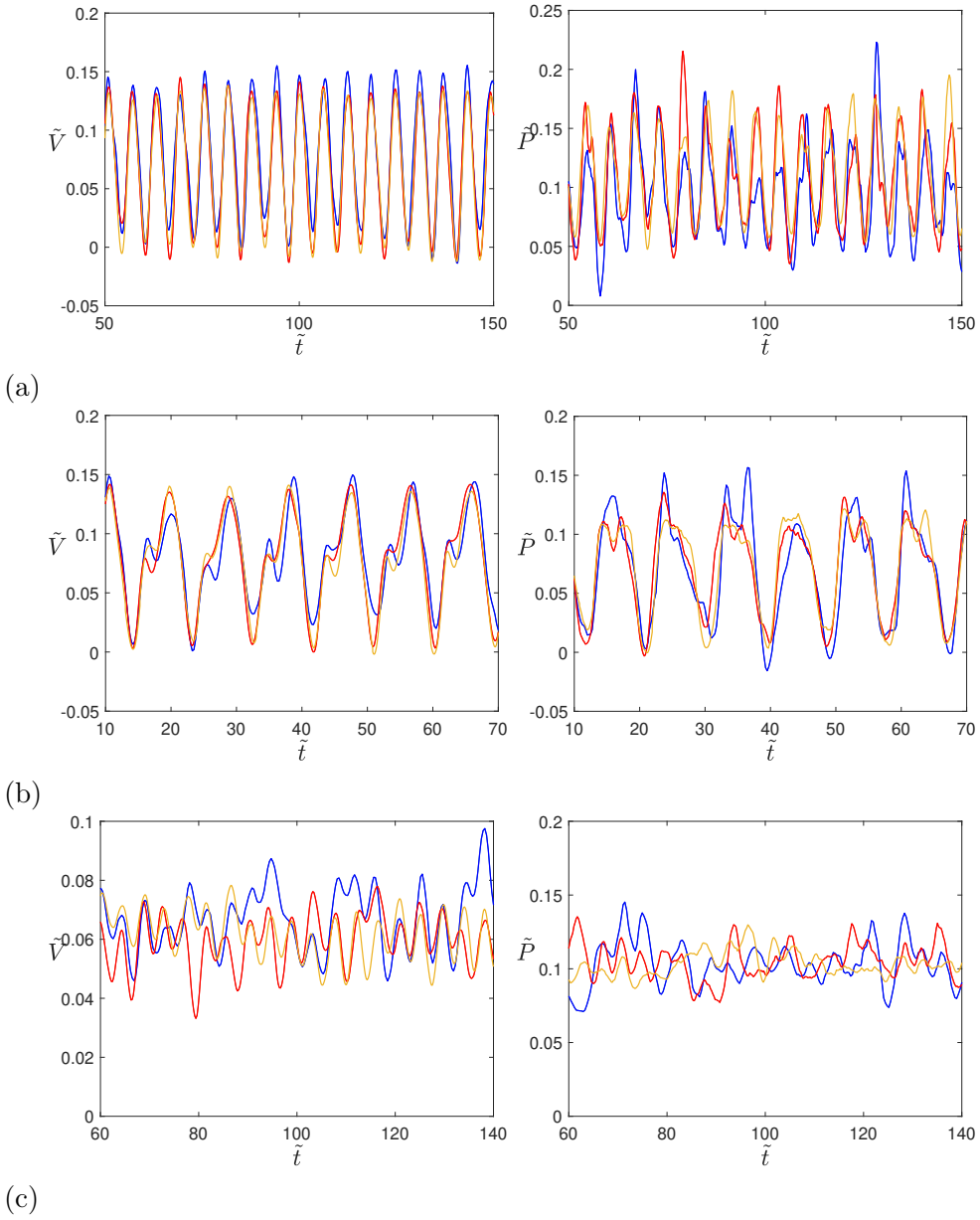

Figure 2-5: Dimensionless power and traveling velocity comparisons of (a) a set of three triangle wheels, (b) a set of rectangle wheels and (c) a set of hexagonal wheels on horizontal beds of cohesive particles. Blue curves stand for Small wheels, red curves for Medium wheels and yellow curves for Large wheels.

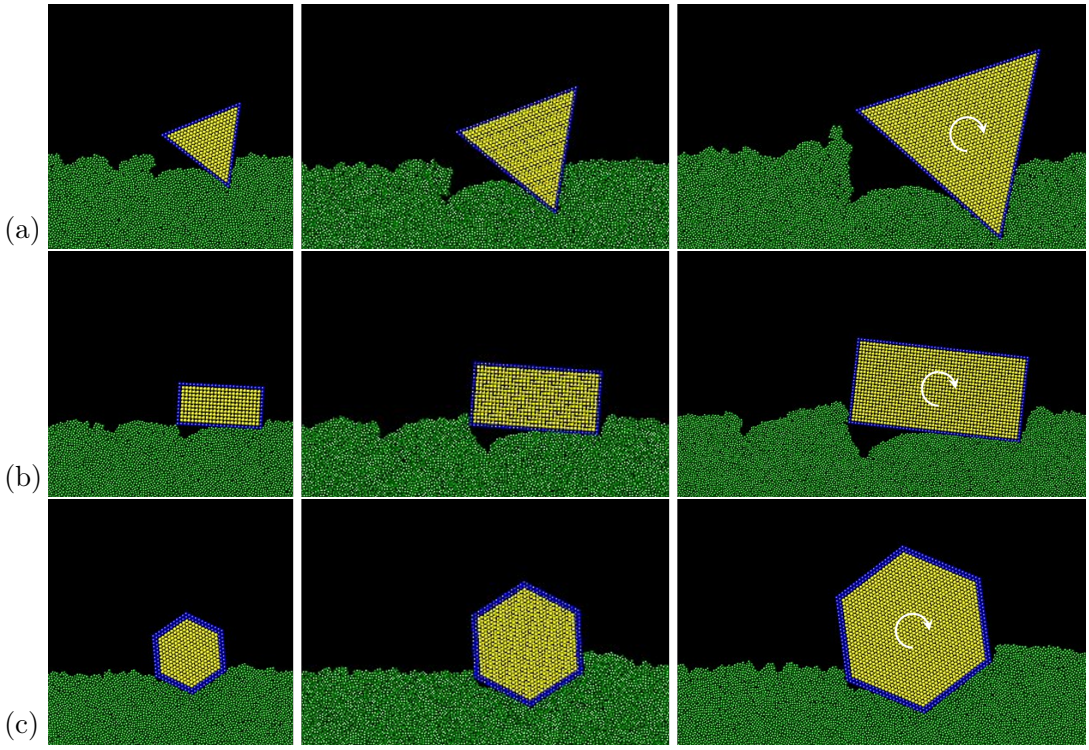

Figure 2-6: Snapshots at the same $\tilde{t}$ of the differently shaped/sized wheels in horizontal cohesive particle beds: (a) triangular wheels, (b) rectangular wheels, and (c) hexagonal wheels. All tests use the same DEM grains. Different wheel sizes are compared in different columns: Small in the first column from the left, Medium in the second column and Large in the third column. The wheels spin clock-wise and travel to the right.

Chapter 3

Fluid-driven transport of round sediment particles

This chapter includes results previously published by this author in Zhang et al., 2022 [46]. The movies referred to in the chapter can be accessed in the Supporting Information section of the publication.

3.1 Background

Fluid-driven sediment transport, in which a flow passing over a loose granular bed entrains and moves the grains, plays a pivotal role in many natural and engineered landscapes. Common scenarios that require the calculation of sediment transport rates include conveyance of sediment through engineered channels, infilling of artificial reservoirs, dispersal of stored sediment following dam removal, and long-term sediment transport that shapes natural rivers [47, 48]. Applications like these create a demand for sediment transport models that can be applied over a wide range of flow conditions and sediment characteristics.

However, calculation of sediment transport rates over a wide range of conditions is a challenging task. Sediment transport at the scale of a river channel depends on the fine-scale interaction of a turbulent flow with many individual sediment grains. Moreover, variations in these fluid-grain interactions through time, or with height above or

below the sediment bed, can create different regimes of grain motion [49], including creep of closely packed grains, a rapidly shearing slurry, or a dilute suspension.

Bedload sediment flux, in which grains move by rolling, sliding or hopping along the bed, is practically described by field-scale sediment transport models which are typically derived semi-empirically by comparing the bulk characteristics of flows, such as average bed shear stress, with observations of bulk sediment transport rates from laboratory flume experiments [8, 50, 51, 52, 9]. Less commonly, field monitoring studies are used [53, 47]. Some widely used bedload transport relations are listed in Table 3.1, where the dimensionless sediment transport rate (the Einstein number) is

$$q^* \equiv q_s \Big/ \left(d_p \sqrt{\frac{\rho_s - \rho_f}{\rho_f} g d_p} \right), \tag{3.1}$$

with q_s the sediment volume flux per unit flow width, d_p the grain diameter, and ρ_s and ρ_f the sediment and fluid densities. The dimensionless bed shear stress, often referred to as the Shields number, is

$$\tau^* \equiv \tau_b \big/ \left[(\rho_s - \rho_f)\, g d_p \right], \tag{3.2}$$

with g the gravitational acceleration. τ_b is the bed shear stress, which is the driving factor in the sediment transport process. For example in a infinite wide river with a bed slope of S and a water depth of H, the bed shear stress can be calculated as $\tau_b = \rho_f g H S$. Most bedload transport relations have a critical value of the Shields number τ_c^* at which grains begin to move [54], and most converge to a power law of 3/2 for $\tau^* \gg \tau_c^*$, but differ if τ^* is close to the threshold of grain motion [55]. Recently, Pähtz and Durán [56] proposed a formula in which $q*$ scales with $\tau^* - \tau_c^*$ linearly for $\tau^* \to \tau_c^*$ and quadratically for $\tau^* \gg \tau_c^*$ through numerical simulations, indicating the 3/2 power law may be an approximation between these two ends.

These semi-empirical models have the desirable characteristic that they are easy to apply in natural and experimental settings, and they are therefore widely used. However, even under controlled laboratory conditions, empirical bedload transport

Table 3.1: Widely used bedload transport relations.

Author(s)	Dimensionless transport rate q^*	Critical Shields # τ_c^*
Meyer-Peter and Müller [8]	$q^* = 8(\tau^* - \tau_c^*)^{3/2}$	$\tau_c^* = 0.047$
Ashida and Michiue [50]	$q^* = 17(\tau^* - \tau_c^*)(\sqrt{\tau^*} - \sqrt{\tau_c^*})$	$\tau_c^* = 0.05$
Engelund and Fredsøe [57]	$q^* = 18.74(\tau^* - \tau_c^*)(\sqrt{\tau^*} - 0.7\sqrt{\tau_c^*})$	$\tau_c^* = 0.05$
Fernandez-Luque and Van Beek [51]	$q^* = 5.7(\tau^* - \tau_c^*)^{3/2}$	$\tau_c^* = 0.037 \sim 0.0455$
Wong [9]	$q^* = 3.97(\tau^* - \tau_c^*)^{3/2}$	$\tau_c^* = 0.0495$

expressions commonly over- or under-predict sediment flux by more than a factor of two [55]; and larger disagreements in natural settings are common: Reid and Laronne [58] compiled the data from 6 streams and found that q^* can vary by a factor of 10 across tests with τ^* fixed at $\tau^* = 0.02$ and more than 100 (up to 1000) when $\tau^* \sim 0.1$. Correction factors for q^*, τ^* and τ_c^* for steep slopes can be obtained from recent works [59, 56]. However, the variability is evident even in sediment transport experiments on gentle slopes, such as Meyer-Peter and Müller [8] in which the slope $S < 0.02$ and the above slope correction factors are close to 1. What is causing the variation in flux (q^*) for a given Shields number (τ^*) on gentle slopes? The empirical transport expressions are also remarkable for what they do not contain, such as any dependence on sediment geometric or surface characteristics other than a representative grain diameter. There are reasons to expect that grain-scale phenomena influence channel-scale sediment transport, but which grain-scale phenomena do we need to consider?

One way to address this question is to simulate the grain-scale mechanisms that entrain and transport sediment. Recent computational and methodological advances have made it feasible to numerically investigate the mutual interactions of many sediment grains and a turbulent flow, allowing for interrogation of transport phenomena at a level of detail that is difficult to achieve even in well-instrumented experiments. Simulations in which the sediment particles are treated as discrete elements can be classified into two types based on the way the fluid-particle interaction is handled: (1) the fluid grid size is much smaller than the particle size so that the fluid-particle interaction can be resolved [60]. And (2) the fluid grid size is comparable to or larger than the particle size and the fluid-particle interaction is modeled by a drag (hydrodynamic force) law [61, 62], and potentially also a hydrodynamic torque model [63, 64].

Most of the simulations examining the sensitivity of the transport relation to the microscopic particle parameters adopt the second type for the higher computational efficiency; e.g. recent studies [65, 66, 67, 68] have found that the transport relation is insensitive to the particle surface friction coefficient and the restitution coefficient. But these simulations do not include the hydrodynamic torque on particles, which may be important since rolling has lower threshold than sliding in entrainment events [69]. The lack of fluid-particle angular momentum exchange may cause problems in the other direction as well: the rotation of a single sediment particle near the bed surface influences the fluid vortex structure nearby which in return changes the hydrodynamic forces [70]. Also, for grains near the bed surface where we would want the most accuracy, the separation of length scales presumed in a drag model might not be applicable due to the jump in volume fraction, which could render the drag model less accurate. These questions matter most for sediment transport close to τ_c^*. Laminar transport simulations [71], which resolve the fluid-particle linear and angular momentum exchange, have shown that the rolling mode in the incipient motion requires nonzero surface friction coefficient, but the specific value of the friction coefficient has only marginal influence. But its effect is still not known in turbulent sediment transport. These considerations motivate revisiting the parameter space, especially the microscopic particle parameters (such as the friction coefficient and the restitution coefficient), using turbulent sediment transport simulations which resolve the fluid-particle interaction at a sub-grain scale.

However, even if grain-resolving simulations give us all the answers, they are currently impractical to implement at field scale (i.e. the scale of a river channel). So one option, as a complementary approach, would be to use them to help parameterize/validate a continuum model that could be scaled up more easily and captures the rheological behavior of grains and fluid in different regions of the bed and the flow. As noted previously, a given fluid stress can cause grains at different heights below or above the sediment bed to move in different granular flow regimes, ranging from a thick creeping layer to a dense slurry to a dilute suspension. Houssais et al. [49] analyze the threshold of grain motion from this perspective, and show in a set of

laboratory experiments that the transition from no motion to bedload transport as τ^* increases is a gradual transition (as opposed the discontinuous transition implicitly assumed by equations in Table 3.1) characterized by progressive quickening of granular creep throughout a layer that extends many grain diameters below the bed surface. They additionally propose a regime diagram for sediment transport in which the style of grain motion (creep, bedload, or dilute) depends on the height relative to the bed surface and the transport stage, τ^*/τ_c^*. This alternate perspective on sediment transport implies that it may be possible to improve predictions of sediment flux by describing these granular regimes with appropriately coupled rheological models rather than fitting a single function to experimental data over a range of $\tau^* - \tau_c^*$.

In this chapter, in order to understand the variability of sediment flux (q^*) at a given Shields number (τ^*), we examine three questions: (i) How important is fluid-particle angular momentum transfer and in which part of the flow and in which regime of the sediment transport is it important? We fully resolve the grain-scale spherical particle movement and study the fluid-particle angular momentum exchange studied in an entrainment event. Then it is quantified as a "rotation stress" whose profile is examined in different transport stages and further correlated to the transport relation. Our work here is benchmarked by flume experiments [72, 73] in which grain-scale motions were tracked. (ii) What is (not) responsible for the variability in the observed sediment transport relation? We explore the parameter space (macroscopic river settings such as slope, and most importantly microscopic particle parameters such as the mean size, surface roughness, and grain contact damping) to see what is responsible for the variability in the relation between the Einstein number and the Shields number in turbulent sediment transport. (iii) How can we formulate a useful model broadly applicable at different scales across the range of bedload sediment transport behaviors? We use the DEM-LBM simulation data to derive continuum models of sediment transport that apply to a range of flow conditions and sediment characteristics. For simplicity, we will limit our investigation to the bedload sediment transport of mono-disperse particles without considering vegetation [74, 75], external agitation of the turbulence [76, 77, 78], or channel morphology that is known to

influence the transport relation, such as bedform patterns [79, 80] or the presence of large (possibly not fully submerged) boulders [81].

3.2 Discrete simulations

A few geoscience-oriented studies have begun to probe the physics of grain-scale sediment motion through numerical experiments [82, 61, 62, 83]. Schmeeckle [61] pioneered this approach in geomorphology by coupling discrete element method (DEM) simulations of grain motion with large-eddy simulations (LES) of turbulent flow. He found that coherent flow structures impinging on the bed are a major cause of sediment entrainment, and he measured a power-law relationship between q^* and τ^* that is similar to (but somewhat steeper than) the widely used bedload transport expression [84, 8]. The LES-DEM approach employed by Schmeeckle [61], a variant of the general CFD-DEM method (CFD: computational fluid dynamics) for the fluid and particles, does not explicitly model flow around grains or particle-scale pressure variations (e.g. lubrication forces). Instead, the flow and grains are coupled with spatially averaged body forces. Nonetheless, his promising results suggest that direct simulations of sediment transport with tighter fluid-grain coupling will yield even more insight into the controls on bedload flux. In recent years, more researchers have studied sediment transport problems using similar CFD-DEM simulations. For example, Hill and Tan [83] studied the influence of the added fine particles on the mobilization of gravel beds using LES-DEM. Maurin et al. [59] and Pähtz and Durán [56] studied slope influence in sediment transport and have proposed slope corrections for q^*, τ^* and τ_c^* for steep slopes. Finn et al. [63] simulated particle dynamics on wavy bottoms. Most recently, Guan et al. [64] studied Kelvin–Helmholtz vortices' influence on local and instantaneous bedload sediment transport with the same numerical method as Finn et al. [63].

For sub-particle resolution of the fluid-grain interaction, the Lattice Boltzmann Method (LBM) [85] is able to resolve the fluid-particle interaction at the moving particle boundaries [86, 60, 87] by treating the fluid material as hypothetical fluid

particles marching in space and colliding with the solid particle boundaries. Coupled DEM-LBM simulations can fully resolve the fluid-particle interaction in sediment transport problems and offer more understanding about the grain-scale mechanisms.

In the following discussion of the particle-scale simulations, we first introduce the DEM-LBM numerical method. Second, we present simulations matching the conditions of flume experiments [72, 73] to provide a relevant many-particle test of the methodology. Third, we present wide wall-free simulations in order to study the factors that can potentially cause the variability seen in experimental transport data on gentle slopes.

3.2.1 Method: DEM-LBM

The translation and rotation of the sediment particles in our DEM-LBM simulations are integrated from the equations of motion of individual particles using the Velocity Verlet method [88], which is widely used in DEM simulations of granular materials and is implemented in common software such as LAMMPS [29] and LIGGGHTS [89]. The particle-particle interaction is elastic with damping effects in the normal direction, which can be simulated as a spring-dashpot model, and the interaction is elastic with friction in the tangential direction.

The DEM algorithm is fully coupled to a LBM solver, which can resolve the traction over many moving boundaries (grain surfaces in our case). Chen and Doolen [90] review the history of this numerical method, and Aidun and Clausen [91] review the application of LBM to complex flows. Inspired by the Boltzmann-Maxwell Equation, LBM recovers the Navier-Stokes equations [85] by treating the fluid material as hypothetical fluid packets that collide and stream in a discrete set of directions. The method is particularly advantageous for solving problems with many moving boundaries and the simple form makes implementation straightforward.

In a standard LBM algorithm, the domain is discretized into a uniform orthogonal grid. The fluid material exists in the 3D domain only on the nodes in a certain discretized dimensionless velocity set $\{\boldsymbol{c}_i\}$. In this chapter, we choose a discretization composed of of 19 directions, known as D3Q19, as shown in Figure 3-1(a). The

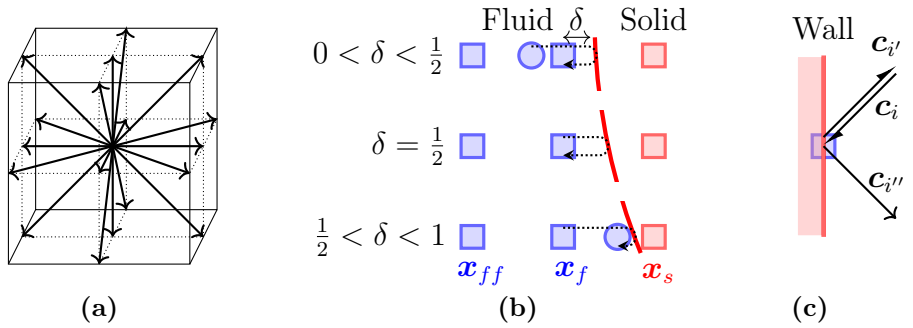

Figure 3-1: Lattice Boltzmann Method: (a) The velocity set of D3Q19: 18 velocities streaming out from the node to the next nearest nodes in the velocity directions and a rest velocity staying at the original node (b) Particle boundary treatment in LBM, depending on δ the distance from the last fluid node to the boundary in terms of lattice units. $\boldsymbol{x}_f$ is the fluid node next to a solid node $\boldsymbol{x}_s$, and $\boldsymbol{x}_{ff}$ is the neighbor fluid node upstream. (c) Related velocities near a stationary wall (the fluid node is aligned with the wall): the fluid parcel coming in $\boldsymbol{c}_i$ will be bounced back into the opposite direction $\boldsymbol{c}_{i'}$ at a no-slip wall, and will be reflected specularly into $\boldsymbol{c}_{i''}$ at a free-slip wall.

fluid material at a point is represented by “fluid parcels" streaming in 18 directions with magnitudes that move the parcels to the nearest node in the velocity direction through each LBM timestep (with the 19th parcel just resting at the original node). Each of the parcels corresponds to a distribution function component f_i satisfying $\Sigma_{i=0}^{18} f_i = 1$. In a fluid timestep, as shown in Eq 3.3, the fluid undergoes a collision (right-hand side) and a streaming operation (left-hand side) sequentially:

$$\underbrace{f_i(\boldsymbol{x}+\boldsymbol{c}_i, t+1) - f_i(\boldsymbol{x}, t)}_{\text{Streaming}} = \underbrace{\frac{1}{\tau}\left[f_i^{eq} - f_i\right]}_{\text{Collision}}, \tag{3.3}$$

where $\boldsymbol{x}$ is the dimensionless position, τ is the dimensionless relaxation time and f_i^{eq} is the equilibrium distribution function. All the quantities are nondimensionalized by the grid size dx, LBM timestep dt_f, and ρ_f. In the collision operation, f_i^{eq} is a function of the macroscopic fluid velocity and density, and τ is a function of the local fluid kinematic viscosity ν [92]:

$$\tau = \frac{1}{2} + \frac{3\nu}{dx^2/dt_f}. \tag{3.4}$$

For turbulent flow, a Large Eddy Simulation (LES) method [92] can model the subgrid-scale eddies. We use the Smagorinsky turbulent closure [93]:

$$\nu = \nu_f + \nu_t, \quad \nu_t = (C_s \cdot dx)^2 \dot{\gamma}_f, \tag{3.5}$$

where ν_f is the kinematic viscosity of the pure fluid, ν_t is the turbulent viscosity, C_s Smagorinsky constant, and $\dot{\gamma}_f$ the fluid local shear rate. C_s is shown to be dependent on the discretization and geometry [94, 95]. We calibrate $C_s = 0.27$ in the flume geometry (see A for details and for validation of the pure fluid simulations) with grid size $dx = 0.5$mm. The value of C_s and the grid spacing are used throughout this chapter for the simulations in which the fluid is water. Body forces such as gravity can be taken into account by adding an extra term to the collision step [96]. More details on how to construct a macroscopic variable such as $\dot{\gamma}_f$ from the distribution $\{f_i\}$ can be found in [92].

For a post-collision distribution function component f_i^c at the fluid node $\boldsymbol{x}_f$ next to a solid node $\boldsymbol{x}_s$, when the corresponding parcel hits a fixed solid boundary that sits in the middle of a link, it will bounce back and end up with the opposite direction $f_{i'}(\boldsymbol{x}_f, t+1) = f_i^c(\boldsymbol{x}_f, t)$, where $f_{i'}$ denotes the component in the opposite direction of f_i. As shown in Figure 3-1(b), when δ the distance from the last fluid node to the boundary is not exactly 0.5, the component $f_{i'}(\boldsymbol{x}_f, t+1)$ can be interpolated [97]. For $0 < \delta < \frac{1}{2}$, the interpolation happens before the streaming

$$\begin{aligned} f_{i'}(\boldsymbol{x}_f, t+1) &= f_i^c(\boldsymbol{x}_f + (2\delta - 1)\boldsymbol{c}_i, t) \\ &= 2\delta f_i^c(\boldsymbol{x}_f, t) + (1 - 2\delta) f_i^c(\boldsymbol{x}_{ff}, t), \end{aligned} \tag{3.6}$$

whereas for $\frac{1}{2} \leq \delta \leq 1$, interpolation happens after the streaming

$$\begin{aligned} f_{i'}(\boldsymbol{x}_f, t+1) &= \frac{1}{2\delta} f_{i'}(\boldsymbol{x}_f + (2\delta - 1)\boldsymbol{c}_i, t+1) + \frac{2\delta - 1}{2\delta} f_{i'}(\boldsymbol{x}_{ff}, t+1) \\ &= \frac{1}{2\delta} f_i^c(\boldsymbol{x}_f, t) + \frac{2\delta - 1}{2\delta} f_{i'}^c(\boldsymbol{x}_f, t), \end{aligned} \tag{3.7}$$

For moving solid boundaries, the no-slip boundary condition can be modified according to the velocity of the particle boundary due to translation and rotation [97]. In our flume simulations (Section 3.2.3), since the thickness of the boundary layer at the glass side walls is smaller than (or comparable to) the grid size dx, we developed a new boundary technique that accounts for the boundary layer implicitly through a matched slip boundary condition. See Appendix A for more details. At a free-slip boundary, the parcel will specularly reflect instead of bounce back [98] as shown in Figure 3-1(c). As indicated above, all the LBM boundary conditions are processed in the streaming operation.

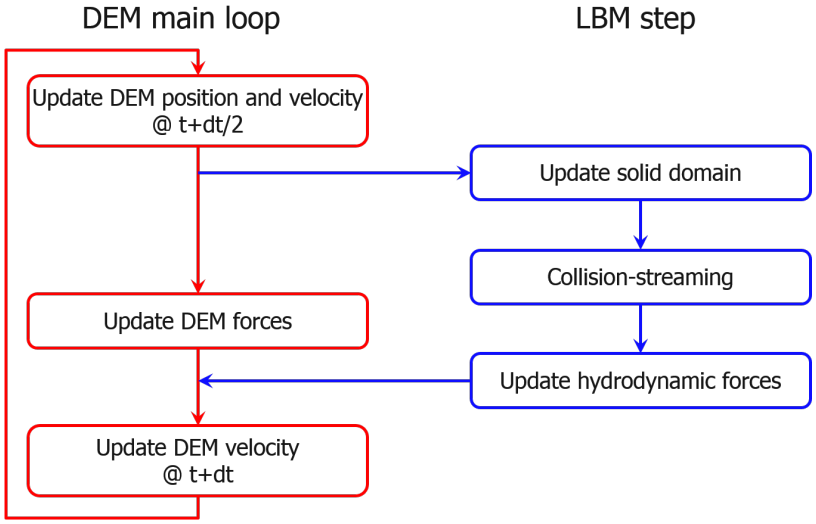

Figure 3-2: DEM-LBM coupling scheme.

The DEM-LBM coupling scheme is shown in Figure 3-2. The local parcel momentum changes can be used to integrate the force and torque on individual particles exerted by the fluid [99]. In this way, the fluid feels the moving particles through the moving interfaces, and the particles feel the fluid via the integrated hydrodynamic forces and torques. These will be used in the DEM scheme to update the linear and angular acceleration of the particles. Note that the timestep of the DEM dt to resolve the elastic interaction of particles [17, 6] is smaller than the timestep of the LBM $dt_f = dx/c_s$, where c_s is the fluid sound speed. dt_f is chosen so that the corresponding sound speed $c_s = dx/dt_f$ guarantees that the maximum Mach number

is below 0.3, in the incompressible limit [100], and the distance a particle travels in a "free flight" is less than $0.02dx$ (mostly $< 0.01dx$) [60]. In the DEM-LBM simulations presented in this chapter, a LBM step is called every 50 DEM steps to update the hydrodynamic forces and torque. If the DEM algorithm uses the particle-wise hydrodynamic forces (and torque) in the current LBM steps to update the particles' linear and angular acceleration, the interstitial fluid may experience numerical oscillations. As a remedy, the particle-wise hydrodynamic forces (and torque) in the current and the previous LBM steps are averaged when conducting the DEM update. When a particle is close to another particle or a wall, the algorithm searches for the upstream fluid information $f_i^c(\boldsymbol{x}_{ff}, t)$ or even $f_i^c(\boldsymbol{x}_f, t)$ in Eq 3.6 and Eq 3.7 which may be no longer physically available. Special care must be taken to update the fluid domain information as well as to calculate the corresponding fluid-solid momentum exchange. For these near contact scenarios, the needed upstream fluid distribution function component, $f_i^c(\boldsymbol{x}_{ff}, t)$ or $f_i^c(\boldsymbol{x}_f, t)$, is evaluated as the (Maxwell) equilibrium distribution using the grain velocity at the node if the search for the upstream fluid node goes into a node occupied by another particle. If the search goes out of the wall of the flume, then it comes back to the domain (see $\boldsymbol{c}_{i''}$ as shown in Figure 3-1(c)).

By refining the resolution of LBM with respect to the particle size d_p, Feng and Michaelides [101] and Derkse [102] have shown that a resolution of $dx \leq d_p/6$ or $dx \leq d_p/8$ is adequate for sufficiently accurate results. Here in this chapter, $dx \leq\sim d_p/10$ is kept to guarantee enough accuracy. To run our method, we have extended a custom-written program described in Mutabaruka et al. [103] and Mutabaruka and Kamrin [104].

3.2.2 Validation: single sphere settling, bouncing and rotation

The DEM-LBM algorithm is validated at the grain scale in tests of the particle-fluid linear and angular momentum exchange

As a validation of the DEM-LBM algorithm, single particle tests are performed to examine the liner and angular momentum exchanges between fluid and solid as well as the resolved lubrication force between close moving solid boundaries. When an

Table 3.2: Material properties in the single sphere tests

		Settle	Bounce	Rotate
ρ_f	[kg·m^{-3}]	970	1203	1000
η	[Pa·s]	0.373	0.0502	0.833
ρ_s	[kg·m^{-3}]	1120	7780	2550
d_p	[mm]	15	9.5	5.2

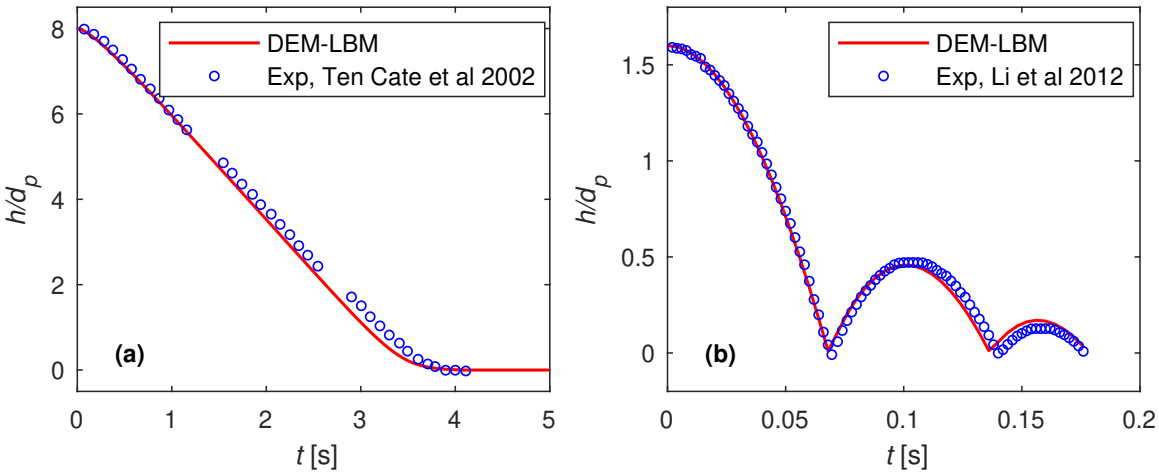

Figure 3-3: Results of the single sphere tests as Validation of DEM-LBM. Sphere normal trajectory comparisons with experiments for (a) settling and (b) bouncing.

immersed particle impacts a flat surface perpendicularly, the restitution coefficient depends on the Stokes number on collision $St_{im} = (1/9)(\rho_s d_p V_{im}/\eta)$, where V_{im} is the impact velocity [105]. Particularly, as shown by Ten Cate et al. [106], when St_{im} is small, the sphere settles on the surface gently without bouncing back. The bounce starts and the restitution coefficient increases as St_{im} increases above 10, and it approaches the dry value as St_{im} increases even further above 400 [107]. Herein we set up DEM-LBM simulations corresponding to the experiments in which $St_{im} = 0.19$ and $St_{im} = 65$, representing the settling and moderate bouncing regimes respectively. The sphere is initially stationary and then released to descend under gravity before impacting the bottom wall. The material properties are listed in Table 3.2.

In Figure 3-3 (a), the sphere is slightly denser than the surrounding viscous fluid and settles gently at the bottom. The match of the terminal velocity (slopes of the trajectories, within 5% relative error) which is reached long before landing, suggests that the linear momentum exchange between fluid and solid is correct. The veloc-

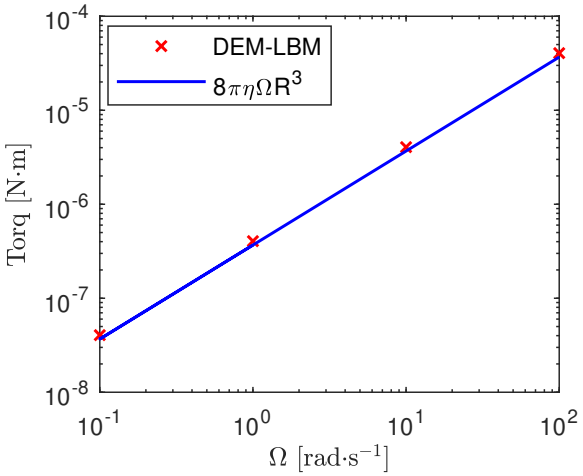

Figure 3-4: Fluid torque exerted on a rotating sphere over a large span of rotational velocity.

ity of the simulated sphere decreases slowly when it is approaching the bottom in agreement with the experiment, showing the hydrodynamic lubrication force is resolved correctly when solid boundaries are getting close. In Figure 3-3 (b), the sphere bounces multiple times and the simulation can match the first three collisions. Capturing the above two impact problems shows the DEM-LBM algorithm is capable of simulating the immersed particle interaction problems accurately, no matter whether they are moving fast or slowly relative the the others.

Besides the linear momentum exchange, we also need to examine how accurate the angular momentum is resolved because torque transfer can be evident due to the shear flow near the bed surface in sediment transport problems. Simulations in which an immersed single sphere is rotating at a fixed position are tested with the rotational velocity Ω varied by 1000 times. The fluid torque experienced by the sphere is compared with the analytical solution of the Stoke's flow solution $T = 8\pi\eta\Omega R_p^3$ as shown in Figure 3-4. The relative error for all the tested rotational speeds is always smaller than 11%.

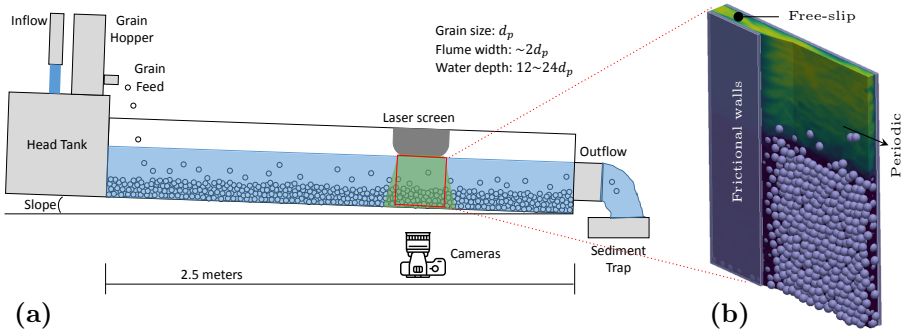

Figure 3-5: Setup of the sediment transport tests in the narrow flume. (a) Experimental setup [73, 72]. (b) The simulated domain corresponds to the videoed zone in the experiment as shown in the red box.

3.2.3 Comparison with laboratory flume experiments

Deal et al. [72] and Benavides et al. [73] conducted bedload sediment transport experiments with glass spheres in a narrow flume, and recorded high-speed videos of the grains, allowing for precise tracking. This provides abundant details of the particle motion. We performed corresponding DEM-LBM simulations as validation specifically to test the accuracy of our method in sediment transport problems. We begin by comparing the time-averaged sediment transport rates as a first verification of our simulations, and then do a more detailed comparison of the time-averaged velocity profiles and particle velocity fluctuation profiles.

The schematic diagram of the flume experimental setup of Deal et al. [72] and Benavides et al. [73] is shown in Figure 3-5 (a). In each experiment, mono-disperse glass spheres and water are fed into the inclined flume from the upstream end at a given combination of volume flux rates. After the initial period of sphere deposition, the granular bed builds up and steady state is reached. Then the slope of the free water surface S as well as the water depth are measured, and the particle motion is recorded by the high-speed cameras in the middle section of the flume. The flume is 10.2mm, slightly wider than two particle diameters ($d_p = 4.95$mm). The density of the spheres is $\rho_s = 2550\,\mathrm{kg/m^3}$. The elastic constants for the normal and tangential contacts are set to be $20\,000\,\mathrm{N\,m^{-1}}$ and $5714\,\mathrm{N\,m^{-1}}$, respectively, guaranteeing the spheres are in hard limit. The friction coefficients of sphere-sphere and sphere-sidewall

contacts are measured to be 0.50 and 0.45 respectively. The dry restitution coefficient of the particles is 0.93. The sensitivity of the results to the choice of the particle surface parameters is low.

DEM-LBM simulations are set up with the same flume geometry and material properties. The simulated domain, as shown in 3-5 (b), has a length $L = 24d_p$ and height $30d_p$. When all the spheres are deposited (in total 969 particles), the thickness of the bed is $18d_p$. The thickness of the bed reduces to $15d_p$ for the largest Shields number tested, as some of the spheres are entrained by the fluid. The LBM lattice has homogeneous grid size $dx = 0.5$mm. The first and last nodes across the flume align with the side walls, and the simulated flume width is adjusted slightly to have $W = 10.5$mm. The top of the simulated domain uses a free-slip (zero gradient) boundary condition. Note that in this narrow flume configuration, the fluid velocity far above the granular bed surface approaches a constant value due to sidewall shear. The bottom uses a no-slip boundary condition and the two sides perpendicular to the flow direction use periodic boundary conditions. For the two side walls of the flume, since the thickness of the boundary layer is smaller than the grid size dx, no-slip boundary conditions with LES is not enough to resolve the near-wall flow field correctly. Instead, we developed a new boundary technique: assuming the second layer of nodes from the wall are out of the boundary layer, we extrapolate the law-of-the-wall flow relationship to the wall, and treat this value as a slip velocity at the wall, which we implement in DEM-LBM using Navier-type boundary conditions used in other studies [108, 109, see Appendix A for more details]. The gravity $g = 9.8\,\mathrm{m/s^2}$ is applied at an angle of slope S with respect to the vertical axis of the simulated domain. The flow is driven by the tilted “horizontal" gravity component.

For the calculation of τ^*, the bed shear stress τ_b is calculated as $\tau_b = \rho_f g S \frac{HW}{2H+W}$, where H is the water depth measured down to the bed surface and W is the flume width. Mindful of the lengthy compute times for each simulation, we chose to perform simulations at 5 different slopes, corresponding to $\tau^* = 0.023$, 0.028, 0.047, 0.063 and 0.068, which covers the experimental range. For the calculation of q^*, the sediment volume flux per unit width q_s is counted in the whole domain as $q_s = \Sigma_i \frac{\pi}{6} d_p^3 V_{i,x}/LW$,

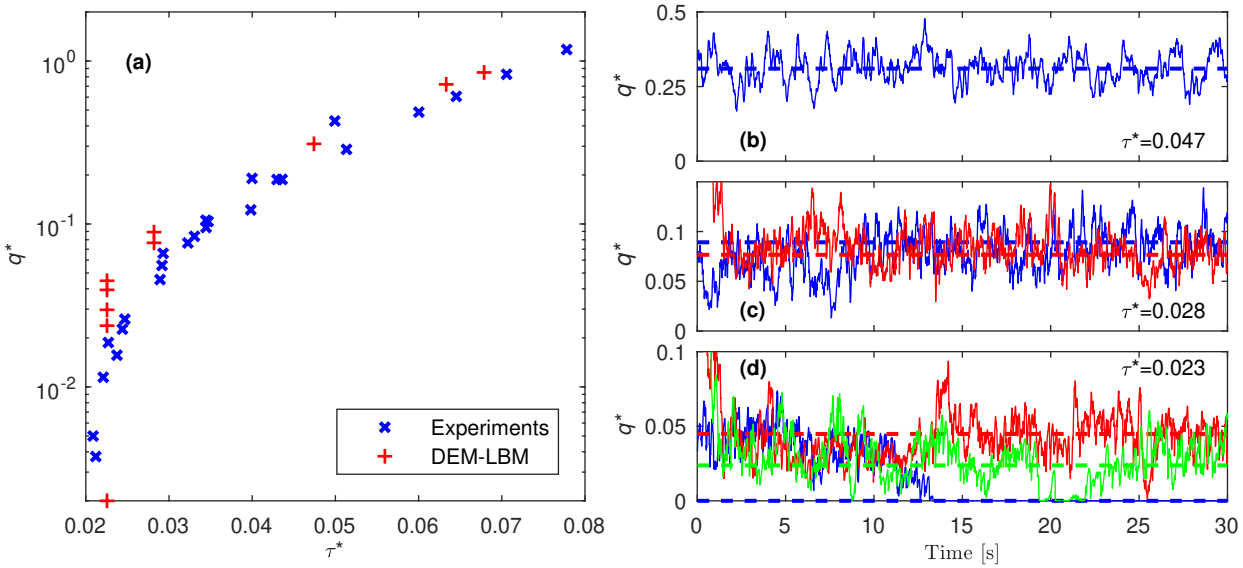

Figure 3-6: Dimensionless sediment transport rate q^* from DEM-LBM simulations. (a) Comparison with the q^* vs τ^* relation from experiments. The critical Shields number in the flume experiments is found to be 0.026 ± 0.002 [73]. At the lowest Shields number $\tau^* = 0.023$, the results show strong intermittency near τ_c^*. The standard initialization gives $q^* = 0$ (shown as 0.002 on the log scale), while the other four cases initialized with the steady flow fields of higher τ^* give different q^* values. Time series of q^* at (b) $\tau^* = 0.047$ (movie08 [46]), (c) $\tau^* = 0.028$ (movie06 and 07 [46]) and (d) $\tau^* = 0.023$ (showing 3 out of the 5 initializations, movie01, 02 and 05 [46]) are shown in thin curves. The thick dashed lines show the mean of the last 10s. The colors distinguish the initializations: blue–standard, red & green–steady flow of $\tau^* = 0.068$ and $\tau^* = 0.063$ respectively.

where $V_{i,x}$ is the streamwise velocity of the i-th particle and L is the length of the simulated domain. The resulting transport relation compared with the experimental results is shown in Figure 3-6(a). The standard initial condition sets the particles uniformly distributed in the whole domain with no velocity and stationary fluid. As each simulation runs, gravity drives the fluid and grains, resulting in the ultimate formation of a particle sediment bed and a transverse fluid flow profile, which transports the near surface particles. For the low Shields numbers, besides the standard initial condition just described, we also run tests where the initial particle positions and initial particle and fluid velocity are assigned from a snapshot taken at the end-phase of a higher Shields number simulation. The simulations are all carried out for at least 30s of simulation time and the last 10s of the simulations are taken to calculate the time averaged values and standard deviation of the integrated flux. The Rouse number ranges from 11.4 to 20.9, indicating the sediment transport is in the bedload regime.

Overall, in terms of the q^* vs τ^* transport relation, the DEM-LBM simulations are consistent with the experiments. At the lowest Shields number simulated, $\tau^* = 0.023$ (τ_c^* found to be 0.026 ± 0.002 [73]), we observe strong intermittency (see movie01 [46]). With the standard initialization, the transport of particles eventually ceases, giving $q^* = 0$ (marked as 0.002 in Figure 3-6(a) due to semi-log). The additional data shown at this slope correspond to simulations using different initializations as described in the prior paragraph. Each of these tests produced low transport rates at steady state, seemingly not correlated to the flow rate of the initialization. Time series data of the transport rate for different initializations are shown in Figure 3-6(d). With the current sampling duration, the standard deviation of q^* at $\tau^* = 0.023$ is on the same order of magnitude as the time averaged q^*. The fact that the variation of the sampled q^* is inversely proportional to the sampling duration [110] implies that reducing the relative uncertainty to 15% of the mean q^* at this lowest transport stage may require the simulations to be run for an additional 200s, which would be too costly for us to run. The intermittency observed could arise from internal variability or potentially from the existence of multiple attractors allowing flowing and non-flowing

steady solutions to coexist at low slopes. At the second lowest simulated transport stage, $\tau^* = 0.028$, the intermittency is less obvious and the transport is continuous as shown in 3-6(c). The standard initialization (movie06 [46]) gives $q^* = 0.089$ with standard deviation 0.019 while the case with the fastest initialization (movie07 [46]) gives $q^* = 0.077$ with standard deviation 0.017. As τ^* increases further from the critical Shields number, the relative uncertainty of the measured q^* goes down to 16% at $\tau^* = 0.047$ (see 3-6(b)), 11% at $\tau^* = 0.063$ and 9% at $\tau^* = 0.068$.

One may notice that transport is observed for very low τ^* values. On one hand, we use the hydraulic radius to estimate the bed shear stress which tends to underestimate the value [111]. On the other hand, a similar low threshold for sediment transport is also observed in a related experimental setup [112] and it has been shown to not be a result of the sidewall influence on turbulence [113]. Also as seen in the movies (Movie01 to Movie05 [46]) of the simulations, the behavior of the particles at the lowest τ^* values seems to correspond to the Intermittent Bulk Transport regime [68] in which τ^* is above the rebound threshold but below the impact entrainment threshold, and the transported particles rebound for a relatively long period on the bed surface before depositing. Due to the periodic boundary conditions applied in the streamwise direction, the simulations have a larger auto-correlation. As a result, the simulations might overpredict q^* when particles are bounding on the bed surface.

Despite the limitation at the low Shields number, the simulations still provide microscopic details when a particle is solely entrained by the turbulent flow. In the intermittent flows shown in Figure 3-6(d), the green curve (corresponding to movie05 [46]) indicates that the sediment transport comes to a full stop at around 20s and then resumes at 21s when a particle on the bed surface is entrained (rolling) by the turbulent fluid. As shown in Figure 3-7(a,b,c), the entrained particle P0 is sitting stationary on the bed surface, in contact with particle P1, P2, P3 and the side wall of the flume before 21s. Under the influence of a turbulent burst, P0 rolls over P1 and P2, losing contact with P3 and the wall.

Using DEM-LBM's capability of resolving fluid-grain traction, we now detail the processes taking place during this prototypical near-threshold entrainment event. The

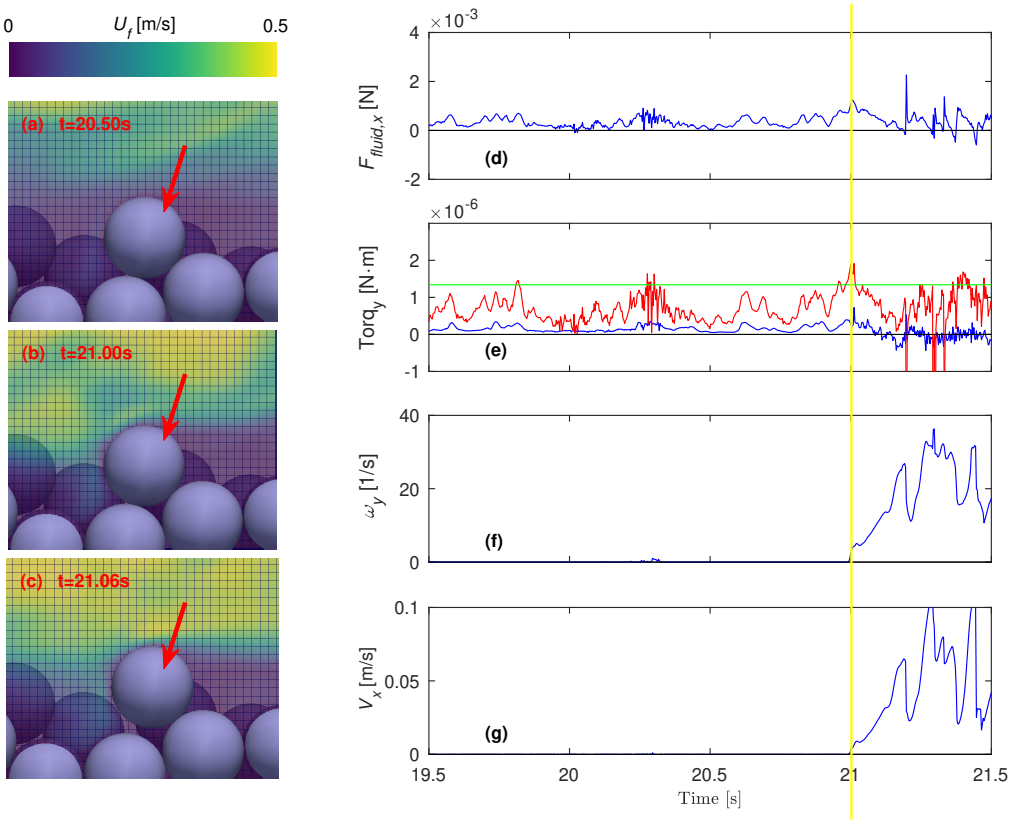

Figure 3-7: Examination of a near-threshold entrainment event (see movie05 [46]). (a) $t = 20.50s$, particle P0 (highlighted with red arrow) in contact with neighbors P1, P2 and P3 and the side wall. (b) $t = 21.00s$, the start of the entrainment of P0. (c) $t = 21.06s$, particle P0 gets entrained by the fluid, rolling over P1 and P2, and loses contact with P3 and the wall. Each contour shows the fluid velocity field on the plane going through the center of P0. The fluid traction over the particle surface can be treated equivalently as a single force and pure moment (couple) acting at the center of the particle. The detailed information about particle P0 around the entrainment event is displayed: (d) hydrodynamic force in the downstream direction, (e) fluid torque (blue: fluid couple, red: fluid couple + net hydrodynamic force induced torque), with respect to the hinge connecting the contact points of (P0, P1) and (P0, P2), compared with the critical torque (green) estimated by product of the lever arm and
the submerged weight of P0, (f) rotational velocity (axis into the paper) and (g) downstream velocity.

fluid traction over the particle surface can be treated equivalently as a single force and pure moment (couple) acting at the center of P0. Figure 3-7(d) shows the hydrodynamic force in the downstream direction. Figure 3-7(e) shows the fluid torque (into the paper component) with respect to the hinge connecting the contact points of (P0, P1) and (P0, P2). The torque is evaluated as the integration of the cross products of the lever arm vector and the hydrodynamic force vector along the surface of the particle. For reference, the green line shows the "critical" fluid torque to maintain the particle free of contact with P3 and the side wall, estimated by the product of the lever arm and the submerged weight. According to Figure 3-7(f,g), when the fluid torque exceeds the critical value near 20.3s, P0 wiggles but still falls back. The entrainment happens at 21s when the fluid torque goes above the critical value and lasts long enough to transfer enough angular momentum to roll P0 out of the spot, which may correspond to an angular momentum criterion similar to the impulse criterion in literature [114]. The fluid torque comes from the fluid traction on the surface of P0, which is equivalent to a net hydrodynamic force on the center of P0 plus a fluid couple. The blue curve in Figure 3-7(e) shows the contribution of the fluid couple, which is about 1/4 of the total fluid torque (shown in red). Equivalently, the fluid traction can be simplified solely as a net force acting on the point $d_p/6$ away from the center on the far side from the hinge. The non-negligible role of the fluid couple shows that fluid-particle angular momentum transfer plays a role in the entrainment. Thus, combined fluid-DEM simulation methods that utilize only a fluid-particle drag force may be missing some relevant physics, at least at the low Shields regime. Other particles examined on the bed surface have also shown a similar $\sim 1/4$ contribution on the total fluid torque from the net fluid couple. More quantitative examinations can be found in the next subsection. Besides the entrainment events purely initiated by the turbulent fluid flow, there are also ones initiated by collisions with hopping particles. Simulations in Vowinckel et al. [115] have shown that a subsequent sweep event that is strong enough is needed for the collided particle to be entrained. Similar results are also seen in our simulations: the fluid torque needs to exceed a certain critical value to get the particle out of its local pocket after the collision.

Next, we examine the flow profiles of the particles. To get the flow fields as functions of the height z with respect to the bed surface, we need to homogenize the flow fields along the flow direction and then average the profiles over time. The homogenization is carried out in three steps. The first step is to identify the particles to be used in the homogenization. In the experiments, since the motion of the particles are recorded by a camera from one side of the flume, which is slightly wider than $2d_p$, only one layer of the particles can be recognized in the images. In the post-processing of the simulations, the particles are projected onto a 2D plane which is discretized into square pixels of $d_p/25$ to mimic the images taken in the experiments. In an effort to match the experimental post-processing method, if more than 60% of the length of the perimeter is covered by particles in front of it, that particle will be labeled as invisible. For the particles left, if two projected particles are closer than $d_p/6$, only the front one is visible. The particles labeled as visible will be used in the next steps of homogenization. In the experiments, due to the refraction, the edges of the particles in the back may confuse the particle recognition in experiment images in rare cases. The resultant areal fractions can therefore be slightly different. For the bed surface, any pixel that is occupied by a particle for half a second is marked as static and then the position of the bed surface can be decided as the outline of the static pixels, as the thick black curves show in Figure 3-8. The vertical position z of a particle is defined as the vertical distance between the center of the particle and the bed surface. The second step is to calculate the areal fraction and particle mean velocity as functions of z. The areal fraction profile is calculated as the packing fraction of the particles labeled as visible. The velocity homogenization is obtained from the linear momentum of the layer at z. The third step is to calculate the granular temperature based on the particle-wise velocity deviation in each snapshots. More details about the last two steps of the homogenization can be found in Zhang and Kamrin [32]. The images of the particles in experiments are post-processed in the same way after the particles are recognized. The fluid velocity field is also averaged temporally and spatially using a similar method to the solid velocity homogenization, based on the linear momentum of a layer of nodes at a given z.

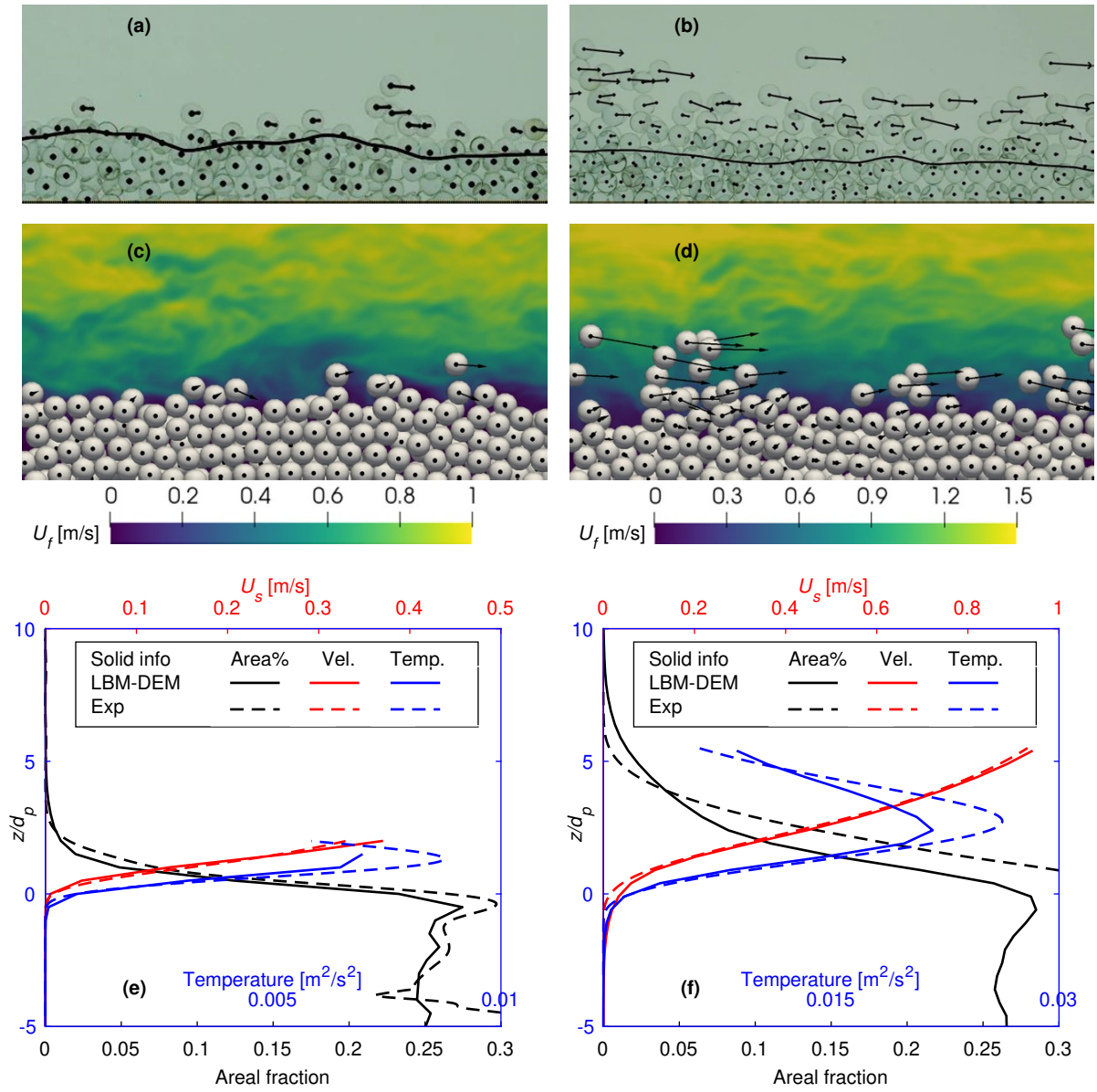

Figure 3-8: Comparisons between the flume experiments and DEM-LBM simulations at Shields number $\tau^* = 0.028$ (left column), and $\tau^* = 0.068$ (right column). (a) & (b) Snapshots of the flume experiments, particle in-plane velocity represented by the arrows. The black curves represent the bed surface. (c) & (d) Snapshots of the DEM-LBM simulations, particle in-plane velocity represented by the arrows, fluid field colored by the fluid velocity magnitude on the center-plane of the flume. (e) & (f) Experiments vs DEM-LBM simulations comparison in terms of the solid phase profiles as a function of the height from bed surface: areal fraction, particle velocity and granular temperature.

The simulated and experimental flow profiles are very similar at a medium Shields number $\tau^* = 0.028$ and a high Shields number $\tau^* = 0.068$, as shown in Figure 3-8. The bed structures and the motion of the particles look similar at both Shields numbers (see movie06 and movie10 [46]). The velocity profiles match the experiments and even the granular temperature, which is a higher order variable; granular temperature may be key to understanding sub-surface granular creep [32, 116]. The areal fraction profiles differ slightly, but are still similar to the experiment results. One reason may be that the particle recognition technique used in the experiments is not easy to replicate in the simulation post-processing, e.g., due to the refraction effects. Fortunately as long as enough particles are sampled for a given height, this difference theoretically does not change the averaged particle velocity or granular temperature; see Figure 3-8 (e) & (f). With the results described above, the simulations are deemed to provide a useful description of observed sediment transport processes, and we proceed to perform numerical experiments to study sediment transport problems from bulk to grain-scale.

3.2.4 Wide wall-free cases

We conduct a parameter study using the simulations to see what properties affect the transport rate. Namely, how much do certain details about the grains, such as particle surface friction and damping coefficient, matter versus geometric properties such as fluid depth, slope and average grain size? Wide wall-free (WWF) simulations (inspired by wide rivers, without the physical side walls like in the flumes), as shown in Figure 3-9(a), are a simple and useful geometry to use toward this end. The wide wall-free simulations also produce 1D solution fields and serve as benchmark cases to test the continuum modeling in Section 3.3.

What are the independent variables that can influence the transport rate in sediment transport problems? Putting the grain shape and size distribution aside, the variables are the gravity g, fluid density ρ_f, fluid viscosity η, slope S, water depth H, particle density ρ_s, particle diameter d_p, particle surface friction coefficient μ_p, particle damping coefficient g_p and particle stiffness k_p, which means the sediment

Table 3.3: Non-dimensionalization of the dependent and independent variables in sediment transport problems (Var: variables, Dim: dimensions, DN: dimensionless numbers)

Var	q_s	H	S	ρ_f	η	g	ρ_s	d_p	μ_p	g_p	k_p
Dim	$\frac{\mathrm{L}^2}{\mathrm{T}}$	L	-	$\frac{\mathrm{M}}{\mathrm{L}^3}$	$\frac{\mathrm{M}}{\mathrm{LT}}$	$\frac{\mathrm{L}}{\mathrm{T}^2}$	$\frac{\mathrm{M}}{\mathrm{L}^3}$	L	-	$\frac{\mathrm{M}}{\mathrm{T}}$	$\frac{\mathrm{M}}{\mathrm{T}^2}$
DN	$q_s\frac{\rho_f}{\eta}$	$H\big(\frac{\rho_f^2 g}{\eta^2}\big)^{\frac{1}{3}}$	S	1	1	1	$\frac{\rho_s}{\rho_f}$	$d_p\big(\frac{\rho_f^2 g}{\eta^2}\big)^{\frac{1}{3}}$	μ_p	$\frac{g_p}{\eta}\big(\frac{g\rho_f^2}{\eta^2}\big)^{\frac{1}{3}}$	$\frac{k_p}{\eta}\big(\frac{\rho_f}{\eta g}\big)^{\frac{1}{3}}$
Symbol	Π_0	Π_1	Π_2	-	-	-	Π_3	Π_4	Π_5	Π_6	Π_7

transport rate q_s can be estimated by a ten-input function Ψ_0 as shown below:

$$q_s = \Psi_0\big(H, S, \rho_f, \eta, g, \rho_s, d_p, \mu_p, g_p, k_p\big). \tag{3.8}$$

The dependent (1) and independent (10) variables in Eq 3.8 can be non-dimensionalized by ρ_f, η and g using the below relations:

$$[\mathrm{M}] = \frac{\eta^2}{\rho_f g}, \quad [\mathrm{L}] = \left(\frac{\eta^2}{\rho_f^2 g}\right)^{1/3}, \quad [\mathrm{T}] = \left(\frac{\eta}{\rho_f g^2}\right)^{1/3}. \tag{3.9}$$

Since there are three dimensions involved in these 11 variables, the variables can be nondimensionlized into 8 dimensionless groups, as shown in Table 3.3, and the transport relation can be expressed as:

$$\Pi_0 = \Psi_1\big(\Pi_1, \Pi_2, \Pi_3, \Pi_4, \Pi_5, \Pi_6, \Pi_7\big). \tag{3.10}$$

We are free to operate on these dimensionless groups so that some of them become existing widely used dimensionless numbers: Π_0 can be modified into the Einstein number $q^* = \frac{\Pi_0}{\Pi_4^{3/2}(\Pi_3-1)^{1/2}}$, Π_1 into the Shields number $\tau^* = \frac{\Pi_1\Pi_2}{\Pi_4(\Pi_3-1)}$, and Π_4 into the Galileo number $Ga = \frac{\sqrt{gd_p^3}}{\eta/\rho_f} = \Pi_4^{3/2}$. Also, since $\Pi_2 = S$, $\Pi_3 = \frac{\rho_s}{\rho_f}$ and $\Pi_5 = \mu_p$ are simple enough, we just use the original variables:

$$q^* = \Psi_2\big(\tau^*, S, \frac{\rho_s}{\rho_f}, Ga, \mu_p, \Pi_6, \Pi_7\big). \tag{3.11}$$

For sediment transport on Earth's surface, ρ_f and η are given as the values for

water and $g = 9.81\text{m/s}^2$. We limit our discussion to the transport of silica-based media like sand (ρ_s/ρ_f is fixed). For river bed sediment transport problems, the sand particles are in the hard limit (the particle deformation is negligible), which means $\Pi_7 \to \infty$, and thus it does not influence the transport rate. Then we have reduced the input set to five variables:

$$q^* = \tilde{\Psi}\big(\tau^*; S, Ga, \mu_p, \Pi_6\big). \tag{3.12}$$

Considering the empirical transport relation q^* vs τ^*, q^* can be seen as a function of τ^* parameterized by S, Ga, μ_p and Π_6 (dimensionless particle damping coefficient).

Besides the dimensionless groups above, previous researchers consider dimensionless numbers that are not included in Table 3.3. Here we comment on how these numbers are related to our dimensionless groups or why some of them are not included in this study. One dimensionless group commonly found in literature is the settling Reynolds number [55] $Re_s = \frac{\rho_f w_s d_p}{\eta}$ with the characteristic settling velocity $w_s = \sqrt{g d_p (\rho_s - \rho_f)/\rho_f}$, which can be written as $Re_s = Ga\sqrt{\Pi_3 - 1}$. The particle Reynolds number [55] can be written as $Re_p = \frac{\rho_f \sqrt{\tau_b/\rho_f}\, d_p}{\eta} = Ga\sqrt{(\Pi_3 - 1)\tau^*}$. The Rouse number [117] can be written as $Ro = \frac{w_s}{\kappa\sqrt{\tau_b/\rho_f}} = \frac{1}{\kappa\sqrt{\tau^*}}$, where $\kappa = 0.41$ is the Von Kármán constant. Some papers [118, 119] also use the dimensionless saltation length and saltation height, but these are actually outputs in our study and as such arise from the choice of input parameters above. Wong and Parker [84] use the dimensionless Chezy resistance coefficient to account for the influence of the channel sidewalls, which is not necessary in this dimensional analysis for the case of wide rivers.

A new set of DEM-LBM simulations are performed without sidewalls to study the influence of the five dimensionless numbers on the sediment transport relation. The geometry of the simulated domain is shown in Figure 3-9(a), compared with the classical 3/2 power law. The granular bed is $24d_p$ long and $8d_p$ wide. The height of the granular bed when all the particles have settled is $10d_p$ (in total 2884 particles). The domain height is set according to the water depth H. Periodic boundary conditions

Table 3.4: Parameters of the wide wall-free simulations. (The base parameters are red.)

Group	S	d_p(mm)	Ga	μ_p	g_p(m/s)	Π_6
WWF1	0.016	5	1378	0.5	0.09	4.2E3
WWF2	0.010	5	1378	0.5	0.09	4.2E3
WWF3	0.030	5	1378	0.5	0.09	4.2E3
WWF4	0.016	8	2789	0.5	0.09	4.2E3
WWF5	0.016	5	1378	0.1	0.09	4.2E3
WWF6	0.016	5	1378	0.5	2.11	9.8E4

are adopted at the four side boundaries. For fluid, the top boundary is a free slip boundary condition whereas the bottom is a no-slip boundary condition. The gravity is tilted by a slope S. The domain is still discretized with the grid size $dx = 0.5$mm for LBM. Simulations are performed at gentle slopes $S = 0.010, 0.016, 0.030$ with monodisperse particles whose density is $\rho_s = 2550\,\mathrm{kg/m^3}$. The simulations are in the bedload transport regime, with Rouse number $\sim 17.4 - 30.0$. Corresponding to the dimensionless groups, the simulation parameters are designed to vary the dimensionless numbers one by one (as shown in Table 3.4) so that we can identify their influence on the q^* vs τ^* relation. The bed shear stress in this geometry can be calculated as $\tau_b = \rho_f g H S$. Water depth H is varied to set the Shields number τ^* to values ranging from 0.046 to 0.141. Each simulation is performed for 30s and the results of the last 10s are averaged, as shown in Figure 3-9. The averaged solid phase shear stress matches the equilibrium solution, suggesting the steady state has been reached. WWF1 is the reference group using the exact same particles as the flume tests. WWF2 and WWF3 change the macroscopic geometrical parameter S. WWF4, WWF5 and WWF6 vary the microscopic particle parameters: particle size d_p (corresponding to Ga), μ_p, and the damping coefficient g_p (corresponding to Π_6). The value in WWF6 $g_p = 2.11$ m/s corresponds to a dry restitution coefficient of e =0.10 while $g_p = 0.09$ m/s in the other groups corresponds to e =0.93. The integrated transport relation $q^* - \tau^*$ at steady state is shown in Figure 3-9(b) and (c).

The results of the DEM-LBM simulations from WWF1, WWF2 and WWF3 with different S overlap on top of each other, indicating S has little influence on the di-

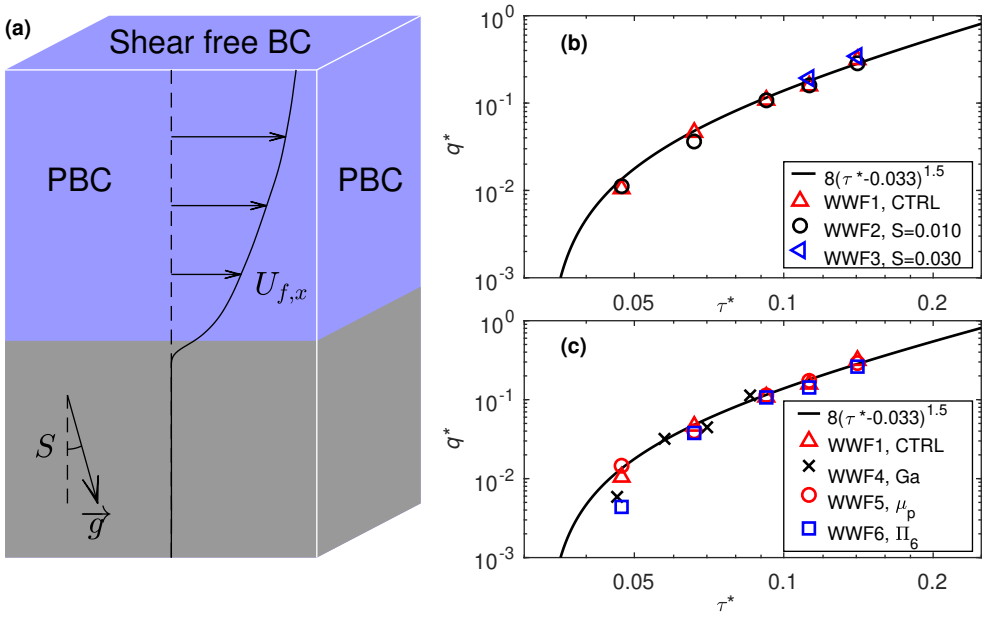

Figure 3-9: (a) Geometry and boundary conditions of the wide wall-free (WWF) simulations (PBC: periodic boundary condition). The simulated domain size is $24d_p \times 8d_p \times \sim 20d_p$. (b) Sediment transport relation from the wide wall-free simulations with the macroscopic geometrical parameter S varied. (c) Sediment transport relation from the wide wall-free simulations with the microscopic particle parameters Ga, μ_p and Π_6 varied. WWF1 is the control group while the other groups vary the dimensionless groups in Table 3.4 one by one, as denoted in the legends. The black curve is $q^* = (\tau^* - 0.033)^{1.5}$.

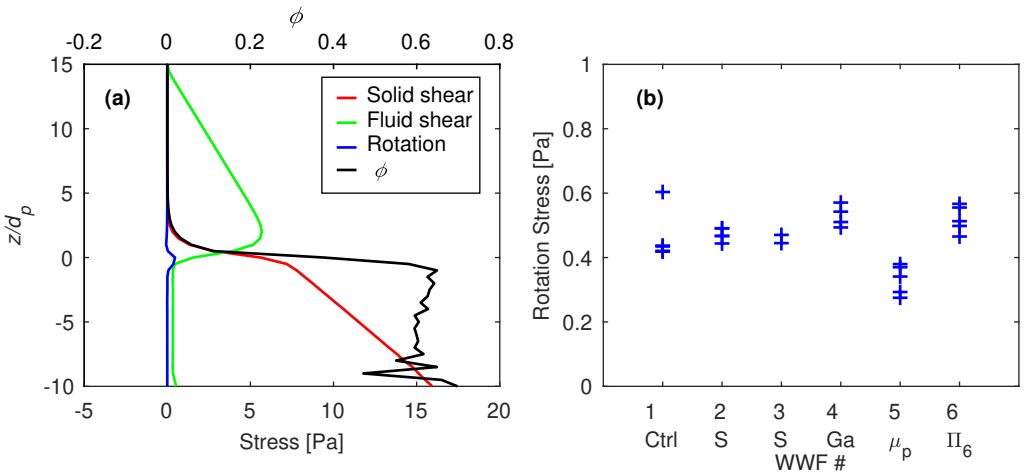

Figure 3-10: Examination of the rotation stress in wide wall free cases. (a) Flow profiles (WWF2 at $\tau^* = 0.085$) as a function of the height above the bed surface: solid shear stress, fluid shear stress, rotation stress and packing fraction. (b) The maximum rotation stress in different wide wall free groups.

mensionless sediment transport rate on gentle slopes (when τ^* is fixed) and is likely not responsible for the variation in flux (q^*) for a given Shields number (τ^*) in experiments [8]. The data sets with varied Ga, μ_p and Π_6 also appear very much the same as the transport relation of WWF1 as shown in Figure 3-9(c), except for some discrepancy at the smallest Shields number tested $\tau^* = 0.0471$ near the threshold: smaller μ_p gives slightly larger q^* whereas larger Ga, and Π_6 give smaller q^*.

3.2.5 Fluid-grain torque interactions

We can also further examine the fluid-solid angular momentum transfer in the wide wall free cases. The net fluid couple (when the origin is picked at the center of the particle) exerted on the ith particle is $\boldsymbol{T}_i = \oint_{A_i} r\hat{\boldsymbol{r}} \times (\boldsymbol{\sigma}_f \cdot \hat{\boldsymbol{r}}) dA$, where A_i is the surface area of the particle, $r = d_p/2$ is the radius, $\hat{\boldsymbol{r}}$ is the unit normal vector pointing out, and $\boldsymbol{\sigma}_f$ is the fluid stress tensor. Following Signorini's theorem [120], the traction distribution over a particle's surface creates the average stress tensor within, and thus the fluid traction has a contribution to the solid phase stress tensor on the ith

particle:

$$\boldsymbol{\sigma}^f_{s,i} = \frac{3}{4\pi r^3} \oint_{A_i} (\boldsymbol{\sigma}_f \cdot \hat{\boldsymbol{r}}) \otimes r\hat{\boldsymbol{r}} dA. \tag{3.13}$$

While the stress tensor is generally a symmetric quantity, its various contributions may not be even if the total stress still is. Here, $\boldsymbol{T}_i$ is related to the skew part of $\boldsymbol{\sigma}^f_{s,i}$ In this study, we are most interested in the y component (into the paper) of the torque: $\sigma^f_{s,i,xz} - \sigma^f_{s,i,zx} = 3T_{i,y}/4\pi r^3$. We call $\sigma^f_{s,i,xz} - \sigma^f_{s,i,zx}$ the "rotation stress" and calculate the homogenized profile as a function of z, as shown in Figure 3-10(a), compared with the solid total stress, fluid stress and the packing fraction ϕ. The maximum value of the rotation stress occurs at the bed surface (as defined in Pähtz and Durán [68]), corresponding to the intuition that the exposed particles on the sediment bed surface sustain the largest fluid torque with the "help" (resistance) of the bed particles. So the rotation stress is not only a measure of the fluid torque exerted on the particles, but also an indicator of the resistive torque provided by the neighbour particles, which balance each other on average at steady state. The maximum rotation stress in the shown case is 0.47Pa, much smaller than the solid shear stress (5.62Pa) at the same position.

Figure 3-10(b) shows the maximum value of each rotation stress profile across different wide wall free simulation groups. Each data point comes from the profile of simulation with a unique set of physical parameters. The values from WWF1, WWF2 and WWF3 are close to each other, suggesting the slope has minor influence on the maximum rotation stress. The maximum rotation stress values of WWF4 and WWF6 are slightly higher than those in WWF1, WWF2 and WWF3, while the values of WWF5 are lower. Looking back at Figure 3-9(c) at the smallest Shields number $\tau^* = 0.0471$, the q^* values from different groups are inversely correlated to the corresponding maximum rotation stress in Figure 3-10(b) — WWF5 has the smallest rotation stress corresponding to the largest q^* while WW4 and WWF6 have larger rotation stress corresponding to smaller q^* values. Also considering that the values seem not to be correlated to the Shields number over the tested range $0.0471 \sim 0.1408$

and mostly a constant in each group, it indicates the torque resistance of the bed is like a material property of the particles. While the maximum rotation stress can be seen as a measurement of the bed resistance, on the other hand it is a driving factor for the particle motion. For the particles on the sediment bed surface, there are two driving factors countering the resistance from the neighbor particles in contact: collision with moving particles and fluid interactions (fluid net couples and hydrodynamic forces as illustrated by Figure 3-7). Since the maximum rotation stress is almost a constant in the tested Shields number range whereas the hydrodynamic force is correlated to τ^*, the influence of the maximum rotation stress of the material on q^* is most evident near the threshold. The maximum rotation stress of WWF5 is slightly below the control group because the low surface friction coefficient reduces the amount that particle contacts can resist the couple. In WWF6, the collisions of the particles on the bed surface dissipates more energy, which in return increases the resistance, giving rise to higher rotation stress.

3.3 Continuum modeling

While the DEM-LBM simulations in the last section are useful for gaining understanding, the drawback from a modeling perspective is obvious: resolving individual grains and running the LBM with a resolution of one tenth of a particle diameter makes for a method that is computationally expensive. For example, a half-minute long wide wall free simulation can take more than a week. These simulations are only affordable for small scale problems or rheological studies. For large scale problems, continuum models with proper closures can be applied for reasonable computational cost.

DEM-LBM simulations do, however, provide a prime tool for developing and extracting continuum models, offering certain advantages over experiments alone. Some of the desired experiments would be difficult to conduct in the lab setting and some of the quantities that are important in developing the continuum model are not easily accessible from experiments, such as the bulk fields of stress and velocity in the fluid

and granular phase, as well as granular temperature.

In this section, we present a two-phase continuum model for steady-state behavior based on a recent mixture theory framework, turbulent-particle interaction closures, and known granular rheology principles. It is validated/calibrated directly from our DEM-LBM simulations. Close comparisons are made between the results from DEM-LBM simulations and the proposed continuum model in terms of the sediment transport relation and the detailed flow profiles of both fluid and solid phases. Besides the relatively fast motion of the transported particles and the fluid, the last subsection will also discuss the modeling of creep beneath the bed surface.

3.3.1 Method

A promising approach for continuum modeling of fluid-grain mixtures is to use a two-phase mixture theory [121, 122, 123, 7] that contains mass and momentum balances for both fluid and solid phases, and three closures: constitutive relations for fluid and solid phase stresses and a drag-law that transfers momentum between solid and fluid phases. As mentioned at the beginning, since the granular flow in sediment transport problems covers multiple regimes, the granular constitutive relation is crucial to making accurate predictions.

The framework of the continuum model presented here is based on a recent mixture model which spans dilute to dense regimes [7], with the addition of a turbulent closure as well as an enhanced drag law and granular rheology. The solid and fluid phases of the fully immersed mixture are considered as overlapping continuum bodies with volume fractions ϕ and porosity $n = 1 - \phi$ respectively. The Cauchy stress tensor of the mixture is defined as the sum of the phase-wise Cauchy stresses: $\boldsymbol{\sigma} = \boldsymbol{\sigma}_s + \boldsymbol{\sigma}_f$. The fluid and solid phase-wise Cauchy stress can be expressed as

$$\boldsymbol{\sigma}_f = \quad \boldsymbol{\tau}_f - n\, p_f\, \mathbf{1} \tag{3.14}$$

$$\boldsymbol{\sigma}_s = \quad \tilde{\boldsymbol{\sigma}}\ - \phi\, p_f\, \mathbf{1}, \tag{3.15}$$

where $\boldsymbol{\tau}_f$ is the deviatoric part of $\boldsymbol{\sigma}_f$, $p_f = -\mathrm{tr}(\boldsymbol{\sigma}_f)/3n$ is the fluid pore pressure, and

$\tilde{\boldsymbol{\sigma}}$ is the solid effective stress which drives the granular plastic flow.

The motion of the mixture in steady state is governed by the mass balance equations

$$\boldsymbol{U}_s \cdot \mathrm{grad}(\phi\rho_s) + \phi\,\rho_s\ \mathrm{div}\boldsymbol{U}_s = 0 \tag{3.16}$$

$$\boldsymbol{U}_f \cdot \mathrm{grad}(n\rho_f) + n\,\rho_f\,\mathrm{div}\boldsymbol{U}_f = 0 \tag{3.17}$$

and momentum balance equations

$$\phi\,\rho_s\,\boldsymbol{U}_s \cdot \mathrm{grad}(\boldsymbol{U}_s) = \phi\,\rho_s\,\boldsymbol{g} - \boldsymbol{f}_d + \mathrm{div}\tilde{\boldsymbol{\sigma}} - \phi\,\mathrm{grad}(p_f) \tag{3.18}$$

$$n\,\rho_f\,\boldsymbol{U}_f \cdot \mathrm{grad}(\boldsymbol{U}_f) = n\,\rho_f\,\boldsymbol{g} + \boldsymbol{f}_d + \mathrm{div}\boldsymbol{\tau}_f - n\,\mathrm{grad}(p_f), \tag{3.19}$$

where $\boldsymbol{f}_d$ is the drag force density from the solid phase to the fluid phase. The buoyancy is built in to the grad pressure terms.

Besides the equations of mass and momentum balances, three closures (constitutive laws) are needed to solve the system: granular rheology for $\tilde{\boldsymbol{\sigma}}$, turbulent closure for $\boldsymbol{\tau}_f$ and inter-phase drag law for $\boldsymbol{f}_d$.

Granular flow rule

For the steady flow of submerged granular materials, based on suspension rheological experiments, Boyer et al. [124] proposed a rheology in which the packing fraction ϕ and granular stress ratio $\mu = \bar{\tau}/p_p$ are functions of only the dimensionless viscous number $I_v = \eta\dot{\gamma}/p_p$, where $\dot{\gamma}$ is the solid equivalent shear strain rate, granular pressure $p_p = -\mathrm{tr}(\tilde{\boldsymbol{\sigma}})/3$, and granular shear stress $\bar{\tau}$ is defined as the magnitude of the deviotoric part of $\tilde{\boldsymbol{\sigma}}$. Similarly, in the rheology of dry granular materials, ϕ and μ are solely functions of the inertial number $I = \dot{\gamma}d_p/\sqrt{p_p/\rho_s}$ [5]. Trulsson et al. [125] proposed a combination of I_v and I to unify the rheology based on 2D simulations, which covers both the viscous regime proposed for suspensions and the inertial regime when fluid resistance is minimal. Later, Amarsid et al. [87] modified the combination as the mixed inertial number $I_m = \sqrt{2I_v + I^2}$ and expressed ϕ and μ in terms of I_m.

Recently, inspired by the work of Boyer et al. [124] and Amarsid et al. [87], Baumgarten and Kamrin [7] proposed a granular flow model that unifies dilute suspension rheology, dense suspension rheology, and inertial flow rheology.

Starting from the latter model, we analyze and fit the granular material parameters with additional DEM-LBM tests in simple shear geometries [124] under varied packing fractions. In the simple shear simulations, there is no gravity and the mixture is confined between the top and bottom walls which are made of particles. The bottom wall is fixed whereas the top wall is assigned a constant horizontal shear velocity. All the side boundaries are periodic. The volume fraction of the particles is varied test-by-test from 0.03 to 0.6. The particles are exactly the same as the previous wide wall-free tests and flume tests. Instead of water, a more viscous fluid ($\eta = 0.417\,\mathrm{Pa}\cdot\mathrm{s}$) is used in the simple shear tests to avoid turbulence for now. In post-processing, $\boldsymbol{\sigma}_s$ is homogenized from the stress in each particle, which arises from grain-grain contact forces $\boldsymbol{\sigma}_s^c$, particle velocity fluctuations $\boldsymbol{\sigma}_s^{dv}$ (just like the Reynolds stress in turbulent fluid mechanics) and fluid-solid interaction $\boldsymbol{\sigma}_s^f$. The contributions from contacts and fluctuations can be calculated according to Da Cruz et al. [17]. Since DEM-LBM provides the fluid-grain momentum exchange along the grain surfaces, these can be used to calculate the fluid-force contribution to the particle-wise stress tensor (see Eq 3.13).

Note that the phase-wise total stresses $\boldsymbol{\sigma}_f$ and $\boldsymbol{\sigma}_s$ are still symmetric in steady state even though the part of the solid stress $\boldsymbol{\sigma}_s^f$ arising from the fluid traction on the particle surfaces is asymmetric near the bed surface. For the solid phase stress $\boldsymbol{\sigma}_s$, the contact from neighbor particles is providing resistant torque, which makes the solid stress component $\boldsymbol{\sigma}_s^c$ from the particle contact asymmetric so that $\boldsymbol{\sigma}_s^c + \boldsymbol{\sigma}_s^f$ is still symmetric. So the defined rotation stress ($\boldsymbol{\sigma}_{s,xz}^f - \boldsymbol{\sigma}_{s,zx}^f$ in the wide wall free geometry) is not only one of the hydrodynamic driving factors on its own, but also an indicator of the bed resistant torque since the skew parts of $\boldsymbol{\sigma}_s^c$ and $\boldsymbol{\sigma}_s^f$ get the same magnitude. For the modeling of the stress asymmetry of the fluid traction, a higher order mixture model which utilizes a“micropolar" form [126, 127] may be used, which can be a future research direction. The fluid phase homoegnized stress $\boldsymbol{\sigma}_f$ is

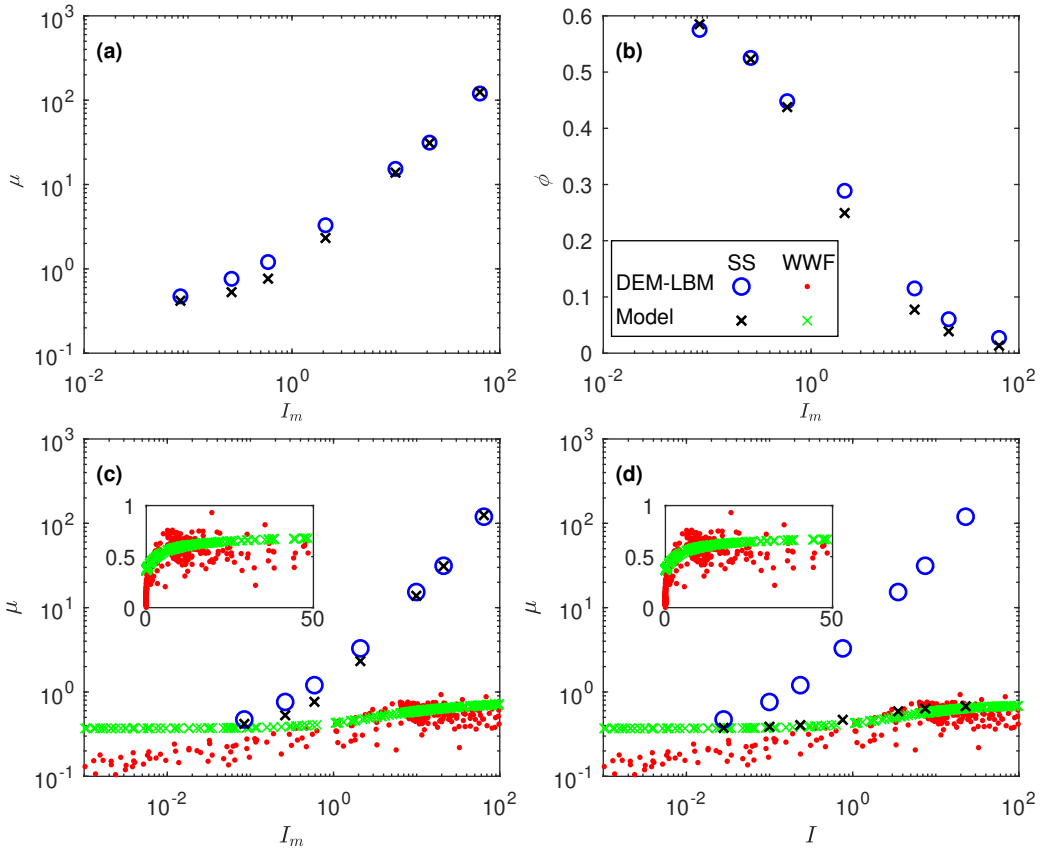

Figure 3-11: Granular flow rule from simple shear SS simulations: (a) the dependence of stress ratio μ on the mixed inertial number I_m, (b) packing fraction ϕ as a function of I_m. Fitted granular flow rule validated with the data from the wide wall free (WWF) simulations: (c) Scatter plot of μ versus I_m , (d) scatter plot of μ and I (dry rheology). Each data point of DEM-LBM comes from a set of homogenized values at a elevation in a WWF test (in total 27 included).

symmetric since it is homogenized from a fluid local stress field that is symmetric.

The DEM-LBM simple shear test results are shown in Figure 3-11, leading to an enhanced granular flow rule as follows:

$$\mu = \mu_1 + \frac{\mu_2 - \mu_1}{1 + b/I_m} + \frac{5}{2}\frac{\phi\, I_v}{a\, I_m} + \frac{5}{2}\phi\, I_v, \tag{3.20}$$

$$\phi = \frac{\phi_m}{1 + a\, I_m}, \tag{3.21}$$

where $a = \sqrt{2}/2$ is a constant and the material parameters are calibrated as $\mu_1 = 0.37$, $\mu_2 = 0.70$, $\phi_m = 0.62$, $b = 5$, as shown in Figure 3-11 (a,b). Eq 3.20 gives the solid phase stress ratio when the material is flowing ($\dot{\gamma} \neq 0$ or I_m, $I_v \neq 0$). When the

granular material is not flowing, the solid shear stress is limited by the flow criterion: $\bar{\tau} - \mu_1 \, p_p < 0$.

Maurin et al. [122] have shown that the drag law in bedload transport problems can be fitted by the $\mu(I)$ rheology which is originally for dry granular materials. In our cases as well, the dry inertial number I dominates the mixed inertial number $I_m = \sqrt{2I_v + I^2}$ with the ratio $I^2/2I_v = \dot{\gamma} d_P^2 / 2\nu$ greater than 10 above the bed surface. We find the last two terms of Eq 3.20 contribute less than 5% to the value of μ for $\phi > 0.05$; these terms serve primarily to recover the suspension effective viscosity in the dilute limit. As shown in Figure 3-11(c), the I_m based rheology predictions for the bedload flow are still consistent with the DEM-LBM results. In contrast, Figure 3-11(d) shows the $\mu(I)$ relation is consistent with the bedload data, but does not match the rheological simple shear tests when $I^2/2I_v$ is low. In this two-phase framework, we choose to use the more universal $\mu(I_m)$ relation because it can be generalized more easily to suspended load in sediment transport or even other particle laden flow scenarios, as suggested by Baumgarten and Kamrin [7]. Note that neither rheology predicts the observed behavior for $\mu < \mu_1$ in Figure 3-11(c,d), which are caused by nonlocal effects, which will be modeled in an upcoming section.

The last term in Eq 3.20 for the solid phase stress was previously attributed to the fluid shear stress in [7]. We have some freedom in choosing which phase includes this contribution — the phase-wise stress decomposition is not totally known. Its placement does not affect the total stress nor the model's ability to span dilute suspensions, dense suspensions, and dry granular flows (see Baumgarten and Kamrin [7] for more details about how these regimes are recovered). That said, it is reasonable to include as part of the solid stress since it induced by fluid traction on the grains and Eq 3.20 matches our DEM-LBM data more closely.

Turbulent closures

Turbulence in the fluid produces Reynolds shear stresses and turbulent effects on particle drift, which can both influence sediment transport. The Reynolds shear stress can be modeled using mixing length models [128, 129, 130]. Here we use that

of [130] where the mixing length is fully determined by the local granular packing fraction ϕ without integrating or calculating the distance from the bed surface, which can be challenging in complex 2D or 3D cases. The turbulent viscosity is modeled as

$$\eta_t = n\,\rho_f\,l_m^2\,||\boldsymbol{D}_{0f}||, \tag{3.22}$$

with the mixing length formulated as

$$l_m = 3\,d_p\,(\phi_m - \phi)^3. \tag{3.23}$$

ϕ_m is the random close packing fraction of the particles which is $\phi_m = 0.62$ for the DEM grains. The deviotoric part of the fluid stress is then calculated as $\boldsymbol{\tau}_f = 2(\eta+\eta_t)\boldsymbol{D}_{0f}$. Experiments [131] have shown $l_m/d_p \geq 0.2$ is a lower limit of the mixing length at high packing fraction, where wake effects dominate the vertical mixing of momentum, so we use $l_m/d_p \geq 0.2$ as the lower bound of Eq 3.23.

Due to the velocity fluctuations of the turbulent flow, the particles experience an additional drift velocity $\boldsymbol{u}_d$ [132], which is crucial to recover the Rouse profile [133] in sheet flows Chauchat [123]. Here we formulate the model in a general vectorial form:

$$\boldsymbol{u}_d = -\frac{\eta_t}{\rho_f\,\Sigma_s\,\phi}\,\mathrm{grad}\phi, \tag{3.24}$$

where Σ_s is the turbulent Schmidt number and has been shown to be a constant above a certain height from the bed surface in the sheet flow [123]. When implemented into a two-phase solver, we use $\Sigma_s = 0.3$.

Drag law

The interphase drag force density $\boldsymbol{f}_d$ can be modeled using the common drag form

$$\boldsymbol{f}_d = \frac{18\phi(1-\phi)\eta}{d_p^2}F(\phi, Re_d)\,\Delta\boldsymbol{U}. \tag{3.25}$$

For turbulent flows, the velocity difference above is modified to account for turbulent drift as $\Delta \boldsymbol{U} = \boldsymbol{U}_s - \boldsymbol{U}_f + \boldsymbol{u}_d$. The function $F(\phi, Re_d)$ is the dimensionless drag function with $Re_d = (1-\phi)\rho_f ||\Delta \boldsymbol{U}||/\eta$. The Stokes drag law for a single sphere implies $F(0,0) = 1$. One typical way to determine $F(\phi, Re_d)$ is to measure $F(0, Re_d)$ with a single particle and then account for hindrance effects from neighbouring particles, such as the Schiller [134] model:

$$F_1(\phi, Re_d) = F(0, Re_d)(1-\phi)^{-1-h_{\text{Exp}}}, \tag{3.26}$$

where the exponent h_{Exp} is taken as a constant value of 2 in a recent work on the continuum modeling of sediment transport [135] and the expression for $F(0, Re_d)$ is evaluated as $1+0.15Re_d^{0.687}$ for $Re_d \leq 1000$ and $\frac{0.44}{24}Re_d$ for $Re_d > 1000$. Alternatively, $F(\phi, Re_d)$ can also be determined in the Stokes flow limit as $F(\phi, 0)$ and then extended by adding a term related to Re_d. For example, Beetstra et al. [136] proposed the expression below from fitting

$$\begin{aligned} F_2(\phi, Re_d) = \quad & \frac{10\phi}{(1-\phi)^2} + (1-\phi)^2(1+1.5\sqrt{\phi}) \\ & + \frac{0.413 Re_d}{24(1-\phi)^2}\left(\frac{(1-\phi)^{-1} + 3\phi(1-\phi) + 8.4Re_d^{-0.343}}{1+10^{3\phi}Re_d^{-(1+4\phi)/2}}\right). \end{aligned} \tag{3.27}$$

The data from DEM-LBM simulations can serve as a tool to test/validate these two drag laws. The drag force density can be extracted from the net fluid force per particle in our DEM-LBM wide wall-free simulations, and then homogenized layer-wise at each z and averaged over time to produce F. Similarly, ϕ and Re_d can be homogenized layer-wise. The measured dimensionless drag coefficient is compared with the predictions of F_1 and F_2 evaluated at the same ϕ and Re_d values, as shown in Figure 3-12(a). According to Eq 3.25, F will be multiplied by $\phi(1-\phi)$ when used to calculate the drag force density $\boldsymbol{f}_d$, so the comparison of $\phi(1-\phi)F$ is also included in Figure 3-12(b). F_1 and F_2 tend to underestimate the drag because Eq 3.26 and Eq 3.27 arise from considering a fluid flowing through a fixed, isotropic array of grains. When it comes to mobile particles in sediment transport problems or fluidized

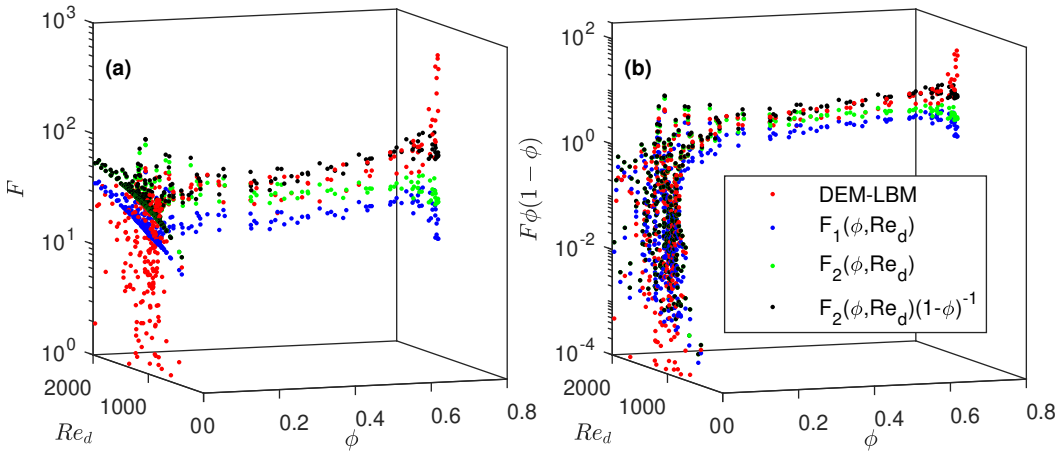

Figure 3-12: Comparison of different dimensionless drag coefficient formulas $F_1(\phi, Re_d)$, $F_2(\phi, Re_d)$ and the modified $F_2(\phi, Re_d)(1-\phi)^{-1}$ against the DEM-LBM results: (e) The dimensionless drag coefficient F as a function of ϕ and Re_d. (f) $F\phi(1-\phi)$ as a function of ϕ and Re_d. The formulas are evaluated at the same ϕ and Re_d values as the DEM-LBM data. F_1 and F_2 tend to underestimate the drag whereas $F_2(\phi, Re_d)(1-\phi)^{-1}$ gives better fitting. Each data point of DEM-LBM comes from a set of homogenized values at an elevation in a WWF test (in total 27 included).

granular beds, the actual drag forces are claimed to be higher than this relation due to granular velocity fluctuations [137, 138], packing heterogeneity [102], and/or packing anisotropy [139, 140]. We account for this effect as follows. The agreement presented in the single sphere settling tests, as shown in 3.2.2, indicates that $F_1(0, Re_d)$ should be recovered in the DEM-LBM simulations. Thus, a simple way to modify the drag law but keep this limit is to multiply $F_1(\phi, Re_d)$ or $F_2(\phi, Re_d)$ above with a correction that is a power of $(1-\phi)$ as an hindrance coefficient [141, 142]. We find the error of the drag law in our system can be reduced by choosing the additional factor to be $(1-\phi)^{-1}$, i.e.,

$$F(\phi, Re_d) = F_2(\phi, Re_d)(1-\phi)^{-1}. \tag{3.28}$$

The proposed formula F fits the DEM-LBM results better than the original formula F_2 for fixed grain arrays.

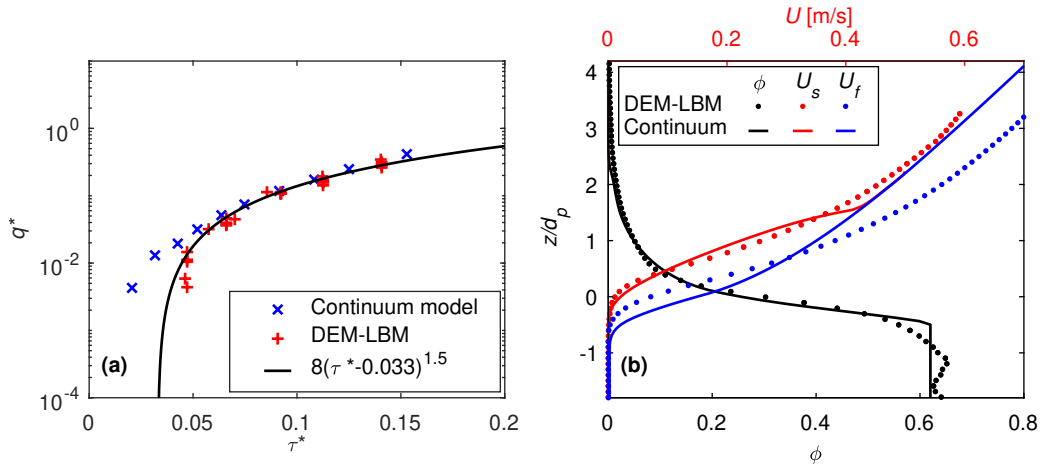

Figure 3-13: Comparison between DEM-LBM simulations and the continuum model for the wide wall-free geometry: (a) sediment transport relation, and (b) flow profiles (WWF2 at $\tau^* = 0.085$) as a function of the height above the bed surface: fluid velocity, solid velocity and solid packing fraction.

3.3.2 Wide wall-free cases

The continuum model with the calibrated material parameters described above has been implemented in a 1D two-phase solver to model the wide wall-free cases. The equations are solved with transient terms and a granular dilation rule [143] using the finite volume method. When the steady state is reached, the transient terms and dilation rule vanish so that the solution is not influenced.

The wide wall-free cases are solved with a given slope S and varied water depth H. The transport relation from multiple solutions is shown in Figure 3-13(a). Each data point represents a single solution for a given H or τ^*. The transport relation from the continuum model matches with that from DEM-LBM simulations, giving a good fit to the widely used (albeit flawed) 3/2 power law. Figure 3-13(b) shows the comparison of the flow profiles from continuum modeling and DEM-LBM simulations. The modeled solid packing fraction profile ϕ matches the simulation almost exactly and the solid velocity profile also matches.

One difference in Figure 3-13(b) is that the solution of the continuum model predicts $\boldsymbol{U}_s$ and $\boldsymbol{U}_f$ to merge into the same profile for $\phi < 0.05$ by observation while in DEM-LBM $\boldsymbol{U}_s$ is always lagging behind $\boldsymbol{U}_f$. The reason for this deviation is that in the DEM-LBM simulations the very top layer of the particles in the dilute suspension

always come up from the granular flow below and they are always slower than the local ambient fluid flow (accelerating streamwise all the way up). On the other hand, there is no such vertical momentum mixing effects (in steady state) in our current continuum model. Moreover, $\boldsymbol{u}_d$ predicted by the continuum model is large enough for the lift force to cancel out the submerged weight of the solid phase, so that the local un-pressurized solid phase sustains no shear stress and co-moves with the fluid phase. For the granular material governed by a frictional flow rule, $p_p = 0$ means the material is suspended and free to be sheared. As a result, there is no drag force in the flow direction (so no velocity lag) for the very dilute layers. For a remedy, there are two future research directions: (1) enhancing the drift velocity formula so that the submerged weight does not fully cancel out, or (2) a granular flow rule for the very dilute regime that considers the vertical mixing of solid phase momentum due to the granular temperature, packing fraction gradient, velocity gradient, and perhaps the gradient of the velocity gradient. Another problem is the abrupt transition to the maximum concentration near bed surface, resulting from the previously mentioned granular flow rule with a flow criterion given by μ_1. The kink corresponds to the elevation where $\mu = \mu_1$, which gives $\phi = \phi_m$ and $\dot{\gamma} = 0$ for all the points below it. Incorporating a nonlocal rheology into the two-phase model may improve the solution near and below the bed surface. As mentioned previously, the drag force density on mobile sheared particles is larger than that on fixed randomly packed particles. More analytical work on this would shed light on the interaction between fluid and solid phases in such flow problems. Finally, we note that this model, which utilizes a standard mixture theoretic decomposition of the stress, is not equipped to model the details of the different stress contributors in each phase beyond the splitting shown in Eqs 3.14 and 3.15. A higher order mixture model could incorporate a micropolar form for the different contributions [126, 127] to permit counterbalancing rotation stresses within each phase to account for the near-bed-surface behavior in Sec 3.2.5, which can be a future research direction.

3.3.3 Creep modeling

For the very dense flow region $\phi \sim \phi_m$ under the bed surface, creep flow (exponential decay of $\boldsymbol{U}_s$) is also observed in DEM-LBM simulations, which is known to be driven by nonlocal effects arising from finite grain size [35, 144, 145]. Creep flow is not contributing much to the $q^* - \tau^*$ transport relation for τ^* far from τ_c^*. However, its effect can matter over the long term, e.g. creep may lead to vertical grain size sorting in river beds [146], and thus accurate modeling of the creeping flow could be helpful to predict river bed armouring.

In the creep zone, the velocities of the particles and the fluid, as well as the relative velocity between the two phases, are so small that the drag forces and lubrication forces from fluid are tiny. One may wonder, hence, if a rheology for the creep of dry granular materials will also work here. We consider the Nonlocal Granular Fluidity model (NGF) [6, 19], which is able to model creep flow in dry granular materials in many cases. In the NGF constitutive model, a phase field called the fluidity, g, is postulated to exist, which satisfies the dynamical partial differential equation:

$$t_0 \dot{g} = A^2 d_p^2 \nabla^2 g - (\mu_2 - \mu_1) \left(\frac{\mu_1 - \mu}{\mu_2 - \mu} \right) g - b \sqrt{\frac{\rho_s d_p^2}{p_p}} \mu g^2 \tag{3.29}$$

where the nonlocal amplitude $A = 0.43$ is a dimensionless constant given by the grain geometry and t_0 is a time-scale. The fluidity then directly controls the stress-flow rheology by the relation $\dot{\gamma} = g\mu$. The “unexpected" flow (i.e. creep) of the solid phase in the region where the load is below the local flow criterion comes from the diffusion term in Eq 3.29, which is scaled directly by the grain size d_p. Recent research [32, 116] shows that g is very likely to be related to the velocity fluctuations of the particles. Thus, the physical picture for the creep flow is as follows: the high granular temperature region of fast flow at the bed surface is a source of g that diffuses downward and “warms up” the cold zone deeper into the bed so that it too can flow. The NGF model parameters are usually fitted from the inertial flow rule for dry granular materials mentioned in 3.3.1. Equation (3.18) then closes the system of equations.

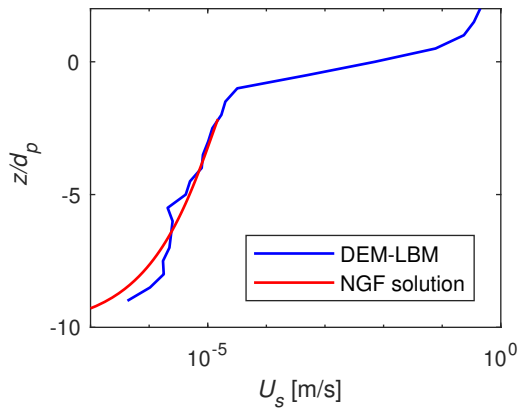

Figure 3-14: The solid phase velocity profile comparison between a DEM-LBM wide wall-free simulation (d_p=5mm, $S = 0.016$) and the corresponding steady state NGF solution.

We solve the NGF model in the wide wall-free flow geometry with some aid from the DEM-LBM results. Since Eq 3.18 needs the fluid forcing, $-\boldsymbol{f}_d - \phi\,\mathrm{grad}(p_f)$, which is not computed from NGF, we simply extract this field directly from the fluid forces in the corresponding DEM-LBM simulation. The g field also needs reasonable boundary conditions. We set $g = 0$ at the bottom of the bed ($z = -10d_p$) and set the g value at $z = -2d_p$ from DEM-LBM tests (using $g = \dot{\gamma}/\mu$) at $z = -2d_p$. Then the velocity of the solid phase can be integrated from the fixed bottom using the solved g field. Figure 3-14 gives the solid phase velocity profile comparison between the DEM-LBM wide wall-free simulation (d_p=5mm, $S = 0.016$) and the corresponding steady state NGF solution. The NGF result shows an exponential decay with a decay length of $\sim 2.5d_p$, in agreement with our DEM-LBM results as well as separate experimental measurements from immersed sediment beds [147] and dry granular beds [148] in similar geometries. This confirms our expectation that the minimal effect of fluid in the deeper zones causes the material to creep as a dry media would.

3.4 Discussion

With regard to the motivating questions asked in the introduction, our study provides the following outlook.

How important is fluid-particle angular momentum transfer and in which part of the flow and in which regime of the sediment transport is it important?

Our simulations resolve the fluid traction over the particle surfaces, leading to a hydrodynamic net force on the center of each particle along with a fluid net couple. Examination of particles entrained by fluid on the bed surface in intermittent sediment transport flume simulations show that nearly $1/4$ of the total fluid torque to roll over neighboring grains comes from the net fluid couple, which is non-negligible especially near the transport threshold. In each wide wall free simulations, the rotation stress, which measures the skewness of the fluid-imposed stress contribution in a grain, seems to be concentrated near the sediment bed surface where it is balanced by the torque resistance arising from the enduring contact with other bed particles. The maximum rotation stress seems not correlated to the Shields number (in the tested range from $0.0471 - 0.1408$), which can be seen as a material indicator of how much fluid net couple the sediment bed can sustain (on the other hand, it is part of the hydrodynamic driving). On the other hand, the fluid net force per grain appears correlated to τ^*. As a result, the influence of the fluid net couple (or the defined rotation stress) is most evident for $\tau^* \to \tau_c^*$ and is negligible for $\tau^* \gg \tau_c^*$, which is shown in this study in terms of the sediment transport relation. This analysis suggests fluid-DEM simulation methodologies that do not explicitly model the small scale fluid-grain interaction may need to use a closure for the angular momentum transfer, such as in Finn et al. [63] and Guan et al. [64], especially when close to the sediment transport threshold.

What is (not) responsible for the variability in the observed sediment transport relation?

The dimensional analysis and the relevant parameter space exploration with DEM-LBM simulations lead to several conclusions, though limited to the simplest geometry (a infinite long and wide straight river) without considering vegetation or external

agitation. In terms of macroscopic factors, the bed slope has little influence on the dimensionless sediment transport rate on gentle slopes (when τ^* is fixed) and is likely not responsible for the variation in flux (q^*) for a given Shields number (τ^*) in experiments [8]. This is not a surprise, in agreement with recent theoretical works [59, 56] about the influence of (steep) slopes on the transport relation, which give correction factors of q^*, τ^* and τ_c^* very close to 1 for gentle slopes ranging from 0.01 to 0.03.

In terms of microscopic particle properties on which this study focuses, tests that independently varied the mean particle size, surface friction coefficient, and surface damping coefficient do not appear to produce transport relations that differ much compared to the reference case at medium to high transport stages. When it is close to the transport threshold, the q^* values in these different simulation groups seem to be inversely correlated to the rotation stress which is correlated to the surface friction coefficient and damping coefficient of the particles.

Following the previous logic regarding the competition between driving factors to dislodge bed particles (collisions and interactions with fluid) countering the resistance from the contact interactions, if we look back at the factors we isolated at the beginning of this analysis, the grain shape [149, 150, 151] via its effect on the frictional resistance and hydrodynamic interaction [152], and size distribution (including effects such as small particles hiding behind large neighbors), may have contributions to the variation in the transport relation. From a different perspective, large particles on river beds also control morphological stability [153, 154], which is possibly another reason. This agrees with the findings of the companion experimental work [72], in which the $q^* - \tau^*$ relation is parameterized primarily by the repose angle of the sediment particles and the ratio of the effective drag coefficient to the drag coefficient of the volume-equivalent sphere. Though the particle surface friction coefficient μ_p influences the repose angle, the influence for round particles is very limited when $\mu_p > 0.05$ [155, 156, 31], consistent with the fact that μ_p has a minor influence on the value of the maximum rotation stress. As a result, μ_p has negligible influence on the transport of spherical sediment particles, but may potentially have more influence on the transport of non-spherical particles.

Besides the microscopic particle properties, other factors that may also play important roles in the variation of the transport relation include the presence of external agitation [76, 77, 78] and vegetation [74, 75]. It should also be noted that here we have only considered the case of simple channel geometry, whereas in actual riverbeds there are a number of channel morphologic features we have not considered that can make a difference, including bedforms [157] and the ratio of grain diameter to flow depth, especially if boulders are present that are not fully submerged [81, 79, 80].

How can we formulate a useful, broadly applicable model at different scales and regimes in bedload sediment transport?

The two-phase continuum framework shown here can be used to predict the bedload transport relation with proper closures: a granular flow rule, a turbulent closure, and a drag law. The transport relation predicted by the model in the wide wall-free cases matches with that from DEM-LBM simulations, giving the classical power law of 3/2. The modeled solid packing fraction profile matches the simulation almost exactly and the solid velocity profile also matches.

For creep flow beneath the bed surface, the success of the NGF model, which has previously been used for dry media, suggests that the physics of cooperative grain motion giving rise to creep in fluid-submerged dense packings may be similar to that in dry packings. In our implementation here, drag forces from the fluid were homogenized from DEM-LBM simulations and applied to the NGF domain as a body force and the fluidity value is specified on the top as the boundary condition. Note that the NGF model does not require $\mu > \mu_1$ anywhere for non-zero flow to exist. As long as there is a finite fluidity boundary condition, flow can happen all beneath μ_1. For example, the presented solution in Section 3.3.3 is obtained by solving the solid field in the creep zone $z \leq -2d_p$ with $\mu < \mu_1$ everywhere. Finite fluidity occurs at the bed surface even if $\mu < \mu_1$ there because the turbulent fluid imparts fluctuations to the bed surface particles resulting in a fluidity source. This interpretation utilizes the result in Zhang and Kamrin [32] that shows fluidity is in fact a measure of grain

fluctuations, so any agency that imparts grain fluctuations can be a source for fluidity in a granular system. We have inferred the fluidity boundary condition from the DEM-LBM simulations, but in principle one could identify a model for the fluidity boundary conditions that depends on the turbulence. In the future we could extend the granular rheology used in our two-phase mixture model to incorporate NGF in the creeping regime, so that fluid flow and granular flow fields are simultaneously computed down to the creeping flow regime. We also acknowledge that creep flows can happen when μ is below μ_1 everywhere [49, 158], the boundary values may be what we want to predict instead of an input. See the review paper [159] for more insights.

The continuum tools we have used make a number of direct ties to the particle-scale information, which can be exploited to apply the model to other bed materials. For example some of the parameters in the drag law at the dilute limit can be calibrated with single particle settling tests. The critical stress ratio μ_1 can be approximated by the static angle of repose of the grains (even if dry). Other parameters in the granular flow rule can be calibrated with basic flow tests. For example, the nonlocal amplitude used in the creep flow model can be inferred from the decay length of the mean particle velocity in wall-bounded chute flows [160, 161] or from annular Couette flow tests [6, 31].

3.5 Concluding remarks

In this chapter, sub-grain scale resolved DEM-LBM simulations of mono-disperse spherical sediment particles were performed and the results compared closely with data from flume experiments. The simulations was shown to match the experiments in terms of the transport relation and the detailed flow profiles of the granular material. With validation in hand, the DEM-LBM tool was then used as the basis for an in-depth modeling study of sediment transport. Wide wall-free simulations were performed in order to evaluate the factors that can potentially affect the transport relation on gentle slopes ($0.01 \sim 0.03$). The slope, the mean particle size, the sur-

face friction coefficient, and the damping coefficient did not appear to influence the dimensionless transport rate for medium to high Shields number when the Shields number was fixed, for spherical sediment particles. Instead, the parameters not included in the dimensional analysis may be responsible for a substantial fraction of the variability in the experimental transport relation on gentle slopes, including particle parameters such as the particle shape and size distribution as well as vegetation, external agitation, bed forms and so on. The particle-resolved simulations also provided details about the fluid-particle angular momentum exchange. The fluid couple with respect to the center of the grain, resulting from the fluid traction over the particle surface, was shown non-negligible for the fluid entrainment near the threshold. The fluid couple was further quantified as the rotation stress, which was found mostly concentrated near the bed surface and not correlated to the Shields number. Particle properties (e.g. surface friction coefficient) changed the observed rotation stress, which was anti-correlated to q^* near the transport threshold, suggesting fluid-particle angular momentum transfer may play a role in transport behavior near the threshold.

Chapter 4

Fluid-driven transport of natural shaped sediment particles

4.1 Background

The results from the previous chapter have shown that the dimensionless transport rate of round particles is not influenced by macroscopic factors (the slope or fluid depth) or microscopic particle properties (mean particle size, particle surface friction or grain-grain damping) for gentle slopes ($0.01 \sim 0.03$) at a medium to high fixed Shields number. One may wonder how much the factors isolated (the size distribution and particle shape) in the previous analysis will influence the transport relation. The size distribution effect has been examined and quantified in multiple works [162, 163, 164]. This chapter mainly discusses the shape effect of the sediment particles.

The sediment particle shape has been long considered to have influences on the sediment transport relation [165, 166, 167, 168, 169, 151], such as the granular dynamics [170] and the threshold of transport [171, 172, 151], but it is rarely quantified [173]. Recent experiments [72] have shown when parameterized by the repose angle of the sediment particles and the ratio C^* of the effective drag coefficient C_D to the drag coefficient of the volume-equivalent sphere C_o, the dimensionless sediment transport

relation of particles in different shapes can be collapsed into a single master curve:

$$q^* = \alpha_o \left(\frac{C^*}{\mu^*} \tau^* - \tau^*_{co} \right)^{3/2}, \tag{4.1}$$

where α_o and τ^*_{co} are the transport coefficient and threshold of motion for idealized spheres independent of grain shape. $\mu^* = (\mu_s - S)/(\mu_o - S)$ is the average bulk friction coefficient μ_s normalized by the bulk friction coefficient of spheres μ_o with consideration of the bed surface slope S. In $C^* = C_D/C_o$, C_D is calculated as the product of the drag coefficient of the particles settling in still water, $C_{D_{settle}}$, and the Corey shape factor S_f, which accounts for the fact that the orientation of the settling particle in still water prefers the largest drag while the orientation of the transported sediment particle is always changing due to rotation. The particle shape is characterized by three mutually perpendicular lengths ($c \leq b \leq a$) [174] of the minimum bounding box [175] and S_f is defined by the ratio $c/\sqrt{ab}$ [176]. $C_{D_{settle}} = \frac{4}{3}\frac{\rho_s - \rho_f}{\rho_f}\frac{gd_o}{w_s^2}$ is obtained from the settling velocity in still water w_s. d_o is the diameter of the volume-equivalent sphere, which is also used in the calculation of q^* and τ^*. $C_o = \frac{4}{3}\frac{\rho_s - \rho_f}{\rho_f}\frac{gd_o}{w_o^2}$ is obtained from the settling velocity of the volume-equivalent sphere w_o, which can be estimated using the empirical equation [177]:

$$\begin{aligned} \log W_* = \; & -3.7671581564 + 1.9294494593 \log D_* - 0.0981509016 (\log D_*)^2 \\ & -0.0057500855 (\log D_*)^3 + 0.0005600075 (\log D_*)^4, \end{aligned} \tag{4.2}$$

where $W_* = w_o^3/(Rg\nu)$, $D_* = Rgd_o^3/\nu^2$ and ν is the kinematic viscosity of water.

The newly proposed transport relation Eq 4.2 has been tested on 5 different particle shapes in flume experiments, from spheres to natural shaped particles. Since the physical experiments can not freely vary the two key factors (repose angle and drag coefficient) and some variables (such as the stress field and the orientation of the particles) can not be easily measured in the experiments, one may want to seek the help of numerical simulations, for example to further check the robustness of Eq 4.2 by independently controlling/varying the factors and to understand the microscopic

Table 4.1: Recent discrete simulations of the sediment transport of non-spherical particles.

Numerical studies	Solid	Fluid	Coupling
Schmeeckle, 2014	Spheres	LES	Empirical drag law
Bravo et al., 2018	Ellipsoids	Imposed	Analytical drag law
Zhang et al., 2020	Ellipsoids	LES	Interfaces resolved
Jain et al., 2021	Ellipsoids	DNS	Interfaces resolved
Sun et al., 2017	Bonded-spheres	LES	Empirical drag law
Alihosseini & Thamsen, 2018	Multi-spheres	RNG $k-\varepsilon$	Empirical drag law
Shao et al., 2019	Multi-spheres	$k-\varepsilon$	Empirical drag law
Fukuda & Fukuoka, 2019	Multi-spheres	LES	Interfaces resolved
Fukuoka et al., 2014	Multi-spheres	LES	Interfaces resolved
This work	Multi-spheres	LES	Interfaces resolved

mechanisms.

In terms of the numerical methods, the discrete simulations of the sediment transport of non-spherical particles differ in 2 dimensions: the representation of the particles and the representation of the fluid. The detailed numerical techniques in recent studies of the non-spherical sediment transport are listed in Table 4.1.

For the fluid representation, some may simply impose an undisturbed fluid velocity field, such as Bravo et al., [178]. The fluid phase is mostly solved on meshes using the finite volume method (FVM) or the finite element method (FEM) with a turbulent closure (such as large eddy simulations, as know as LES) or with enough resolution even for the smallest eddies (direct numerical simulation, as know as DNS). The length-scale the fluid is resolved also decides the way how the fluid-particle interaction is handled. When the grid size is greater than or comparable to the particle size, the momentum exchange is estimated using analytical or empirical drag laws based on the homogenized solid fields (such as packing fraction and velocity). When the grid size is much smaller than the particle size, the interface can be resolved and the momentum exchange on individual particles can be integrated more accurately.

The discrete simulations are all based on DEM, in which the particles are individually tracked. The earliest work [61] uses an empirical drag law for irregular sand particles, though the solid phase is still represented by spheres. Ellipsoids [178, 179, 151] are one of the easiest representations of the non-spherical shapes. Besides the single-

particle representation, the clustered-particle approach is getting popular in recent years [180]. Sun et al. [181] bond/glue spheres together (no overlaps) to represent geometrically rough particles, but the shapes are not commonly seen in real problems due to the large crevasses between the spheres in contact. Another type of clustered-particle approach – the multi-sphere technique which uses overlapping spheres to approximate non-spherical shapes was first introduced for dry particle simulations [182, 183]. It was later adopted in the numerical studies of sediment transport [184, 185, 186, 187]. It is worth noting that most of the previous numerical studies use multi-sphere particles of a single shape in each simulation. Only Fukuoka et al. [186] used different realistic shapes in a single simulation. As more accurate algorithms to approximate real particles using the multi-sphere method are developed [188, 189], simulating the sediment transport of realistic natural shaped particles has been made possible. The literature mentioned above are mainly recent progress. For earlier research works, please refer to this review paper [190] in 2016.

This chapter is dedicated to study the role of particle shape in bedload sediment transport processes using fully coupled discrete particle-fluid simulations. Compared with the previous numerical works, the novelties of this chapter are:

- more accurate shape representations with the most recent multi-sphere approximation algorithm,
- many distinct realistic natural gravel shapes (more than 600 shapes) from CT scanning in each simulation,
- a close benchmark with the corresponding flume tests.

In terms of the numerical method, this is also the first implementation of DEM-LBM based multi-sphere simulations.

4.2 Discrete simulations

This section describes the workflow for the numerical study of the bedload sediment transport of natural shaped particles, from particle shape measurement and approx-

imation to the coupled simulations of the multi-sphere particles.

4.2.1 Method: multi-sphere technique

Multi-sphere approximation of the natural gravel shapes

The particle shapes are reconstructed [191] from the CT scanning results of natural shaped particles in the flume tests [72]. Here we introduce the key information related to the scope of this chapter. Based on the scanning results, a greedy heuristic algorithm was employed to superimpose the overlapping spheres, which is adapted from the algorithm proposed by Li et al. [189]. After uniformly discretizing the scanning result into a bunch of cells, a sphere is inserted inside the shape such that the sphere encompasses the most number of cells. When a new sphere is required to be inserted, the sphere that adds the most number of cells into the occupied volume is selected. This repeats until the desired number of spheres have been inserted for the shape approximation.

Figure 4-1 (cited from Rushlow's work [191]) shows the comparison between the original scanned result and the approximations using different numbers of component spheres. It seems a cluster of 20 component spheres can capture the shape of the natural shaped particles fairly well, without creating too much overfitting near the thin edges. In the following of this chapter, the shape of each natural shaped particle is approximated using 20 constituent spheres. More detailed descriptions of the CT scanning, the shape approximation procedures, and the quantification can be found in Matthew Rushlow's Bachelor degree thesis [191]. After fitting the shape, one more step of length-scale re-scaling is carried out to make sure the volume of the multi-sphere particle matches that of the scanned shape, since the insertion process under-represents the volume on its own. This additional step is crucial since the newly proposed transport relation [72] relies on the diameter and settling velocity of the volume equivalent sphere. Note that the volume of the multi-sphere particle is decided by counting the number of cells encompassed in the envelope, so the overlaps are not double counted.

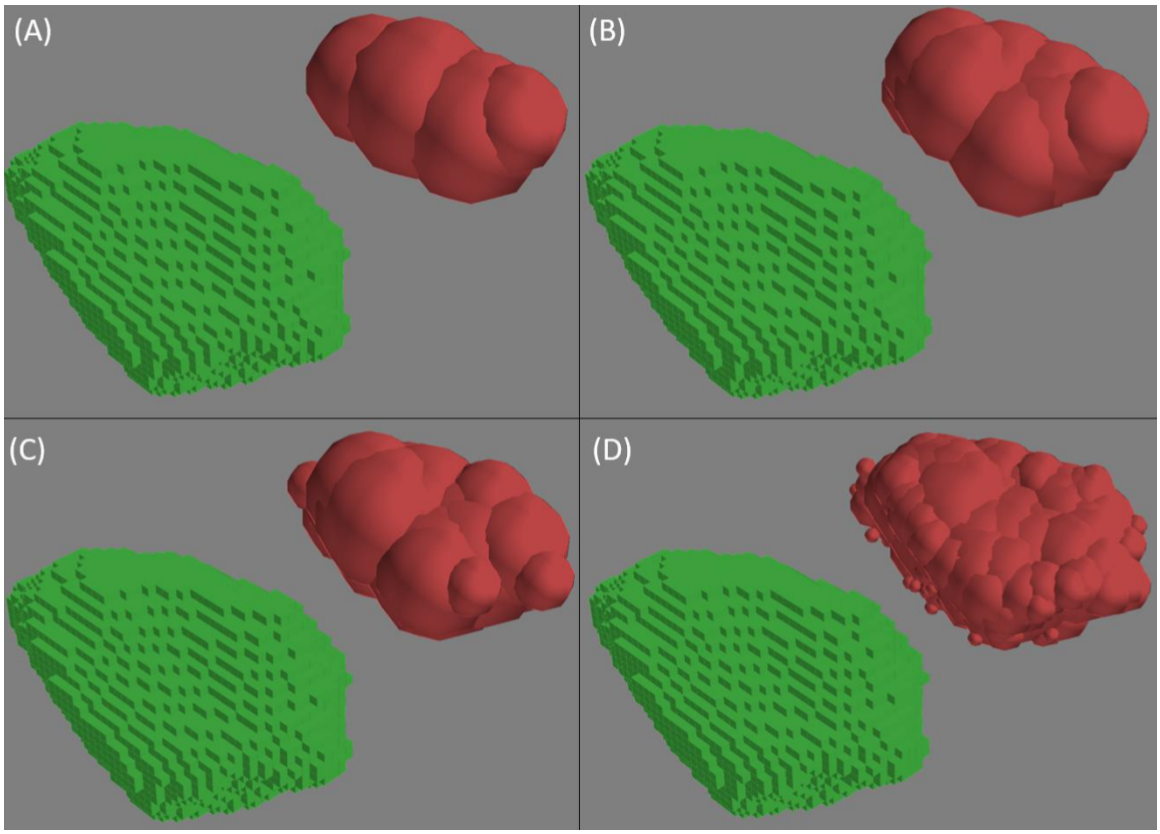

Figure 4-1: Multi-sphere approximation using different numbers of spheres (green: the original natural grain from CT scanning; red: the multi-sphere approximation). (A) A 5 sphere recreation. (B) A 10 sphere recreation. (C) A 20 Sphere recreation. (D) A 150 Sphere recreation. Figure cited from Matthew Rushlow's Bachelor degree thesis [191].

Coupled DEM-LBM scheme

In the previous chapter, being validated against the corresponding flume experiments, the coupled DEM-LBM scheme has shown the capability of recovering the sub-particle scale physics in the bedload sediment transport of spherical particles. It is straightforward to modify the DEM-LBM coupling scheme of spherical particles in Figure 3-2 for multi-sphere particles as shown in Figure 4-2.

Besides the information stored on fluid nodes and particles, the DEM-LBM scheme for multi-sphere particles also stores the information on each multi-sphere particle or shape. The position and velocity of the spheres are used to update the solid domain felt by the fluid. Then momentum transfer is dealt with in the same way as the

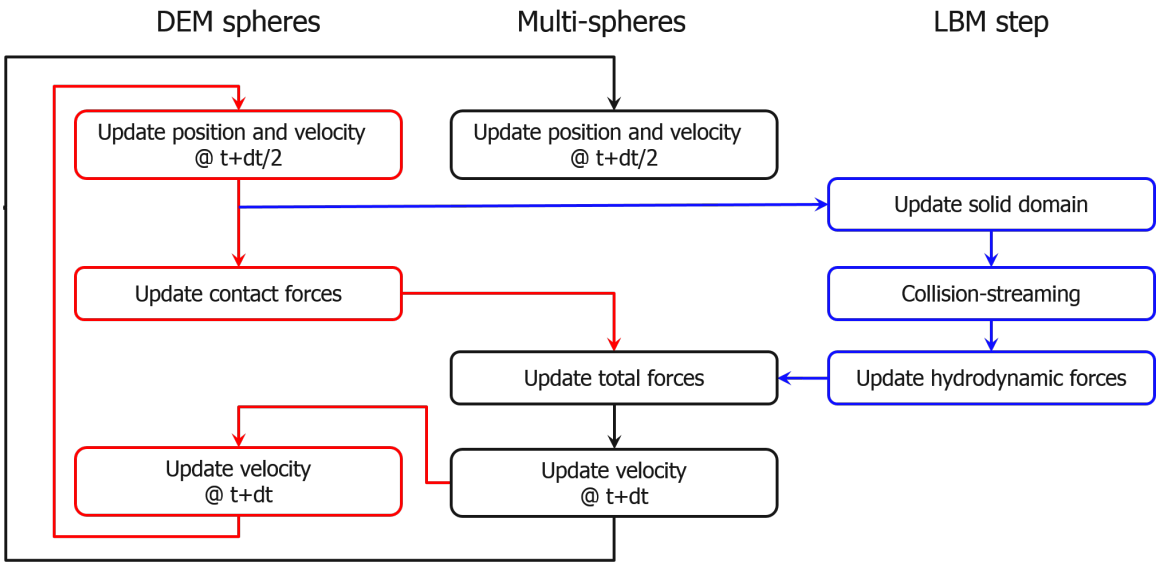

Figure 4-2: DEM-LBM scheme with multi-sphere particles.

DEM-LBM for spherical particles as long as a moving fluid-solid interface has been detected. Then, instead of passing the (linear and angular) momentum transfer back to the spheres, they are integrated on each shape. Similar to the original DEM-LBM scheme, the hydrodynamic forces (and torque) on each shape in the current and the previous LBM steps are averaged when conducting the DEM update, to reduce numerical oscillations. The sphere-sphere contacts are carried out without considering the interaction of the component spheres in the same shape. By summing these two contributions of momentum transfer and the buoyancy force, the linear and angular acceleration of each shape can be decided, which is further used to update the velocity and rotational velocity of the shape. Then in each rigid body (shape), the constituent spheres share the same angular velocity as the shape. The velocity of each component sphere is updated according to the velocity of the shape as well as the cross product of the angular velocity and the position of the sphere relative to the center of the shape. Note that the acceleration of each sphere also needs to be obtained, which will be used for the update of position and velocity in the middle of the time step. Special care should be taken regarding the linear acceleration originated from the rotation of the shape, which can be seen as a constraint for the rigid body.

4.2.2 Benchmarking: repose angle and settling velocity

Before setting up flume simulations for the comparison of the sediment transport relation with the experiments, the material properties of the natural shaped particles need to be benchmarked. The natural shaped particles have an average density of $\rho_s = 2471\,\mathrm{kg/m^3}$. The diameter of the volume equivalent sphere is $d_o = 4.1\mathrm{mm}$. The average settling velocity is $w_s = 0.286\,\mathrm{m\,s^{-1}}$ whereas the settling velocity of the volume equivalent sphere is $w_o = 0.436\,\mathrm{m\,s^{-1}}$, corresponding to drag coefficients $C_{D_{settle}} = 0.67$ and $C_o = 0.42$. The repose angle of the dry material is 38°. For More details about the measuring methods and other properties, please refer to this paper [72].

The previous subsection described how the shape and volume of the multi-sphere particles are matched with the scanned natural shaped particles, which means d_o and w_o have also been calibrated. Beside the average size d_o, the Corey shape factor S_f (relative flatness) should also be benchmarked since it is used in the calculation of C_D. The S_f value of the multi-spheres measured to be 0.67 exactly matches that measure from the scanning results, confirming that multi-sphere approximations using 20 constituent spheres can capture the natural shapes well.

Here we are going to check other important particle properties in Eq 4.1: repose angle of the dry material and the average settling velocity in still water. The repose angle test has been carried out using the multi-sphere particles with both the particle-particle and wall-particle friction coefficients of 0.8, mimicking a rough table. Figure 4-3a shows a snapshot of the pile of multi-sphere particles. We can also get the radial locations of the constituent spheres and plot them with the vertical positions, as shown in Figure 4-3b. The repose angle in the simulation is measured as 37°, close to the 38° repose angle measure in the experiment. After pouring down nearly 1800 particles, the pile ended up with a similar size to the experiments in which a rim of particles were glued on the table with a diameter of 12cm (see Figure 4-3b, the 37° slope approximately ends at the radius of 6cm). The large repose angle of the natural shaped particles is due to the particle shape and insensitive the particle

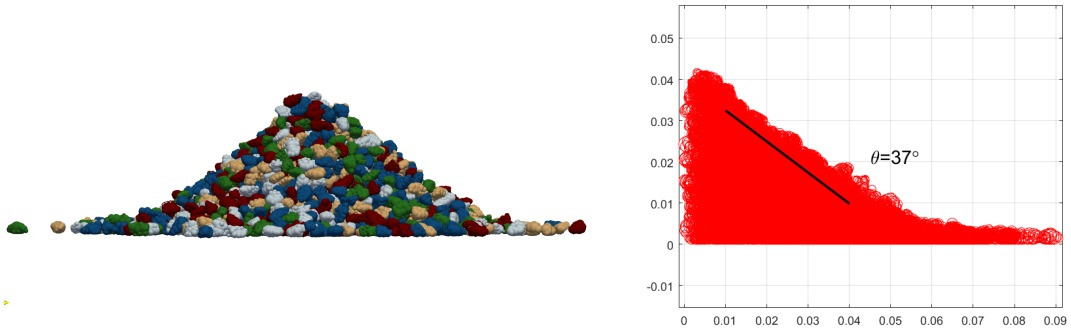

(a) (b)

Figure 4-3: Repose angle simulation of the multi-sphere particles. In total nearly 1800 particles in 627 distinct shapes (none used more than 3 times). (a) Snapshot of the simulation result. (b) Radial location of the particles in the pile, with respect to the center line, plotted with the vertical position. The multi-sphere particles shows a 37° repose angle.

surface friction coefficient.

For DEM-LBM simulations of round particles, Feng and Michaelides [101] and Derkse [102] have shown that a resolution of $dx \leq d_p/6$ or $dx \leq d_p/8$ is adequate for sufficiently accurate results. In previous chapter, $dx \leq d_p/10$ is kept to guarantee enough accuracy. Even though $dx \leq d_o/8$ is kept with the same choice of dx in this case, the diameter of the smallest constituent sphere is comparable to the grid size $dx = 0.5$mm in LBM ($\sim 0.9dx$). It is not clear whether the shape is well resolved on the LBM mesh. Since this is the first implementation of DEM-LBM simulations of multi-sphere particles, the convergence of resolution needs clarification. Settling simulations in still water with grid size of dx, $dx/2$ and $dx/5$ are set up with the same set of 34 multi-sphere particles. The number of the tested particles is limited due to the high computational cost of the simulations with a resolution of $dx/5$. The domain size is 3cm by 3cm by 18cm. The side walls are all periodic and the top and bottom are fixed boundary conditions. The average settling velocities with different resolutions is summarized in Table 4.2. The set of 34 particles tested in the simulations is not the same set of 23 in the experiments, so the average settling velocity of these two sets may be slightly different. Even so, the results do show convergence as the grid size

Table 4.2: The average settling velocities on the same set of 34 multi-sphere particles with different resolutions. The experiments measure 23 natural shaped particles.

	dx	$dx/2$	$dx/5$	Experiments
Settling velocity [m/s]	0.254	0.276	0.280	0.286

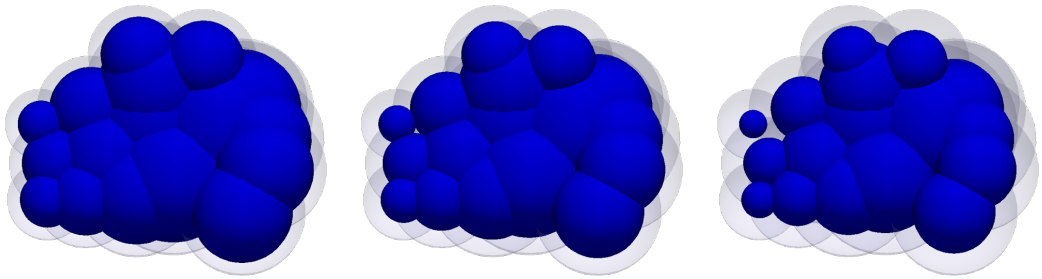

(a) (b) (c)

Figure 4-4: Shrunk particles felt by the fluid with different shrinkage coefficients SK. (a) $SK = 0.40$, (b) $SK = 0.55$, (c) $SK = 0.70$

decreases from dx to $dx/5$. When dx is halved, the settling velocity increases by 8.8%. But as the grid size shrinks further for 2.5 times, the settling velocity is only changed by 1.1% and the value is close to that measured in the experiments (off by 3.5%, increasing the domain size will make it closer to the experimental measurement). For these particles, a resolution of $dx/2 \sim d_o/16$ should be adequate.

However, halving the current grid size by a factor of 2 means the number of fluid nodes in all 3 dimensions will increase by a factor of 2. This will also lead to a halved fluid timestep, which in return makes the total computational cost on the fluid side multiplied by a factor of 16. One may wonder if there is an alternative option to match the settling velocity in still water while keeping the current grid size. The trick is to shrink the size of the constituent spheres universally on the fluid side. Figure 4-4 illustrates this idea with 3 different shrinkage coefficients (shrinkage/dx) SK =0.40, 0.55 and 0.70. The original multi-sphere shape is represented by the semi-transparent envelopes. The average settling velocities on the same set of 480 multi-sphere particles with different shrinkage coefficients are list in Table 4.3. As the shrinkage coefficient increases, the average settling velocity increases as well and

Table 4.3: The average settling velocities on the same set of 480 multi-sphere particles with different shrinkage coefficients.

	$SK = 0.00$	$SK = 0.40$	$SK = 0.55$	$SK = 0.70$
Settling velocity [m/s]	0.246	0.263	0.273	0.286

the rate of the increase goes higher. $SK = 0.70$ gives the same average settling velocity as that measured in the experiments. Note that SK only shrinks the size of the constituent spheres for the fluid, leaving the solid phase (size, interactions, etc.) unchanged. One may wonder why the shrinkage trick is able to tune and match the correct settling velocity. The issue solved here is actually that the crevasses of the approximated natural shapes are at a sub-grid scale, with a low chance to be resolved by the fluid grid when the particles are moving. Consequentially, the grid representation of the fluid mesh artificially makes particles of an awkward shape look bigger on the fluid side. Shrinking the constituent spheres increases the length scale of the crevasses to the grid scale so that these features have higher chances to be resolved on the fluid mesh. This shrinkage trick also provides an opportunity to vary the drag coefficient independently, without changing any other key factor in Eq 4.1.

4.2.3 Comparison with laboratory flume experiments

Deal et al. [72] and Benavides et al. [73] conducted bedload sediment transport experiments with natural shaped particles in a narrow flume, and recorded high-speed videos of the grains. We performed corresponding DEM-LBM simulations as validations specifically to test the accuracy of the developed multi-sphere simulations in sediment transport problems. We compare the time-averaged sediment transport rates as a verification of our simulations, and then vary the drag coefficient of the multi-sphere particle as a further check of the modified bedload transport relation Eq 4.1.

The the flume experimental setup of Deal et al. [72] and Benavides et al. [73] for natural shaped particles are the same as that for spheres in the previous chapter as shown in Figure 3-5 (a). In each experiment, natural shaped particles and water are

fed into the inclined flume from the upstream end at a given combination of volume flux rates. After the initial period of sediment deposition, the granular bed builds up and steady state is reached. Then the slope of the free water surface S as well as the water depth are measured, and the particle motion is recorded by the high-speed cameras in the middle section of the flume. The flume is 10.2mm wide.

The simulated flume has a length $L = 0.12$m and height 0.15m. The LBM lattice has homogeneous grid size $dx = 0.5$mm. The first and last nodes across the flume align with the side walls, and the simulated flume width is adjusted slightly to have $W =$ 10.5mm. The top of the simulated domain uses a free-slip (zero gradient) boundary condition. Note that in this narrow flume configuration, the fluid velocity far above the granular bed surface approaches a constant value due to sidewall shear. The bottom uses a no-slip boundary condition and the two sides perpendicular to the flow direction use periodic boundary conditions. For the two side walls of the flume, see the Navier-type boundary conditions developed in Appendix A for more details. The gravity $g = 9.8\,\mathrm{m/s^2}$ is applied at an angle of slope S with respect to the vertical axis of the simulated domain. The flow is driven by the tilted "horizontal" gravity component. Inside the flume, there are 1000 multi-sphere particles of 627 distinct shapes (each shape at most used twice). The elastic constants for the normal and tangential contacts are set to be $2000\,\mathrm{N\,m^{-1}}$ and $571.4\,\mathrm{N\,m^{-1}}$, respectively, guaranteeing the constituent spheres are in the hard limit. The damping coefficient of the particles is $0.03\,\mathrm{kg\,s^{-1}}$. For more descriptions, shape approximation, and the benchmark of the particle properties with the multi-sphere particles, please refer to the previous subsection.

For the calculation of τ^*, the bed shear stress τ_b is calculated as $\tau_b = \rho_f g S \frac{HW}{2H+W}$, where H is the water depth measured down to the bed surface and W is the flume width. For the calculation of q^*, the sediment volume flux per unit width q_s is counted in the whole domain as $q_s = \Sigma_i Vol_i V_{i,x}/LW$, where $V_{i,x}$ and Vol_i (real volume of the solid shape, not influenced by the shi rinkage coefficient SK) are the streamwise velocity and the volume of the i-th particle, respectively.

The first set of 6 DEM-LBM simulations uses the benchmarked multi-sphere par-

ticles with $SK = 0.70$, having the same average settling velocity as the experiments. The initial condition sets the particles uniformly distributed in the whole domain with no velocity and stationary fluid. As each simulation runs, gravity drives the fluid and grains, resulting in the ultimate formation of a particle sediment bed and a transverse fluid flow profile, which transports the near-surface particles. The simulations are all carried out for at least 40s of simulation time and the last 20s of the simulations are taken to calculate the time averaged values and standard deviation of the integrated flux. The resulting transport relation compared with the experimental results is shown in Figure 3-6(a).

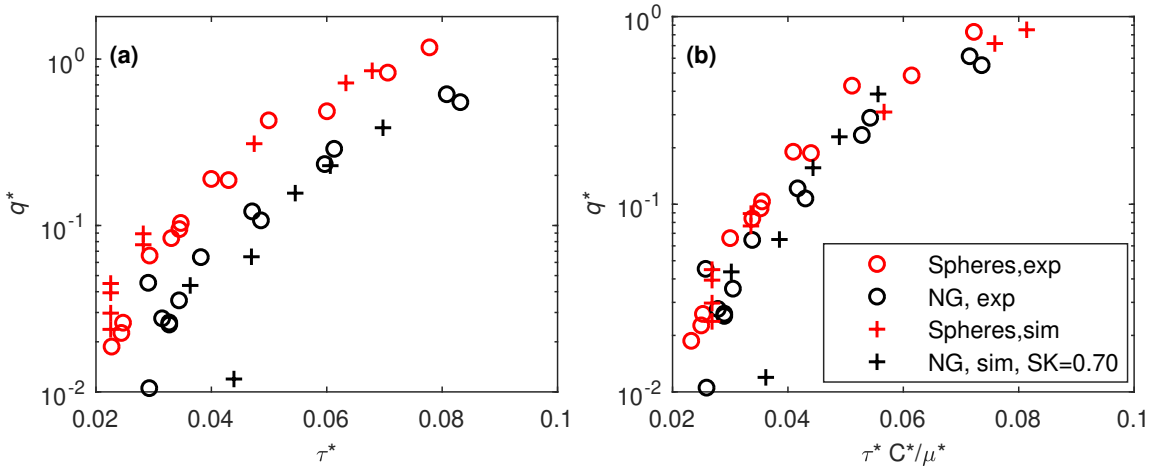

Figure 4-5: Dimensionless sediment transport rate q^* from DEM-LBM simulations of multi-sphere particles. The particles have a shrinkage coefficient of $SK = 0.70$ (making the drag coefficient same as the experiments). (a) Comparison with the q^* vs τ^* relation from experiments. The critical Shields number in the flume experiments is found to be 0.040 ± 0.008 [73]. At the low Shields numbers, the results show strong intermittency near τ_c^*. (b) Comparison with the modified q^* vs $\tau^* C^*/\mu^*$ relation from experiments. The sediment transport relation data of the spherical particles is also plotted in red for comparison. NG: natural gravel.

Overall, in terms of the q^* vs τ^* transport relation, the DEM-LBM simulations are consistent with the experiments. At the low Shields numbers simulated, $\tau^* = 0.036 \sim 0.047$ (τ_c^* found to be 0.040 ± 0.008 [73]), strong intermittency has been observed. For the other 3 data points at medium to high transport stages, the dimensionless transport rate q^* values match well, far below the transport relation

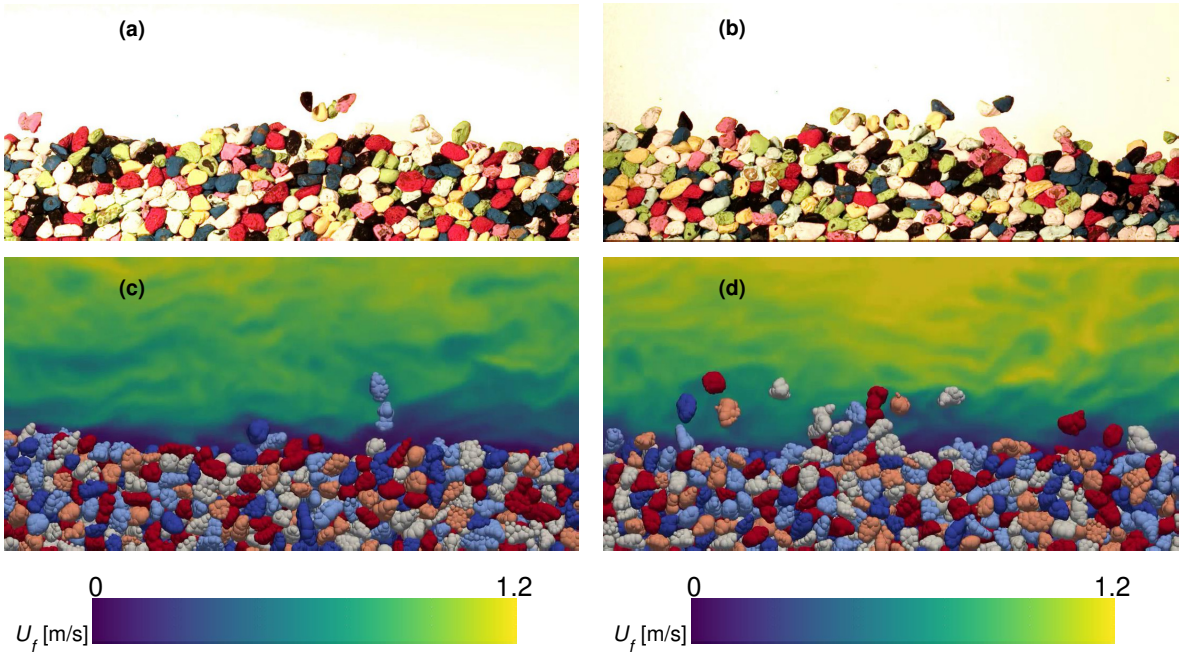

Figure 4-6: Comparisons between the flume experiments and DEM-LBM simulations of multi-sphere particles at Shields number $\tau^* = 0.047$ (left column), and $\tau^* = 0.061$ (right column). (a) & (b) Snapshots of the flume experiments. (c) & (d) Snapshots of the DEM-LBM simulations of the multi-sphere particles, fluid field colored by the fluid velocity magnitude on the center-plane of the flume.

obtained from glass spheres. Figure 3-6(b) shows the data when the horizontal axis is modified from τ^* into $\tau^* C^*/\mu^*$, following Eq 4.1 as proposed recently in the corresponding experiments [72]. The numerical results of the multi-sphere particles and glass spheres as well as the corresponding experimental results collapse onto the same master curve. Besides the flux rate of the natural shaped particles, the simulation results are also similar to the experiments in terms of bed surface structure and the collective behaviours of the transported particles, as shown in Figure 4-6 at two different Shields numbers. With the values of the repose angle of the dry material and the average settling velocity benchmarked, the the multi-sphere simulations have been validated against the corresponding flume tests with natural shaped particles.

The newly proposed sediment transport relation Eq 4.1 has taken two factors into account for the particle shape: the repose angle and the settling velocity. One may wonder if there is a way to vary one of these two factors independently using the benchmarked numerical tool for further validation. Recall that changing the shrink-

age coefficient SK only changes the average settling velocity without influencing the other key factor purely dependent on the DEM: the repose angle of the dry material. As shown in Table 4.3, tuning SK varies the settling velocity (the drag coefficient) independently, providing an opportunity to vary the drag coefficient independently and probe the parameter space as a further check of Eq 4.1. Two sets of DEM-LBM simulations with the same set of 1000 multi-sphere particles but different shrinkage coefficients $SK = 0.55$ and $SK = 0.00$ have been carried out. The dimensionless transport relation is plotted in Figure 4-7(a). For the same set of multi-sphere particles, a larger value of SK reduces the area of the cross-sectional area and decreases the hydrodynamic force, leading to a higher threshold of motion and lower transport rate in general. Interestingly, the multi-sphere simulations with $SK = 0.00$ gives almost the same q^* vs τ^* relation as the glass spheres. The modified sediment transport relation can also be calculated using the average settling velocities for different SK values, as shown in Figure 4-7(b). The collapse of the data points from the same set of particles with different drag coefficients confirms the robustness of Eq 4.1. It also relieves the concern that a shrinkage coefficient of $SK = 0.70$ might be too big a change to the particle shape as shown in Figure 4-4. Even with multi-spheres with smaller SK values, as long as the average settling velocity of the particles are measured and taken into account, the modified sediment transport relation is able to collapse the data onto the master curve.

4.3 Concluding remarks

In this chapter, a complete workflow has been developed for the numerical study of the bedload sediment transport of natural shaped particles, from particle shape measurement and approximation to the coupled simulations of the non-spherical particles. Superimposed spheres are used to approximate the shape of natural shaped particles. The material properties such as the diameter of the volume-equivalent sphere, the repose angle of the dry material and the average settling velocity have been benchmarked with the experiments. Sediment transport tests of the multi-sphere

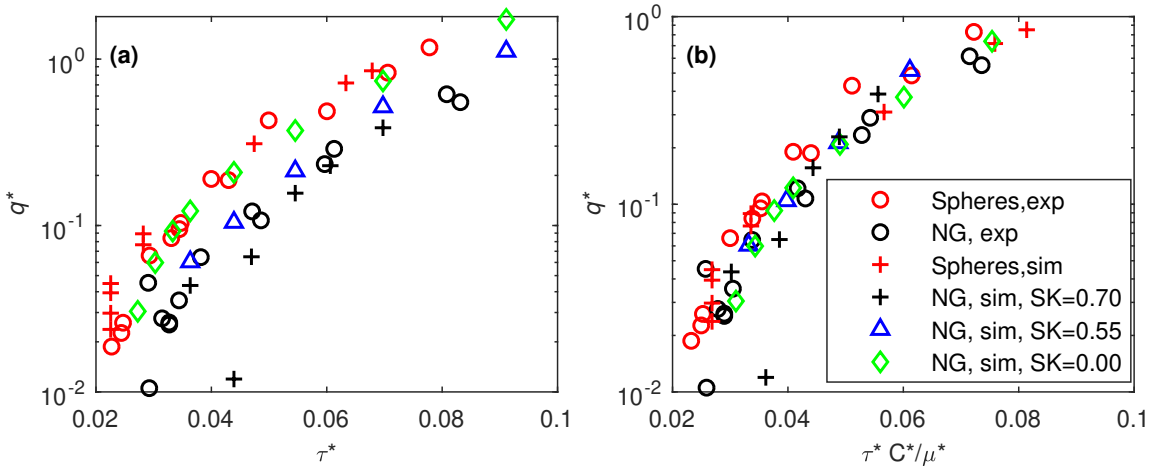

Figure 4-7: Dimensionless sediment transport rate q^* from DEM-LBM simulations of multi-sphere particles with different drag coefficients (varied through shrinkage coefficients). (a) Comparison with the q^* vs τ^* relation from experiments. At the low Shields numbers, the results show strong intermittency near τ_c^*. (b) Comparison with the modified q^* vs $\tau^* C^*/\mu^*$ relation from experiments. Different colors distinguish different shrinkage coefficients (drag coefficients). NG: natural gravel.

particles in the flume have been performed. The results have been compared with data from flume experiments. The simulations has been shown to match the experiments in terms of the transport relation, bed structure and collective behaviours of the particles. With validation in hand, the DEM-LBM tool was then used to test the robustness of the modified sediment transport relation by varying the drag coefficient while fixing all other grain properties via different shrinkage coefficients.

In terms of the numerical method, sub-grain scale resolved DEM-LBM simulations of multi-sphere particles has been implemented for the first time. Compared with the previous numerical works, the novelties of the simulations are:

- more accurate shape representations with the most recent multi-sphere approximation algorithm,
- many distinct realistic natural gravel shapes (627 shapes) from CT scanning in each simulation,
- a close benchmark with the corresponding flume tests.

Chapter 5

General conclusion

5.1 Summary of results

In this thesis, DEM simulations have been carried out as virtual experiments to study the particle-scale physics and then guide the formulation of empirical dimensionless relations or continuum models for two applications: (1) locomotion problems in granular media, and (2) the bedload sediment transport process.

In Chapter 2, dynamic similarity in locomotion problems in granular media has been extended to inclined and cohesive granular beds. Scaling relations for driving performance, namely the power and traveling velocity, have been proposed for wheeled locomotion on these beds. For verification, DEM simulations of different shaped wheels have been performed and the results have confirmed the proposed scaling relations. These scaling relations shed light on how to design experiments in laboratory scales and/or in a different gravitational environment by following the dimensionless groups and serve as a potential design tool for off-road vehicles and extra-planetary rovers, and as an analysis tool for bio-locomotion in soils.

In chapter 3, fluid-driven transport of round sediment particles has been studied. Sub-grain scale resolved DEM-LBM simulations of mono-disperse spherical sediment particles were performed and the results compared closely with data from flume experiments. The simulations were shown to match the experiments in terms of the transport relation and the detailed flow profiles of the granular material. With val-

idation in hand, the DEM-LBM tool was then used as the basis for an in-depth modeling study of sediment transport. Wide wall-free simulations were performed in order to evaluate the factors that can potentially affect the transport relation on gentle slopes ($0.01 \sim 0.03$). The slope, the mean particle size, the surface friction coefficient, and the damping coefficient did not appear to influence the dimensionless transport rate for medium to high Shields number when the Shields number was fixed, for spherical sediment particles. Instead, the parameters not included in the dimensional analysis may be responsible for a substantial fraction of the variability in the experimental transport relation on gentle slopes, including particle parameters such as the particle shape and size distribution as well as vegetation, external agitation, bed forms and so on. The particle-resolved simulations also provided details about the fluid-particle angular momentum exchange. The fluid couple with respect to the center of the grain, resulting from the fluid traction over the particle surface, was shown non-negligible for the fluid entrainment near the threshold. The fluid couple was further quantified as the rotation stress, which was found mostly concentrated near the bed surface and not correlated to the Shields number. Particle properties (e.g. surface friction coefficient) changed the observed rotation stress, which was anti-correlated to q^* near the transport threshold, suggesting fluid-particle angular momentum transfer may play a role in transport behavior near the threshold.

In Chapter 4, a complete workflow has been developed for the numerical study of the bedload sediment transport of natural shaped particles, from particle shape measurement and approximation to the coupled simulations of the non-spherical particles. Superimposed spheres are used to approximate the shape of natural gravels. The material properties such as the diameter of the volume-equivalent sphere, the repose angle of the dry material and the average settling velocity have been benchmarked with the experiments. Sub-grain scale resolved DEM-LBM simulations of multi-sphere particles has been first time implemented and sediment transport tests of the multi-sphere particles in the flume have been performed. The results have been compared with data from flume experiments. The simulations has been shown to match the experiments in terms of the transport relation, bed structure and col-

lective behaviours of the particles. With validation in hand, the DEM-LBM tool was then used to test the robustness of the modified sediment transport relation by varying the drag coefficient via different shrinkage coefficients.

5.2 Future work

Although significant progress has been made in locomotion problems in granular media and the bedload sediment transport process, there are several areas where significant improvements can be made.

- **Enhancement of the two-phase continuum model in the dilute limit.** In Chapter 3, the solution of the continuum model predicts $\boldsymbol{U}_s$ and $\boldsymbol{U}_f$ to merge into the same profile for $\phi < 0.05$ by observation while in DEM-LBM $\boldsymbol{U}_s$ is always lagging behind $\boldsymbol{U}_f$. The reason is that the particle phase pressure p_p is 0 in the very dilute layers, which means the material is suspended and free to be sheared for the granular material governed by a frictional flow rule. As a result, there is no drag force in the flow direction (so no velocity lag) for the very dilute layers. For a remedy, there are two future research directions: (1) enhancing the drift velocity formula so that the submerged weight does not fully cancel out, or (2) a granular flow rule for the very dilute regime that considers the vertical mixing of solid phase momentum due to the granular temperature, packing fraction gradient, velocity gradient, and perhaps the gradient of the velocity gradient.

- **Development of higher order mixture model for the stress asymmetry of the fluid traction.**

  In Chapter 3, the net angular momentum transfer between the fluid and the sediment particles (especially near the bed surface) has been quantified as the asymmetry of the phase-wise stress tensors in both phases, though the total stress tensor is still symmetric. The presented continuum model, which utilizes a standard mixture theoretic decomposition of the stress, is not equipped to

model the details of the different stress contributors in each phase beyond the splitting shown in Eqs 3.14 and 3.15. A higher order mixture model could incorporate a micropolar form for the different contributions [126, 127] to permit counterbalancing rotation stresses within each phase to account for the near-bed-surface behavior in Sec 3.2.5, which could potentially be further connected to the bed surface structures such as sorting and armoring.

- **Incorporation of the non-local granular flow rule in the two-phase mixture model.**

  In Chapter 3, though the sediment transport and the creep flow below the sediment bed surface have been modeled, two separate models are utilized: the two-phase mixture model and the non-local granular fluidity model. In the future we could extend the granular rheology used in our two-phase mixture model to incorporate NGF in the creeping regime, so that fluid flow and granular flow fields are simultaneously computed down to the creeping flow regime. We also acknowledge that creep flows can happen when μ is below μ_1 everywhere [49, 158], the boundary values may be what we want to predict instead of an input.

- **Physical interpretation of the modified sediment transport relation.**

  In Chapter 4, the modified sediment transport relations [72] has should its robustness on predicting the transport rate of sediment particles of different shapes. However, the physical meaning of this modification $\tau^* C^*/\mu^*$ in Eq 4.1 to the traditional transport relation is still not fully understood. The validated DEM-LBM simulation of multi-sphere particles provides a tool to study the microscopic mechanisms. For example, the hydrodynamic forces and the orientations of the transported particles may be monitored. If a preferred axis of rotation is found on the moving particles, it may give hints on why the Corey shape factor (relative flatness) plays an pivotal role in $C^* = C_{D_{settle}} S_f / C_o$. Better understanding of the microscopic mechanisms can also help improve the modified transport relation.

There are many other areas of potential improvement for the methods and models presented in this thesis. However, these areas here present the most straightforward improvements that are apparent to this author.

Appendix A

Wall boundary layer treatment for flume tests

To ensure the fluid velocity in the DEM-LBM simulations, it is correct is crucial to recover the transport relation of the sediment particles. In the flume experiments [72, 73], the flumes are narrow and tall so that the cross-sectional fluid streamwise velocity far from the granular bed can be approximated by the law of the wall when fully developed. According to the law of the wall, the velocity near the wall (viscous sublayer, $y^+ < 10.8$) is linear to the wall distance $u^+ = y^+$ with $y^+ = y_w u_\tau / \nu_f$, $u_\tau = \sqrt{\tau_w / \rho_f}$ and $u^+ = u/u_\tau$, where y_w is the distance to the closest wall of the channel and τ_w is the wall shear stress. Beyond the viscous sublayer, the fluid average velocity not too close to the walls ($y^+ \geq 10.8$) can be formulated as $u^+ = \ln y^+ / 0.41 + 5.0$. The goal of this appendix is to explain how we can recover the turbulent pure fluid cross-sectional velocity profile in the channel without having to directly resolve the boundary layer.

LBM has shown the capability to simulate homogeneous isotropic turbulent flows accurately [92], either on a high resolution mesh whose grid spacing is no larger than Kolmogorov length scale δx_K (as known as Direct Numerical Simulations or DNS), or a relatively coarse mesh with a turbulent closure (LES). Various papers on LBM [192, 193, 194] have shown DNS can recover the turbulent fluid velocity profile in a channel with two parallel walls. However in LBM with LES such as our

simulations, the thickness of the viscous sublayer of the boundary layer is smaller than or comparable with the grid spacing dx, leading to a velocity jump near the boundaries. LBM based LES with a no-slip boundary condition will underestimate the fluid velocity in the channel. Here, we present a new boundary technique, relating the velocity jump across the boundary layer as a slip velocity in a Navier slip boundary condition formulation.

Uth et al. [108] and Wang et al. [109] have provided the implementation method of the Navier slip boundary condition in LBM. The slip boundary condition is characterized by a scalar s_{sl}, the slip length defined as the distance from the wall at which the linearly extrapolated relative velocity is 0. At the boundary, if f_i corresponds to the oblique velocity $\boldsymbol{c}_i$ going into the wall, the distribution component coming out of the wall in the opposite direction can be made up as

$$f_{i'}(\boldsymbol{x}_w, t+1) = r_1\, f_i^c(\boldsymbol{x}_w, t) + (1 - r_1)\, f_{i'''}^c(\boldsymbol{x}_w, t) \tag{A.1}$$

with

$$r_1 = \frac{1}{1 + \frac{s_{sl}}{dx\,(\tau - 1/2)}} \tag{A.2}$$

where $f_{i'''}$ corresponds to the velocity going into the wall in the specular reflection direction (the opposite direction of $\boldsymbol{c}_{i''}$, see Figure 3-1 (c)) and the superscript "c" denotes the post-collision distribution. Substituting Eqn (3.4) and $s_{sl} = u_{sl}/\dot{\gamma}_{f,w}$ gives

$$r_1 = \frac{1}{1 + \frac{u_{sl}}{\dot{\gamma}_{f,w}\nu}\frac{dx}{3dt_f}} = \frac{1}{1 + \frac{u_{sl}}{\tau_w}\frac{dx\,\rho_f}{3\,dt_f}} \tag{A.3}$$

where u_{sl} is the slip velocity and $\dot{\gamma}_{f,w}$ the fluid shear rate at the boundary. Since the node is at the wall, τ_w equals the local shear stress

$$\tau_w = ((C_s \cdot dx)^2 \dot{\gamma}_{f,w} + \nu_f)\dot{\gamma}_{f,w} \tag{A.4}$$

Assuming the second layer of nodes from the wall are right out of the viscous sublayer ($y^+ = 10.8$), then the dimensionless velocity there is 10.8. Extrapolating the

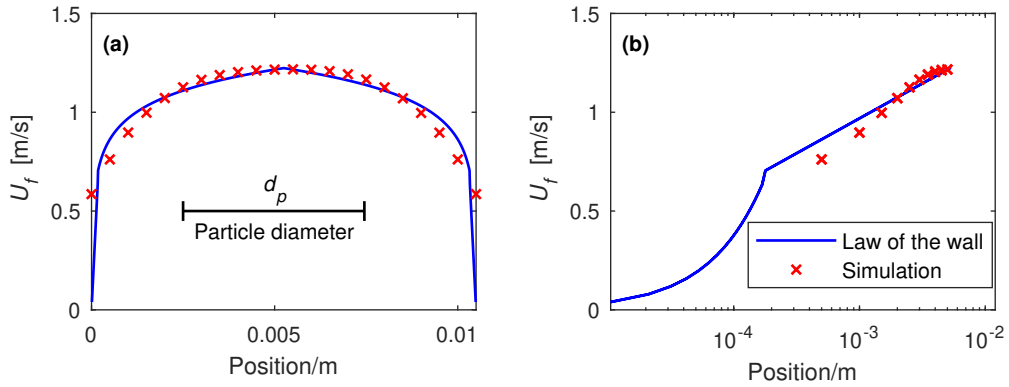

Figure A-1: Turbulent pure fluid velocity across the channel: the law of the wall (solid blue line) compared with an LBM based large eddy simulation with the proposed Navier's slip boundary condition (red crosses), in (a) linear plot, and (b) semi-log plot. The inclined angle of the flume corresponds to a moderate Shields number $\tau* = 0.047$ in Figure 3-6. Note the channel is as wide as $\sim 2d_p$.

logarithmic-law to the wall gives the slip velocity as

$$u_{sl} = 2.35u_\tau. \tag{A.5}$$

Then Eqn (A.1,A.3,A.4,A.5) together give the analytical Navier's slip boundary condition for turbulent channel flow in LBM based LES.

Figure A-1 shows the comparison between the law of the wall and an LBM based large eddy simulation with the proposed Navier's slip boundary condition. The simulated fluid velocity match the law of the wall very well. This simulation also serves as a tool to calibrate the value of $C_s = 0.27$ with the resolution of $dx = 0.005$m. The value of C_s and the grid spacing are used throughout this paper for the simulations in which the fluid is water. With the help of the proposed boundary condition, the shown LBM simulation whose resolutions dx is equivalent to $\sim 15\delta x_K$, is much faster than DNS without losing much accuracy on the fluid velocity.

Bibliography

[1] Peter A Cundall and Otto DL Strack. A discrete numerical model for granular assemblies. *geotechnique*, 29(1):47–65, 1979.

[2] HP Zhu, ZY Zhou, RY Yang, and AB Yu. Discrete particle simulation of particulate systems: a review of major applications and findings. *Chemical Engineering Science*, 63(23):5728–5770, 2008.

[3] Shahab Golshan, Rahmat Sotudeh-Gharebagh, Reza Zarghami, Navid Mostoufi, Bruno Blais, and JAM Kuipers. Review and implementation of cfd-dem applied to chemical process systems. *Chemical Engineering Science*, 221:115646, 2020.

[4] Mahmoud A El-Emam, Ling Zhou, Weidong Shi, Chen Han, Ling Bai, and Ramesh Agarwal. Theories and applications of cfd–dem coupling approach for granular flow: A review. *Archives of Computational Methods in Engineering*, 28(7):4979–5020, 2021.

[5] Pierre Jop, Yoël Forterre, and Olivier Pouliquen. A constitutive law for dense granular flows. *Nature*, 441(7094):727–730, 2006.

[6] Ken Kamrin and Georg Koval. Nonlocal constitutive relation for steady granular flow. *Physical Review Letters*, 108(17):178301, 2012.

[7] Aaron S Baumgarten and Ken Kamrin. A general fluid–sediment mixture model and constitutive theory validated in many flow regimes. *Journal of Fluid Mechanics*, 861:721–764, 2019.

[8] Eugen Meyer-Peter and R Müller. Formulas for bed-load transport. In *IAHSR 2nd meeting, Stockholm, appendix 2*. IAHR, 1948.

[9] Miguel Wong. Does the bedload equation of meyer-peter and müller fit its own data. In *Proceedings, 30th Congress, International Association of Hydraulic Research, Thessaloniki, JFK Competition*, volume 73, page 80, 2003.

[10] Qiong Zhang, Stephen Townsend, and Ken Kamrin. Expanded scaling relations for locomotion in sloped or cohesive granular beds. *Physical Review Fluids*, 5(11):114301, 2020.

[11] James Slonaker, D Carrington Motley, Qiong Zhang, Stephen Townsend, Carmine Senatore, Karl Iagnemma, and Ken Kamrin. General scaling relations for locomotion in granular media. *Physical Review E*, 95(5):052901, 2017.

[12] Andrew Schofield and Peter Wroth. *Critical state soil mechanics*, volume 310. McGraw-Hill London, 1968.

[13] David Muir Wood. *Soil behaviour and critical state soil mechanics*. Cambridge university press, 1990.

[14] F Radjai. Physics of dry granular media, 1997.

[15] Trushant S Majmudar and Robert P Behringer. Contact force measurements and stress-induced anisotropy in granular materials. *Nature*, 435(7045):1079, 2005.

[16] GDR MiDi. On dense granular flows. *The European Physical Journal E*, 14(4):341–365, 2004.

[17] Frédéric Da Cruz, Sacha Emam, Michaël Prochnow, Jean-Noël Roux, and François Chevoir. Rheophysics of dense granular materials: Discrete simulation of plane shear flows. *Physical Review E*, 72(2):021309, 2005.

[18] P Jop. P. jop, y. forterre, and o. pouliquen, nature (london) 441, 727 (2006). *Nature (London)*, 441:727, 2006.

[19] Ken Kamrin and David L Henann. Nonlocal modeling of granular flows down inclines. *Soft matter*, 11(1):179–185, 2015.

[20] Binquan Kou, Yixin Cao, Jindong Li, Chengjie Xia, Zhifeng Li, Haipeng Dong, Ang Zhang, Jie Zhang, Walter Kob, and Yujie Wang. Granular materials flow like complex fluids. *Nature*, 551(7680):360, 2017.

[21] Sarah S Sharpe, Robyn Kuckuk, and Daniel I Goldman. Controlled preparation of wet granular media reveals limits to lizard burial ability. *Physical biology*, 12(4):046009, 2015.

[22] Rausan Jewel, Andreea Panaitescu, and Arshad Kudrolli. Micromechanics of intruder motion in wet granular medium. *Physical Review Fluids*, 3(8):084303, 2018.

[23] RT Shield. On coulomb's law of failure in soils. *Journal of the Mechanics and Physics of Solids*, 4(1):10–16, 1955.

[24] M Massoudi and MM Mehrabadi. A continuum model for granular materials: considering dilatancy and the mohr-coulomb criterion. *Acta Mechanica*, 152(1-4):121–138, 2001.

[25] Ronald Midgley Nedderman. *Statics and kinematics of granular materials*. Cambridge University Press, 2005.

[26] Ryan C Hurley and José E Andrade. Continuum modeling of rate-dependent granular flows in sph. *Computational Particle Mechanics*, 4(1):119–130, 2017.

[27] Sachith Dunatunga and Ken Kamrin. Continuum modeling of projectile impact and penetration in dry granular media. *Journal of the Mechanics and Physics of Solids*, 100:45–60, 2017.

[28] David L Henann and Ken Kamrin. A predictive, size-dependent continuum model for dense granular flows. *Proceedings of the National Academy of Sciences*, 110(17):6730–6735, 2013.

[29] Steve Plimpton. Fast parallel algorithms for short-range molecular dynamics. *Journal of computational physics*, 117(1):1–19, 1995.

[30] Georg Koval, Jean-Noël Roux, Alain Corfdir, and François Chevoir. Annular shear of cohesionless granular materials: From the inertial to quasistatic regime. *Physical Review E*, 79(2):021306, 2009.

[31] Ken Kamrin and Georg Koval. Effect of particle surface friction on nonlocal constitutive behavior of flowing granular media. *Computational Particle Mechanics*, 1(2):169–176, 2014.

[32] Qiong Zhang and Ken Kamrin. Microscopic description of the granular fluidity field in nonlocal flow modeling. *Physical review letters*, 118(5):058001, 2017.

[33] Stefan Luding. Contact models for very loose granular materials. In *IUTAM Symposium on Multiscale Problems in Multibody System Contacts*, pages 135–150. Springer, 2007.

[34] Guillaume Grégoire, Hugues Chaté, and Yuhai Tu. Moving and staying together without a leader. *Physica D: Nonlinear Phenomena*, 181(3-4):157–170, 2003.

[35] Leonardo E Silbert, James W Landry, and Gary S Grest. Granular flow down a rough inclined plane: transition between thin and thick piles. *Physics of Fluids*, 15(1):1–10, 2003.

[36] A Janda, Iker Zuriguel, A Garcimartín, Luis A Pugnaloni, and Diego Maza. Jamming and critical outlet size in the discharge of a two-dimensional silo. *EPL (Europhysics Letters)*, 84(4):44002, 2008.

[37] CKK Lun, S Br Savage, DJ Jeffrey, and N Chepurniy. Kinetic theories for granular flow: inelastic particles in couette flow and slightly inelastic particles in a general flowfield. *Journal of fluid mechanics*, 140:223–256, 1984.

[38] James T Jenkins and Stuart B Savage. A theory for the rapid flow of identical, smooth, nearly elastic, spherical particles. *Journal of fluid mechanics*, 130:187–202, 1983.

[39] Igor S Aranson and Lev S Tsimring. Continuum theory of partially fluidized granular flows. *Physical Review E*, 65(6):061303, 2002.

[40] Dmitri Volfson, Lev S Tsimring, and Igor S Aranson. Order parameter description of stationary partially fluidized shear granular flows. *Physical review letters*, 90(25):254301, 2003.

[41] Steven T Nase, Watson L Vargas, Adetola A Abatan, and JJ McCarthy. Discrete characterization tools for cohesive granular material. *Powder Technology*, 116(2-3):214–223, 2001.

[42] F Bertrand, L-A Leclaire, and G Levecque. Dem-based models for the mixing of granular materials. *Chemical Engineering Science*, 60(8-9):2517–2531, 2005.

[43] R Deiva Venkatesh, M Grmela, and J Chaouki. Simulations of vibrated fine powders. *Powder technology*, 100(2-3):211–222, 1998.

[44] Guoping Lian, Colin Thornton, and Michael J Adams. A theoretical study of the liquid bridge forces between two rigid spherical bodies. *Journal of colloid and interface science*, 161(1):138–147, 1993.

[45] M Toivakka, P Salminen, Y Chonde, and DW Bousfield. Consolidation of particulate suspension–model study with plastic pigments. In *Proceedings of 1997 TAPPI Advanced Coating Fundamentals Symposium*, page 89. TAPPI Press Atlanta, GA, USA, 1997.

[46] Qiong Zhang, Eric Deal, J. Taylor Perron, Jeremy G. Venditti, Santiago J. Benavides, Matthew Rushlow, and Ken Kamrin. Fluid-driven transport of round sediment particles: From discrete simulations to continuum modeling. *Journal of Geophysical Research: Earth Surface*, 127(7):e2021JF006504, 2022.

[47] Basil Gomez. Bedload transport. *Earth-Science Reviews*, 31(2):89–132, 1991.

[48] Mehmet Selim Yalin and AM Ferreira Da Silva. Fluvial processes. iahr monograph. *International Association for Hydraulic Research, Delft*, 2001.

[49] Morgane Houssais, Carlos P Ortiz, Douglas J Durian, and Douglas J Jerolmack. Onset of sediment transport is a continuous transition driven by fluid shear and granular creep. *Nature communications*, 6(1):1–8, 2015.

[50] K Ashida and M Michiue. Studies on bed-load transport rate in open channel flows. *IN: SEDIMENT TRANSPORTATION, VOLUME 1*, 1973.

[51] R Fernandez Luque and R Van Beek. Erosion and transport of bed-load sediment. *Journal of hydraulic research*, 14(2):127–144, 1976.

[52] Patricia L Wiberg and J Dungan Smith. Model for calculating bed load transport of sediment. *Journal of hydraulic engineering*, 115(1):101–123, 1989.

[53] Ralph Alger Bagnold. An empirical correlation of bedload transport rates in flumes and natural rivers. In *Proceedings of the Royal Society of London A: Mathematical, Physical and Engineering Sciences*, volume 372, pages 453–473. The Royal Society, 1980.

[54] IA Shields. Anwendung der ahnlichkeitmechanik und der turbulenzforschung auf die gescheibebewegung, mitt. preuss ver. *Anst., Berlin*, 26, 1936.

[55] Eric Lajeunesse, Luce Malverti, and François Charru. Bed load transport in turbulent flow at the grain scale: Experiments and modeling. *Journal of Geophysical Research: Earth Surface*, 115(F4), 2010.

[56] Thomas Pähtz and Orencio Durán. Unification of aeolian and fluvial sediment transport rate from granular physics. *Physical Review Letters*, 124(16):168001, 2020.

[57] Frank Engelund and Jørgen Fredsøe. A sediment transport model for straight alluvial channels. *Hydrology Research*, 7(5):293–306, 1976.

[58] Ian Reid and Jonathan B Laronne. Bed load sediment transport in an ephemeral stream and a comparison with seasonal and perennial counterparts. *Water Resources Research*, 31(3):773–781, 1995.

[59] Raphael Maurin, Julien Chauchat, and Philippe Frey. Revisiting slope influence in turbulent bedload transport: consequences for vertical flow structure and transport rate scaling. *Journal of Fluid Mechanics*, 839:135–156, 2018.

[60] Jacobus J Derksen. Simulations of granular bed erosion due to a mildly turbulent shear flow. *Journal of Hydraulic Research*, 53(5):622–632, 2015.

[61] Mark W Schmeeckle. Numerical simulation of turbulence and sediment transport of medium sand. *Journal of Geophysical Research: Earth Surface*, 119(6):1240–1262, 2014.

[62] Mark W Schmeeckle. The role of velocity, pressure, and bed stress fluctuations in bed load transport over bed forms: numerical simulation downstream of a backward-facing step. *Earth Surface Dynamics*, 3(1):105, 2015.

[63] Justin R Finn, Ming Li, and Sourabh V Apte. Particle based modelling and simulation of natural sand dynamics in the wave bottom boundary layer. *Journal of Fluid Mechanics*, 796:340–385, 2016.

[64] Liheng Guan, JS Salinas, N Zgheib, and S Balachandar. The role of bed-penetrating kelvin–helmholtz vortices on local and instantaneous bedload sediment transport. *Journal of Fluid Mechanics*, 911, 2021.

[65] Raphaël Maurin, Julien Chauchat, Bruno Chareyre, and Philippe Frey. A minimal coupled fluid-discrete element model for bedload transport. *Physics of Fluids*, 27(11):113302, 2015.

[66] Husam A Elghannay and Danesh K Tafti. Sensitivity of numerical parameters on dem predictions of sediment transport. *Particulate Science and Technology*, 36(4):438–446, 2018.

[67] Thomas Pähtz and Orencio Durán. Universal friction law at granular solid-gas transition explains scaling of sediment transport load with excess fluid shear stress. *Physical Review Fluids*, 3(10):104302, 2018.

[68] Thomas Pähtz and Orencio Durán. The cessation threshold of nonsuspended sediment transport across aeolian and fluvial environments. *Journal of Geophysical Research: Earth Surface*, 123(8):1638–1666, 2018.

[69] Subhasish Dey and Sk Zeeshan Ali. Mechanics of sediment transport: Particle scale of entrainment to continuum scale of bedload flux. *Journal of Engineering Mechanics*, 143(11):04017127, 2017.

[70] Chuanhu Zhang, Kenichi Soga, Krishna Kumar, Qicheng Sun, and Feng Jin. Numerical study of a sphere descending along an inclined slope in a liquid. *Granular Matter*, 19(4):1–19, 2017.

[71] Jacobus J Derksen. Simulations of granular bed erosion due to laminar shear flow near the critical shields number. *Physics of Fluids*, 23(11):113303, 2011.

[72] Eric A Deal, Jeremy G Venditti, Santiago J Benavides, Ryan Bradley, Qiong Zhang, Ken Kamrin, and J Taylor Perron. Grain shape effects in bed load sediment transport. 2021.

[73] Santiago J Benavides, Eric Deal, Matthew Rushlow, Jeremy G Venditti, Qiong Zhang, Ken Kamrin, and J Taylor Perron. The impact of intermittency on bed load sediment transport. *Geophysical Research Letters*, page e2021GL096088, 2021.

[74] Andrés Vargas-Luna, Alessandra Crosato, and Wim SJ Uijttewaal. Effects of vegetation on flow and sediment transport: comparative analyses and validation of predicting models. *Earth Surface Processes and Landforms*, 40(2):157–176, 2015.

[75] Chao Liu, Yuqi Shan, and Heidi Nepf. Impact of stem size on turbulence and sediment resuspension under unidirectional flow. *Water Resources Research*, 57(3):e2020WR028620, 2021.

[76] B Mutlu Sumer, Lloyd HC Chua, N-S Cheng, and Jørgen Fredsøe. Influence of turbulence on bed load sediment transport. *Journal of Hydraulic Engineering*, 129(8):585–596, 2003.

[77] Satya P Ojha, BS Mazumder, S Carstensen, and J Fredsoe. Externally generated turbulence by a vertically oscillating grid plate and its impact on sediment transport rate. *Coastal Engineering Journal*, 61(4):444–459, 2019.

[78] NS Cheng, MX Wei, YM Chiew, YS Lu, and A Emadzadeh. Combined effects of mean flow and turbulence on sediment pickup rate. *Water Resources Research*, 56(2):e2019WR026181, 2020.

[79] J.G. Venditti. 9.10 bedforms in sand-bedded rivers. In John F. Shroder, editor, *Treatise on Geomorphology*, pages 137–162. Academic Press, San Diego, 2013.

[80] Jeremy G Venditti, Peter A Nelson, Ryan W Bradley, Dan Haught, and Alessandro B Gitto. Bedforms, structures, patches, and sediment supply in gravel-bed rivers. *Gravel-Bed Rivers: Processes and Disasters, edited by: Tsutsumi, D. and Laronne, JB, John Wiley & Sons, Chichester, England*, pages 439–466, 2017.

[81] EM Yager, JW Kirchner, and WE Dietrich. Calculating bed load transport in steep boulder bed channels. *Water Resources Research*, 43(7), 2007.

[82] Mark W Schmeeckle and Jonathan M Nelson. Direct numerical simulation of bedload transport using a local, dynamic boundary condition. *Sedimentology*, 50(2):279–301, 2003.

[83] Kimberly M Hill and Danielle Tan. Granular flows applied to gravel-bed rivers: particle-scale studies of the mobilization of a gravel bed by the addition of fines. *Gravel-Bed Rivers: Processes and Disasters*, pages 73–95, 2017.

[84] Miguel Wong and Gary Parker. Reanalysis and correction of bed-load relation of meyer-peter and müller using their own database. *Journal of Hydraulic Engineering*, 132(11):1159–1168, 2006.

[85] Hudong Chen, Shiyi Chen, and William H Matthaeus. Recovery of the navier-stokes equations using a lattice-gas boltzmann method. *Physical review A*, 45(8):R5339, 1992.

[86] David F Boutt, Benjamin K Cook, Brian JOL McPherson, and JR Williams. Direct simulation of fluid-solid mechanics in porous media using the discrete element and lattice-boltzmann methods. *Journal of Geophysical Research: Solid Earth*, 112(B10), 2007.

[87] Lhassan Amarsid, J-Y Delenne, Patrick Mutabaruka, Yann Monerie, Frédéric Perales, and Farhang Radjai. Viscoinertial regime of immersed granular flows. *Physical Review E*, 96(1):012901, 2017.

[88] William C Swope, Hans C Andersen, Peter H Berens, and Kent R Wilson. A computer simulation method for the calculation of equilibrium constants for the formation of physical clusters of molecules: Application to small water clusters. *The Journal of chemical physics*, 76(1):637–649, 1982.

[89] Christoph Kloss, Christoph Goniva, Alice Hager, Stefan Amberger, and Stefan Pirker. Models, algorithms and validation for opensource dem and cfd–dem.

Progress in Computational Fluid Dynamics, an International Journal, 12(2-3):140–152, 2012.

[90] Shiyi Chen and Gary D Doolen. Lattice boltzmann method for fluid flows. *Annual review of fluid mechanics*, 30(1):329–364, 1998.

[91] Cyrus K Aidun and Jonathan R Clausen. Lattice-boltzmann method for complex flows. *Annual review of fluid mechanics*, 42:439–472, 2010.

[92] Huidan Yu, Sharath S Girimaji, and Li-Shi Luo. Dns and les of decaying isotropic turbulence with and without frame rotation using lattice boltzmann method. *Journal of Computational Physics*, 209(2):599–616, 2005.

[93] Joseph Smagorinsky. General circulation experiments with the primitive equations: I. the basic experiment. *Monthly weather review*, 91(3):99–164, 1963.

[94] A Yoshizawa. Subgrid-scale modeling suggested by a two-scale dia. In *Computational Wind Engineering 1*, pages 69–76. Elsevier, 1993.

[95] Shuling Hou, J Sterling, Shiyi Chen, and GD Doolen. A lattice boltzmann subgrid model for high reynolds number flows. *arXiv preprint comp-gas/9401004*, 1994.

[96] Zhaoli Guo, Chuguang Zheng, and Baochang Shi. Discrete lattice effects on the forcing term in the lattice boltzmann method. *Physical review E*, 65(4):046308, 2002.

[97] M'hamed Bouzidi, Mouaouia Firdaouss, and Pierre Lallemand. Momentum transfer of a boltzmann-lattice fluid with boundaries. *Physics of fluids*, 13(11):3452–3459, 2001.

[98] Anthony JC Ladd. Numerical simulations of particulate suspensions via a discretized boltzmann equation. part 1. theoretical foundation. *Journal of fluid mechanics*, 271:285–309, 1994.

[99] Renwei Mei, Dazhi Yu, Wei Shyy, and Li-Shi Luo. Force evaluation in the lattice boltzmann method involving curved geometry. *Physical Review E*, 65(4):041203, 2002.

[100] Sauro Succi. *The lattice Boltzmann equation: for fluid dynamics and beyond*. Oxford university press, 2001.

[101] Zhi-Gang Feng and Efstathios E Michaelides. Robust treatment of no-slip boundary condition and velocity updating for the lattice-boltzmann simulation of particulate flows. *Computers & Fluids*, 38(2):370–381, 2009.

[102] Jacobus J Derksen. Simulations of hindered settling of flocculating spherical particles. *International journal of multiphase flow*, 58:127–138, 2014.

[103] Patrick Mutabaruka, Jean-Yves Delenne, Kenichi Soga, and Farhang Radjai. Initiation of immersed granular avalanches. *Physical Review E*, 89(5):052203, 2014.

[104] Patrick Mutabaruka and Ken Kamrin. Simulation technique for slurries interacting with moving parts and deformable solids with applications. *Computational Particle Mechanics*, 5(2):239–267, 2018.

[105] P Gondret, M Lance, and L Petit. Bouncing motion of spherical particles in fluids. *Physics of fluids*, 14(2):643–652, 2002.

[106] A Ten Cate, CH Nieuwstad, Jacobus J Derksen, and HEA Van den Akker. Particle imaging velocimetry experiments and lattice-boltzmann simulations on a single sphere settling under gravity. *Physics of Fluids*, 14(11):4012–4025, 2002.

[107] Xiaobai Li, Melany L Hunt, and Tim Colonius. A contact model for normal immersed collisions between a particle and a wall. *Journal of fluid mechanics*, 691:123–145, 2012.

[108] Marc-Florian Uth, Alf Crüger, and Heinz Herwig. A new partial slip boundary condition for the lattice-boltzmann method. In *International Conference on Nanochannels, Microchannels, and Minichannels*, volume 55591, page V001T12A001. American Society of Mechanical Engineers, 2013.

[109] Kai Wang, Zhenhua Chai, Guoxiang Hou, Wei Chen, and Sheng Xu. Slip boundary condition for lattice boltzmann modeling of liquid flows. *Computers & Fluids*, 161:60–73, 2018.

[110] Christophe Ancey and Ivan Pascal. Estimating mean bedload transport rates and their uncertainty. *Journal of Geophysical Research: Earth Surface*, 125(7):e2020JF005534, 2020.

[111] Junke Guo. Sidewall and non-uniformity corrections for flume experiments. *Journal of Hydraulic Research*, 53(2):218–229, 2015.

[112] Joris Heyman, Patricio Bohorquez, and Christophe Ancey. Entrainment, motion, and deposition of coarse particles transported by water over a sloping mobile bed. *Journal of Geophysical Research: Earth Surface*, 121(10):1931–1952, 2016.

[113] G Rousseau and C Ancey. An experimental investigation of turbulent free-surface flows over a steep permeable bed. *Journal of Fluid Mechanics*, 941, 2022.

[114] Panayiotis Diplas, Clint L Dancey, Ahmet O Celik, Manousos Valyrakis, Krista Greer, and Tanju Akar. The role of impulse on the initiation of particle movement under turbulent flow conditions. *Science*, 322(5902):717–720, 2008.

[115] Bernhard Vowinckel, Ramandeep Jain, Tobias Kempe, and Jochen Fröhlich. Entrainment of single particles in a turbulent open-channel flow: A numerical study. *Journal of Hydraulic Research*, 54(2):158–171, 2016.

[116] Seongmin Kim and Ken Kamrin. Power-law scaling in granular rheology across flow geometries. *Physical Review Letters*, 125(8):088002, 2020.

[117] Julien Chauchat and Sylvain Guillou. On turbulence closures for two-phase sediment-laden flow models. *Journal of Geophysical Research: Oceans*, 113(C11), 2008.

[118] Masato Sekine and Hideo Kikkawa. Mechanics of saltating grains. ii. *Journal of Hydraulic Engineering*, 118(4):536–558, 1992.

[119] Yarko Niño, Marcelo García, and Luis Ayala. Gravel saltation: 1. experiments. *Water resources research*, 30(6):1907–1914, 1994.

[120] Antonio Signorini. Sopra alcune questioni di statica dei sistemi continui. *Annali della Scuola Normale Superiore di Pisa-Classe di Scienze*, 2(2):231–251, 1933.

[121] Samila Bandara and Kenichi Soga. Coupling of soil deformation and pore fluid flow using material point method. *Computers and geotechnics*, 63:199–214, 2015.

[122] Raphael Maurin, Julien Chauchat, and Philippe Frey. Dense granular flow rheology in turbulent bedload transport. *Journal of Fluid Mechanics*, 804:490–512, 2016.

[123] Julien Chauchat. A comprehensive two-phase flow model for unidirectional sheet-flows. *Journal of Hydraulic Research*, 56(1):15–28, 2018.

[124] François Boyer, Élisabeth Guazzelli, and Olivier Pouliquen. Unifying suspension and granular rheology. *Physical Review Letters*, 107(18):188301, 2011.

[125] Martin Trulsson, Bruno Andreotti, and Philippe Claudin. Transition from the viscous to inertial regime in dense suspensions. *Physical review letters*, 109(11):118305, 2012.

[126] Eugene Cosserat and François Cosserat. *Théorie des corps déformables*. A. Hermann et fils, 1909.

[127] Ken Kamrin. Non-locality in granular flow: Phenomenology and modeling approaches. *Frontiers in Physics*, 7:116, 2019.

[128] Liya Li and Masaki Sawamoto. Multi-phase model on sediment transport in sheet-flow regime under oscillatory flow. *Coastal Engineering in Japan*, 38(2):157–178, 1995.

[129] Thibaud Revil-Baudard, Julien Chauchat, David Hurther, and Pierre-Alain Barraud. Investigation of sheet-flow processes based on novel acoustic high-resolution velocity and concentration measurements. *Journal of Fluid Mechanics*, 767:1–30, 2015.

[130] Diego Berzi and Luigi Fraccarollo. Turbulence locality and granularlike fluid shear viscosity in collisional suspensions. *Physical review letters*, 115(19):194501, 2015.

[131] Wei-Jay Ni and Hervé Capart. Stresses and drag in turbulent bed load from refractive index-matched experiments. *Geophysical Research Letters*, 45(14):7000–7009, 2018.

[132] O Simonin. Numerical study on phase dispersion mechanisms in turbulent bubbly flows. In *Int. Conf. on Mechanics of Two-Phase Flows*, pages 163–165, 1989.

[133] Hunter Rouse. Modern conceptions of the mechnics of turbulence. *Transactions American Soc. of Civil Engineers*, 102:463–505, 1937.

[134] L Schiller. Über die grundlegenden berechnungen bei der schwerkraftaufbereitung. *Z. Vereines Deutscher Inge.*, 77:318–321, 1933.

[135] Julien Chauchat, Zhen Cheng, Tim Nagel, Cyrille Bonamy, and Tian-Jian Hsu. Sedfoam-2.0: a 3-d two-phase flow numerical model for sediment transport. *Geoscientific Model Development*, 10(12):4367–4392, 2017.

[136] R Beetstra, Martin Anton van der Hoef, and JAM Kuipers. Drag force of intermediate reynolds number flow past mono-and bidisperse arrays of spheres. *AIChE journal*, 53(2):489–501, 2007.

[137] Jonathan J Wylie, Donald L Koch, and Anthony JC Ladd. Rheology of suspensions with high particle inertia and moderate fluid inertia. *Journal of Fluid Mechanics*, 480:95, 2003.

[138] SHL Kriebitzsch, MA Van der Hoef, and JAM Kuipers. Fully resolved simulation of a gas-fluidized bed: a critical test of dem models. *Chemical Engineering Science*, 91:1–4, 2013.

[139] William Holloway, Jin Sun, and Sankaran Sundaresan. Effect of microstructural anisotropy on the fluid–particle drag force and the stability of the uniformly fluidized state. *Journal of Fluid Mechanics*, 713:27–49, 2012.

[140] Teng Ma, Yaxiong Yu, Xiao Chen, and Qiang Zhou. Effect of anisotropic microstructures on fluid–particle drag in low-reynolds-number monodisperse gas–solid suspensions. *AIChE Journal*, 66(4):e16910, 2020.

[141] JF Richardson and WN Zaki. Sedimentation and fluidisation: Part i. *Trans. Instn Chem. Engrs*, 32:35–53, 1954.

[142] R Di Felice. On the voidage function in two-phase multiparticle systems. *Int. J. Multiphase Flow*, 20:153–159, 1994.

[143] Mickael Pailha and Olivier Pouliquen. A two-phase flow description of the initiation of underwater granular avalanches. *Journal of Fluid Mechanics*, 633:115, 2009.

[144] Daniel M Mueth. Measurements of particle dynamics in slow, dense granular couette flow. *Physical Review E*, 67(1):011304, 2003.

[145] C Bonnoit, T Darnige, E Clement, and A Lindner. Inclined plane rheometry of a dense granular suspension. *Journal of Rheology*, 54(1):65–79, 2010.

[146] Behrooz Ferdowsi, Carlos P Ortiz, Morgane Houssais, and Douglas J Jerolmack. River-bed armouring as a granular segregation phenomenon. *Nature communications*, 8(1):1–10, 2017.

[147] Benjamin Allen and Arshad Kudrolli. Depth resolved granular transport driven by shearing fluid flow. *Physical Review Fluids*, 2(2):024304, 2017.

[148] Saloome Siavoshi, Ashish V Orpe, and Arshad Kudrolli. Friction of a slider on a granular layer: Nonmonotonic thickness dependence and effect of boundary conditions. *Physical Review E*, 73(1):010301, 2006.

[149] Ingo Kock and Katrin Huhn. Influence of particle shape on the frictional strength of sediments—a numerical case study. *Sedimentary Geology*, 196(1-4):217–233, 2007.

[150] Thomas Pähtz, Yonghui Liu, Yuezhang Xia, Peng Hu, Zhiguo He, and Katharina Tholen. Unified model of sediment transport threshold and rate across weak and intense subaqueous bedload, windblown sand, and windblown snow. *Journal of Geophysical Research: Earth Surface*, 126(4):e2020JF005859, 2021.

[151] Ramandeep Jain, Silvio Tschisgale, and Jochen Fröhlich. Impact of shape: Dns of sediment transport with non-spherical particles. *Journal of Fluid Mechanics*, 916, 2021.

[152] Benoît Camenen. Simple and general formula for the settling velocity of particles. *Journal of Hydraulic Engineering*, 133(2):229–233, 2007.

[153] Lucy G MacKenzie and Brett C Eaton. Large grains matter: contrasting bed stability and morphodynamics during two nearly identical experiments. *Earth Surface Processes and Landforms*, 42(8):1287–1295, 2017.

[154] Lucy G MacKenzie, Brett C Eaton, and Michael Church. Breaking from the average: Why large grains matter in gravel-bed streams. *Earth Surface Processes and Landforms*, 43(15):3190–3196, 2018.

[155] OR Walton. Effects of interparticle friction and particle shape on dynamic angles of repose via particle-dynamics simulation. In *Proc. Conf. Mechanics and Statistical Physics of Particulate Materials, June*, pages 8–10, 1994.

[156] Joanna Wiacek, Marek Molenda, Józef Horabik, and Jin Y Ooi. Influence of grain shape and intergranular friction on material behavior in uniaxial compression: Experimental and dem modeling. *Powder Technology*, 217:435–442, 2012.

[157] Gary Parker. Self-formed straight rivers with equilibrium banks and mobile bed. part 2. the gravel river. *Journal of Fluid mechanics*, 89(1):127–146, 1978.

[158] Benjamin Allen and Arshad Kudrolli. Granular bed consolidation, creep, and armoring under subcritical fluid flow. *Physical Review Fluids*, 3(7):074305, 2018.

[159] Thomas Pähtz, Abram H Clark, Manousos Valyrakis, and Orencio Durán. The physics of sediment transport initiation, cessation, and entrainment across aeolian and fluvial environments. *Reviews of Geophysics*, 58(1):e2019RG000679, 2020.

[160] Teruhisa S Komatsu, Shio Inagaki, Naoko Nakagawa, and Satoru Nasuno. Creep motion in a granular pile exhibiting steady surface flow. *Physical review letters*, 86(9):1757, 2001.

[161] Daren Liu and David L Henann. Non-local continuum modelling of steady, dense granular heap flows. *Journal of Fluid Mechanics*, 831:212–227, 2017.

[162] Gary Parker, Peter C Klingeman, and David G McLean. Bedload and size distribution in paved gravel-bed streams. *Journal of the Hydraulics Division*, 108(4):544–571, 1982.

[163] GT Proffitt and AJ Sutherland. Transport of non-uniform sediments. *Journal of hydraulic research*, 21(1):33–43, 1983.

[164] Peter R Wilcock and Joanna C Crowe. Surface-based transport model for mixed-size sediment. *Journal of hydraulic engineering*, 129(2):120–128, 2003.

[165] Albert Shields. Application of similarity principles and turbulence research to bed-load movement. 1936.

[166] RI Ferguson and SJ Wathen. Tracer-pebble movement along a concave river profile: Virtual velocity in relation to grain size and shear stress. *Water Resources Research*, 34(8):2031–2038, 1998.

[167] J Warburton and T Demir. Influence of bed material shape on sediment transport in gravel-bed rivers: a field experiment. In *Tracers in geomorphology*, pages 401–410, 2000.

[168] Tuncer Demir. *The influence of particle shape on bedload transport in coarse-bed river channels*. PhD thesis, Durham University, 2000.

[169] Ashley Dudill, Jeremy G Venditti, Michael Church, and Philippe Frey. Comparing the behaviour of spherical beads and natural grains in bedload mixtures. *Earth Surface Processes and Landforms*, 45(4):831–840, 2020.

[170] Paul W Cleary. The effect of particle shape on simple shear flows. *Powder Technology*, 179(3):144–163, 2008.

[171] Paul D Komar and Zhenlin Li. Pivoting analyses of the selective entrainment of sediments by shape and size with application to gravel threshold. *Sedimentology*, 33(3):425–436, 1986.

[172] Elowyn M Yager, Mark W Schmeeckle, and Alexandre Badoux. Resistance is not futile: Grain resistance controls on observed critical shields stress variations. *Journal of Geophysical Research: Earth Surface*, 123(12):3308–3322, 2018.

[173] Mathieu Cassel, Jerome Lave, Alain Recking, Jean-René Malavoi, and Hervé Piégay. Bedload transport in rivers, size matters but so does shape. *Scientific Reports*, 11(1):1–11, 2021.

[174] William Christian Krumbein. Measurement and geological significance of shape and roundness of sedimentary particles. *Journal of Sedimentary Research*, 11(2):64–72, 1941.

[175] Simon J Blott and Kenneth Pye. Particle shape: a review and new methods of characterization and classification. *Sedimentology*, 55(1):31–63, 2008.

[176] AT Corey. Influence of shape on fall velocity of sand grains [unpublished ms thesis]: Colorado a&m college. *Fort Collins, Colorado*, 1949.

[177] William E Dietrich. Settling velocity of natural particles. *Water resources research*, 18(6):1615–1626, 1982.

[178] Rafael Bravo, Pablo Ortiz, and José Luis Pérez-Aparicio. Analytical and discrete solutions for the incipient motion of ellipsoidal sediment particles. *Journal of Hydraulic Research*, 56(1):29–43, 2018.

[179] Boxi Zhang, Dong Xu, Bingchang Zhang, Chunning Ji, Antonio Munjiza, and John Williams. Numerical investigation on the incipient motion of non-spherical sediment particles in bedload regime of open channel flows. *Computational Particle Mechanics*, 7(5):987–1003, 2020.

[180] D Höhner, S Wirtz, H Kruggel-Emden, and V Scherer. Comparison of the multisphere and polyhedral approach to simulate non-spherical particles within the discrete element method: Influence on temporal force evolution for multiple contacts. *Powder Technology*, 208(3):643–656, 2011.

[181] Rui Sun, Heng Xiao, and Honglei Sun. Realistic representation of grain shapes in cfd–dem simulations of sediment transport with a bonded-sphere approach. *Advances in water resources*, 107:421–438, 2017.

[182] JF Favier, MH Abbaspour-Fard, M Kremmer, and AO Raji. Shape representation of axi-symmetrical, non-spherical particles in discrete element simulation using multi-element model particles. *Engineering computations*, 1999.

[183] JF Favier, MH Abbaspour-Fard, and M Kremmer. Modeling nonspherical particles using multisphere discrete elements. *Journal of Engineering Mechanics*, 127(10):971–977, 2001.

[184] Maryam Alihosseini and Paul Uwe Thamsen. Experimental and numerical investigation of sediment transport in sewers. In *Fluids Engineering Division Summer Meeting*, volume 51579, page V003T17A005. American Society of Mechanical Engineers, 2018.

[185] Bing Shao, Yifei Yan, Xiangzhen Yan, and Zhiqian Xu. A study on non-spherical cuttings transport in cbm well drilling by coupled cfd-dem. *Engineering Applications of Computational Fluid Mechanics*, 13(1):579–590, 2019.

[186] S Fukuoka, T Fukuda, and T Uchida. Effects of sizes and shapes of gravel particles on sediment transports and bed variations in a numerical movable-bed channel. *Advances in water resources*, 72:84–96, 2014.

[187] Tomoo Fukuda and Shoji Fukuoka. Interface-resolved large eddy simulations of hyperconcentrated flows using spheres and gravel particles. *Advances in Water Resources*, 129:297–310, 2019.

[188] Stefan Amberger, Michael Friedl, Christoph Goniva, Stefan Pirker, and Christoph Kloss. Approximation of objects by spheres for multisphere simulations in dem. *ECCOMAS-2012*, 2012.

[189] Cheng-Qing Li, Wen-Jie Xu, and Qing-Shan Meng. Multi-sphere approximation of real particles for dem simulation based on a modified greedy heuristic algorithm. *Powder Technology*, 286:478–487, 2015.

[190] Wenqi Zhong, Aibing Yu, Xuejiao Liu, Zhenbo Tong, and Hao Zhang. Dem/cfd-dem modelling of non-spherical particulate systems: theoretical developments and applications. *Powder technology*, 302:108–152, 2016.

[191] Matthew RSB Rushlow et al. *Using machine learning, particle tracking, and grain shape modeling to characterize bedload sediment transport*. PhD thesis, Massachusetts Institute of Technology, 2020.

[192] Amir Banari, Yackar Mauzole, Tetsu Hara, Stephan T Grilli, and Christian F Janßen. The simulation of turbulent particle-laden channel flow by the lattice boltzmann method. *International Journal for Numerical Methods in Fluids*, 79(10):491–513, 2015.

[193] Lian-Ping Wang, Cheng Peng, Zhaoli Guo, and Zhaosheng Yu. Lattice boltzmann simulation of particle-laden turbulent channel flow. *Computers & Fluids*, 124:226–236, 2016.

[194] Amir Eshghinejadfard, Abouelmagd Abdelsamie, Seyed Ali Hosseini, and Dominique Thevenin. Immersed boundary lattice boltzmann simulation of turbulent channel flows in the presence of spherical particles. *International Journal of Multiphase Flow*, 96:161–172, 2017.